

UNIVERSITY OF CALGARY

The Controls of Porosity on Mineral Alteration Processes in the Shallow Oceanic  
Lithosphere at Slow-Spreading Ridges

by

Simone Pujatti

A THESIS

SUBMITTED TO THE FACULTY OF GRADUATE STUDIES

IN PARTIAL FULFILLMENT OF THE REQUIREMENTS FOR THE

DEGREE OF DOCTOR OF PHILOSOPHY

GRADUATE PROGRAM IN GEOLOGY AND GEOPHYSICS

CALGARY, ALBERTA

MARCH, 2023

©Simone Pujatti 2023

## Abstract

Porosity exerts strong controls on mineral replacement and alteration processes mediated by the action of fluids. These processes are ubiquitous in the Earth's crust, but even more so within the oceanic lithosphere, an environment saturated by infiltrating fluids that can range in composition from hot hydrothermal fluids to low-temperature seawater. This thesis presents examples of fluid-rock interactions that affect mafic and ultramafic lithologies recovered via drilling from the subseafloor of the slow-spreading Mid-Atlantic Ridge. These reactions are enabled by the presence of pores that provide flow pathways for fluids to reach the reaction front of altering minerals. Chapter 2 explores the genesis of petrographic textures observed in samples recovered from the Trans-Atlantic Geotraverse, a hydrothermal sulfide mound that shows black smoker activity. The textures form due to the replacement of anhydrite by pyrite under the action of hot hydrothermal fluids generated via heating of seawater entrained within the oceanic crust, and involved growth of quartz into open space. Intensive investigation of the observed textures detailed in this Chapter provides a mechanistic explanation for the attainment of the sulfur isotopic signatures found in sulfide precipitate within the hydrothermal mound. In Chapter 3, tomographic analysis of serpentinized peridotite at nanometer and micrometer scales reveals the presence of dissolution pores located at the grain boundaries of olivine, which show significant connectivity, suggesting that soluble Mg and Si sourced from the dissolution of olivine are exported to seawater, affecting its chemical budget, alkalinity, and consequently the coupled carbonate-silicate cycle. Chapter 4 tests the hypothesis that the porosity and  $\text{Fe}^{3+}$  contents of serpentinized peridotite increase with increasing serpentinization degree, suggested by correlations between density and magnetic susceptibility of serpentinites established in earlier work. The hypothesis was tested by applying statistical analysis to geochemical and porosity data collected on serpentinite samples recovered

from 10 different drilling sites, revealing complex alteration patterns that involve seafloor weathering processes and thus extend beyond the transformation imparted by serpentinization reactions. Together, the scientific investigations conducted in this thesis demonstrate the importance and complexities of porosity generation and evolution during alteration of the shallow oceanic lithosphere.

## Preface

**Chapter 2.** Published as Pujatti, S., Klyukin, Y., Steele-MacInnis, M., and Tutolo, B.M., (2021). “Anhydrite replacement reaction in nodular pyrite breccia and its geochemical controls on the  $\delta^{34}\text{S}$  signature of pyrite in the TAG hydrothermal mound, 26° N Mid Atlantic Ridge”. *Lithos*, 400–401, 106357, <https://doi.org/10.1016/j.lithos.2021.106357>.

**Chapter 3.** Published as Pujatti, S., Plümper, O., and Tutolo, B. M. (2023). “Weathering-driven porosity generation in altered oceanic peridotites”. *Earth and Planetary Science Letters*, 604, 118006, <https://doi.org/10.1016/j.epsl.2023.118006>.

**Chapter 4.** Submitted to *Lithos* as Pujatti, S., and Tutolo, B.M. (2023). “Fe oxidation and porosity generation in serpentized abyssal peridotite”.

Copyright permissions can be found in Appendix D.

## Acknowledgments

I consider this thesis a great personal achievement, but it would not have been possible without the constant support of many great people and institutions, which I acknowledge in this section in no specific order.

I am proud of being a member of the Reactive Transport Group (RTG), an exceptional team made not just of outstanding students and researchers, but also caring and friendly people that have been a support anchor that allowed me to sail safely through the COVID pandemic and all the obstacles I faced before and after that. Several times during my PhD studies I found myself at an impasse due to the challenges involved with understanding geologic systems, which are intrinsically complex and multifaceted. Benjamin Tutolo always went above and beyond his duties as my advisor, throwing me a safety rope when I would get stuck in scientific quicksand. I am extremely grateful for his endless patience and for pushing me past any obstacle that I faced during the past years at UofC. I cannot overstate how kind, thoughtful and understanding Ben has been, not to mention that he is likely the smartest and most passionately driven scientist I have ever met.

I want to thank Qin Zhang, my PhD partner in crime since the begging of my experience at the University of Calgary, for being down-to-earth and the best laboratory manager I could wish for. Chapter 2 in this thesis would have not been possible without the help from Yury Klyukin, and I particularly cherish the frequent conversations we have had about science and society – Yury is one of the most knowledgeable people I know, and it was always a pleasure to have coffee breaks with him. I thank Juan Carlos de Obeso, who taught me so much about serpentinization and weathering, and would always spend efforts to help the other members of RTG. I am very proud of Juan for obtaining a professorship at the University of Utah, which I think he fully deserves. I thank Adedapo Awolayo for dedicating time to helping me solving my coding problems even past

the end of his research experience with RTG, such levels of selflessness are rare. Sofia Escario was the first post-doc part of RTG and I thank her for patiently keeping up with my hectic schedule during the beginning of my PhD. Zhengqiang Che has been a great member of our research group and was always cheerful and positive, even when facing the most hectic and troublesome times at UofC. I am also grateful to Christiaan Laureijs and Alec Hutchings, who have contributed significantly to my PhD experience. A big thank you to all the rest of the RTG members, including Serhat Sevgen, Cameron Wood, Liam Walters and Lauren Madronich.

During my time at UofC I acted as teaching assistant for various graduate and undergraduate level courses, so I would like to express the utmost gratitude to all the students that I (hopefully) helped during classes and Jennifer Cuthbertson for being a wonderful and kind instructor. I want to express a special mention to some students I helped supervising during their research projects: thank you Hannah Robotka, Aaron Claeys, and Bradley Earl for keeping up with me and being such bright and promising minds.

Several faculty members and researchers at UofC have accompanied me during this journey, so I would like to extend my thanks to Rajeev Sasidharan Nair, Rachel Lauer and Dave Pattison. Amin Ghanizadeh, Adnan Younis and the members of the Tight Oil Consortium have been tremendously helpful with data acquisition, and so have Alan Hildebrand and Lincoln Hanton. Fabio Ciceri deserves a special mention not only because his aid has been vital to the completion of Chapter 4 part of this thesis, but also because we have shared the best and worst moments of graduate life and he has provided constant moral support during our frequent coffee breaks.

I want to thank my former supervisor Oliver Plümper not just for the practical help that resulted in Chapter 3 found in this thesis, but also for believing in me and guiding me towards this PhD opportunity, which is my best achievement so far. I am very grateful also to Matthew Steele-

MacInnis, who contributed to my first publication and is a funny, charismatic, insightful person and outstanding researcher. Michael Nightingale has helped tremendously my lab work and deserves his title as “Santa Claus of the fifth floor” as he never refused helping our group with our laboratory activities, even at the cost of his own time. Jason Droboth has been my closest office mate during the last few years, and I thank him for putting up with my moodiness during difficult times.

My family has been extremely supportive in the past years and I struggle to find the words to express enough gratitude to them. I want to thank my parents Maurizio and Viviana and my brothers Mattia and Luca for believing in me and helping me morally and materially to make my transition to Canada happen. I look forwards to meeting them all once again after the long years of separation during my time in Calgary. The latter wish extends to my sister-in-law Elisa and my niece Ada, whom I cannot wait to finally meet in person.

During the past years in Canada I have not only learnt exciting science, but also met new friends who have massively enriched my experience. I want to thank Manuele Lazzarotto, Marco Venieri, Tom Wilson, Sara Lee, Ryan Mesenchuk, Tanya Peck, Falayha Khawaja, Jacob Forshaw and Jasmine Chase. A big thank you goes also to my lifetime friends Dario Pontrandolfo, Marco Magris, Alessandro Di Bari, Davide Ermacora, Mattia Corbetta and Lorenc and Francesco Shuka who all know me better than myself and have been extremely supportive, I cannot thank them enough.

Last, but not least, I want to thank Harriet Boston. She has been my anchor and the best partner I could wish for, always being caring and understanding of the challenges I was facing. She helped me to overcome every obstacle during my PhD, offering comfort and stability and believing in me

beyond any expectation and in the face of any adversity. A mention goes also to my dog George, who would joyfully greet me every time I returned home after working at the university.

**Funding support:** this thesis was possible thanks to funding provided by the Natural Sciences and Engineering Research Council of Canada (NSERC) to B.M. Tutolo under Discovery Grant RGPIN-2018-03800. Part of the research presented in Chapter 3 was performed at the Electron Microscopy Centre at Utrecht University and received funding from the European Research Council Starting grant (nanoEARTH; 852069) provided to O. Plümper. The research presented in Chapter 3 was possible also thanks to the fellowship granted to S. Pujatti by Interridge in 2018. Part of the research presented in Chapter 3 was performed at the high-energy Biomedical Imaging beamline (BMIT-ID) of the Canadian Light Source, a national research facility of the University of Saskatchewan, which is supported by the Canada Foundation for Innovation (CFI), NSERC, the National Research Council (NRC), the Canadian Institutes of Health Research (CIHR), the Government of Saskatchewan, and the University of Saskatchewan. All research presented in this thesis was conducted on samples and data provided by the International Ocean Discovery Program (IODP).

## Table of contents

Abstract .....	ii
Preface .....	iv
Acknowledgments .....	v
Table of contents .....	ix
List of Tables .....	xii
List of Figures .....	xiii
1 Chapter 1 Introduction .....	1
2 Chapter 2 Anhydrite replacement reaction in nodular pyrite breccia and its geochemical controls on the $\delta^{34}\text{S}$ signature of pyrite in the TAG hydrothermal mound, 26° N Mid Atlantic Ridge. ....	8
2.1 Introduction .....	9
2.1.1 Background .....	9
2.1.2 Geology of the active TAG mound .....	11
2.1.3 $\delta^{34}\text{S}$ signatures at TAG .....	14
2.1.4 Sample selection .....	17
2.2 Methods .....	19
2.2.1 Petrographic analysis .....	19
2.2.2 Microthermometry .....	20
2.2.3 Thermodynamic modelling .....	21
2.3 Results .....	23
2.3.1 Petrographic textures .....	23
2.3.1.1 Nodular pyrite .....	23
2.3.1.2 Mineral replacement reaction .....	25
2.3.1.3 Paragenetic sequence .....	26
2.3.2 Fluid Inclusions .....	28
2.3.3 Modelling saturation states .....	30
2.4 Discussion .....	32
2.4.1 Anhydrite dissolution .....	32
2.4.2 Anhydrite replacement by pyrite .....	34
2.4.3 Nodular texture and related growth processes .....	35
2.4.4 $\delta^{34}\text{S}$ stratigraphy at TAG .....	38
2.5 Conclusion .....	40
3 Chapter 3 Weathering-driven porosity generation in altered oceanic peridotites .....	43

3.1	Introduction .....	44
3.2	Methods .....	47
3.2.1	Geological samples .....	47
3.2.1.1	Leg 209 data sets FIB-1-209 and FIB-2-209 .....	48
3.2.1.2	Leg 209 sample Micro209 .....	49
3.2.1.3	Expedition 357 sample Micro357 .....	50
3.2.1.4	Expedition 304/305 sample Micro304 .....	51
3.2.2	Site variability .....	52
3.2.3	Focused ion beam-scanning electron microscopy .....	52
3.2.4	Synchrotron-based microtomography .....	53
3.2.5	Processing, segmentation and quantification of tomographic data .....	53
3.3	Results .....	55
3.3.1	FIB-1-209 .....	57
3.3.2	FIB-2-209 .....	61
3.3.3	Micro209 .....	63
3.3.4	Micro357 .....	63
3.3.5	Micro304 .....	64
3.4	Discussion .....	66
3.4.1	Anisotropic distribution of pores .....	66
3.4.2	Serpentinization-generated nanopores .....	67
3.4.3	Porosity generation during seafloor weathering .....	68
3.4.4	Elemental fluxes and implications .....	70
3.5	Conclusions .....	72
4	Chapter 4 Fe oxidation and porosity generation in serpentinized abyssal peridotite .....	75
4.1	Introduction .....	76
4.2	Methods .....	78
4.2.1	Geological samples .....	78
4.2.1.1	ODP 109 .....	79
4.2.1.2	ODP 173 .....	79
4.2.1.3	ODP 209 .....	80
4.2.1.4	IODP 304/305 .....	81
4.2.1.5	IODP 357 .....	82
4.2.2	Chemical dataset .....	83
4.2.3	Porosity dataset .....	83

4.2.4	Data processing and analyses .....	85
4.3	Results .....	86
4.3.1	Protolith classification.....	86
4.3.2	Correlation matrix .....	90
4.3.3	Principal component analysis.....	92
4.3.4	Modal composition and terrestrial array .....	96
4.4	Discussion .....	98
4.4.1	Representativity of the dataset .....	98
4.4.2	Serpentinization-related geochemical trends .....	99
4.4.3	Porosity and redox state of iron.....	100
4.5	Conclusions .....	104
5	Conclusions .....	106
	Bibliography.....	109
	Appendices.....	138
	Appendix A Supplementary Material for Chapter 2 .....	138
	Appendix B Supplementary Material for Chapter 3 .....	139
	Appendix C Supplementary Material for Chapter 4 .....	148
	Appendix D Copyright Permissions.....	149

## List of Tables

Table 2 - 1. Sampling depth and lithologic information on the analyzed TAG samples.....	17
Table 2 - 2. Modal abundance of the mineral associations in TAG samples.....	18
Table 2 - 3. Chemical species used in the thermodynamic models to represent bottom ocean seawater (BSW) and TAG hydrothermal fluid .....	21
Table 3 - 1. Sample names adopted in the main text, summary of analytical techniques employed with obtained voxel dimensions, serpentinization degrees and mineral assemblage .....	49
Table 3 - 2. Estimation of the yearly Mg flux extracted during weathering of serpentinized peridotite .....	71
Table 4 - 1. Results of chemical analyses via WD-XRF, titrations and gravimetric method, and results of CIPW normative calculation .....	87
Table 4 - 2. List of principal components that best describe each property analyzed via PCA....	95

## List of Figures

Fig. 2 - 1. Schematic cross-section of the internal stratigraphy of the TAG mound .....	12
Fig. 2 - 2. $\delta^{34}\text{S}$ vs depth at the TAG-1 area.....	16
Fig. 2 - 3. Nodular pyrite texture .....	24
Fig. 2 - 4. Anhydrite replacement by pyrite .....	26
Fig. 2 - 5. Textures indicative of paragenetic relationships .....	27
Fig. 2 - 6. Paragenetic sequence of the minerals identified within the nodular texture .....	28
Fig. 2 - 7. Pressure-Temperature phase diagram showing the homogenization conditions and isochores of fluid inclusion assemblages .....	30
Fig. 2 - 8. Results of thermodynamic modelling.....	32
Fig. 2 - 9. Conceptual model for the formation of nodular pyrite textures observed within the TAG mound .....	38
Fig. 3 - 1. Samples investigated in this study.....	48
Fig. 3 - 2. Orthoslices presenting the results of FIB-SEM analyses and grain-scale observations. ....	56
Fig. 3 - 3. Orthoslices depicting the results of core-scale observations from $\mu$ -CT data sets.....	57
Fig. 3 - 4. Tomographic volumes reconstructed from FIB-SEM and $\mu$ -CT data sets.....	59
Fig. 3 - 5. Pore size distribution (PSD) of statistically significant quantifications.....	60
Fig. 3 - 6. Plots of Euler characteristic values as a function of the equivalent spheric diameter..	62
Fig. 4 - 1. Ternary diagram showing the lithologic classification of the peridotite protolith of the analyzed serpentinites .....	87
Fig. 4 - 2. Correlation matrix .....	92

Fig. 4 - 3. Histogram showing the spread in values of the properties included in the PCA analysis ..... 93

Fig. 4 - 4. Results of the PCA analysis ..... 94

Fig. 4 - 5. Geochemical trends related to mineralogic modes..... 97

Fig. 4 - 6. Geochemical evolution of altered peridotites..... 98

Fig. 4 - 7. Porosity and Fe redox distribution against serpentinization degree monitored via water content..... 103

# 1 Chapter 1 Introduction

The evolution of the Earth's lithosphere is governed by the changing environmental conditions that rocks experience during their geologic lifespan. The transformation of a mineral assemblage to a different one, e.g., Na-amphibole replaced by omphacite during the eclogitization of blueschists, depends strongly on changing pressure and temperature conditions that make the primary mineral assemblage thermodynamically unstable. The newly formed mineral assemblage will form only if it leads to a decrease of the free energy of the system. Consequently, the evolution of mineral assemblages has traditionally been understood as a metamorphic process where mineral assemblages, their geochemical composition, and preserved microtextures are proxies for the pressure-temperature conditions that generated them (Eskola, 1920; Turner, 1948). In this sense, metamorphic rocks were understood as passive recorders of the pressures and temperatures imposed by tectonic processes, sparking the adoption of pressure-temperature-time (PTt) paths that allow to characterize and interpret the geologic history of metamorphic rocks (England and Thompson, 1984). The transformation of a mineral species to a different one requires transport of chemical species. The immense timespan available for geological processes, quantified in the order of millions of years via isotopic dating of rocks, suggested that solid-state diffusion processes could provide effective mechanisms to explain the observed mineral transformation (Barrer, 1951). However, it has become increasingly recognized that fluids provide an alternative and more efficient pathway for mineral transformation (Putnis et al., 2019), particularly because they dramatically extend the length-scale at which chemical equilibration processes can occur. In fact, the length scale at which diffusion-driven reactions operate even across millions of years can extend only to the order of hundreds of meters (Yoder, 1955), and fails to explain mineral

transformation at regional scales, e.g., the albitization of plagioclase in metamorphic terrains that can affect several km<sup>3</sup> of rocks (Kondratiuk et al., 2015). On the other hand, the past three decades have seen a rising recognition of the importance and ubiquity of fluids in metamorphic processes (Yardley, 2009). Fluids reduce the activation energy required at the onset of chemical reactions, enhancing the kinetics of mineral transformation via mechanisms like pressure solution creep or fluid-enhanced grain boundary migration (Peach et al., 2001; Rubie, 1986), and enhance transport by adding an advective component to diffusional transport. Moreover, fluids do not only serve a catalytic role by enhancing reaction kinetics, but affect the thermodynamics of mineral transformations by changing the chemical potential of fluid-mobile elements, as fluids transport solute that can actively participate in mineral reactions (Putnis and Austrheim, 2010; Putnis and John, 2010). The recognition of the role of fluids in metamorphic processes has prompted the reconsideration of classic models used to interpret the evolution of metamorphic rocks (Barrer, 1951; Bowen and Tuttle, 1949; Eskola, 1920; Thompson, 1983; Turner, 1948). Partial mineral replacements that generate corona textures and symplectites at the interface between two mineral species were classically considered to form by solid-state diffusion mechanisms and to represent a frozen snapshot of the pressure-temperature conditions under which local equilibrium was attained between the mineral species that compose the symplectite (Ashworth et al., 1992; Clarke and Powell, 1991; Misch and Onyeagocha, 1976). However, recent studies have shown that symplectitic textures can be reproduced at laboratory conditions via hydrothermal synthesis and that coarsening of the texture occurs ~1000 times faster in the presence of fluids (Zhao et al., 2017). Whereas the classical views identified corona textures as an indication of attainment of local thermodynamic equilibrium between the minerals that form the corona texture, the new conceptual

model states that equilibrium (if any) is attained between a metamorphic fluid and the secondary minerals formed in the corona (Putnis and John, 2010).

Fluid-rock interactions require the presence of pathways that allow continuous contact between fluids and rocks for the duration of the reaction. These fluid pathways are the pores, which are a dynamic property of rock systems and evolve concomitantly with the mineral transformations experienced by rocks. Porosity is the ratio between the volume of voids in a rock and bulk volume of that rock (Hook, 2003). During mineral transformation reactions, porosity can form due to (i) differences in molar volume between the primary and secondary minerals, or (ii) due to differences in their solubilities (Putnis and Austrheim, 2010). In case (i) if the primary mineral has a greater molar volume than the secondary one (assuming that the reaction is isochemical) the volumetric difference is the pore space. If the primary mineral has a lower molar volume than the secondary one, over time the mineral replacement will stop due to armoring of the reactive surface of the primary mineral. Alternatively, the volumetric expansion can exert enough stress on the host rock leading to brittle failure and generation of fracture porosity (Kelemen and Hirth, 2012; Plümper et al., 2012). In case (ii) if the dissolution rate of the primary mineral is faster than the precipitation rate of the secondary mineral, the difference in kinetic rates will be balanced by the generation of new pores. Pseudomorphic reactions are a special case where the rates of dissolution and precipitation become spatially and temporally coupled, so that dissolution of the primary mineral leads to in situ precipitation of the secondary species in a thin interfacial fluid located at the reaction front (Putnis, 2009). There are several distinctive features that characterize pseudomorphic replacement reactions and help to identify them (Putnis and Austrheim, 2010): (i) they are isovolumetric reactions, thus the secondary products preserve the overall size and shape of the primary minerals they replaced; (ii) they show sharp reaction fronts, which cannot form

purely by means of diffusive transport; (iii) the mineral products can preserve crystallographic information inherited from the parent mineral, thanks to the epitaxial nature of pseudomorphic replacements; (iv) new pores form in the mineral products, acting as fluid conduits that enable the infiltration of reactive fluids and solute to the reaction front, self-sustaining the replacement reaction. An example of pseudomorphic reaction is serpentinization, which will be treated further in Chapters 3 and Chapter 4. A special type of porosity is found within the grain boundaries of minerals. Because rocks can be defined as aggregates of natural minerals, and even monomineralic rocks are polycrystalline, every rock type contain myriads of grain boundaries that separate its mineral components. Therefore, even in the case of an unfractured, nominally impermeable rock, grain boundaries exist and represent an almost ubiquitous expression of porosity. They can provide efficient pathways for pervasive fluid flow, as shown experimentally during the replacement of Carrara marble by calcium phosphate (Jonas et al., 2013). In fact, fluid infiltration was observed to be more than one order of magnitude faster along the grain boundaries of calcite compared to the progression of the reaction front towards the unreplaced mineral core through the reaction-induced porosity. Chapter 3 will show examples of the coarsening of porosity at grain boundaries during low-temperature seafloor weathering of serpentinized peridotites.

All the research presented in this thesis has been performed on rock cores recovered via oceanic drilling, thanks to the efforts of the International Ocean Discovery Program (IODP), and its earlier iterations, namely Deep Sea Drilling Project (DSDP), Ocean Drilling Program (ODP), and Integrated Ocean Drilling Program. Scientific ocean drilling has resulted in exceptional discoveries as the presence of hydrothermal vents at the seafloor, and allowed to test important constitutive hypothesis of modern geology as plate tectonics. Moreover, scientific ocean drilling has enabled researchers to observe and characterize currently ongoing processes that previously

could only be inferred by studying fossil analogues in ophiolitic bodies. A prominent example of this are seafloor massive sulfide (SMS) deposits that form at hydrothermal vent fields which expression at the seafloor are black smoker chimneys and are comparable to volcanogenic massive sulfide (VMS) deposits found in terrains emplaced on land.

The *Trans-Atlantic Geotraverse* (TAG) is one of the best studied SMS deposits found in proximity of the Mid-Atlantic Ridge and is an exceptional expression of the mineralogic and geochemical alteration that occurs at the seafloor in the presence of seawater-derived hydrothermal fluids. Chapter 2 presents a study conducted on rock cores recovered from the subseafloor of the TAG mound. It describes a mineral replacement reaction that provides a mechanistic explanation for the attainment of the sulfur isotopic signatures of sulfide minerals at TAG, according to the anhydrite buffer model (Ohmoto, 1983). The anhydrite buffer model suggests that the sulfur isotopic signature of H<sub>2</sub>S and sulfide precipitate is buffered by previously precipitated anhydrite, so that the sulfur isotopic composition of sulfide precipitate is controlled by the isotope fractionation factor between sulfate (SO<sub>4</sub>) and sulfide (H<sub>2</sub>S), which increases with decreasing temperature of fluid-rock interaction. For example, the δ<sup>34</sup>S signature of modern seawater is 21‰ and for fluid-rock interactions that occur at 400 °C the isotope fractionation factor between SO<sub>4</sub> and H<sub>2</sub>S is 15‰, leading to the precipitation of sulfide minerals with a resulting δ<sup>34</sup>S signature of 6‰. For fluid-rock interactions that occur at 300 °C the isotope fractionation factor of sulfur is 21‰, resulting in sulfide precipitate with δ<sup>34</sup>S signature of 0‰. Consistently with the anhydrite buffer model, petrographic imaging of the TAG samples analyzed in this thesis and thermodynamic modelling at temperatures consistent both with the results of our fluid inclusion analyses and previously published results indicate that fluid-rock interactions in the subseafloor cause the replacement of anhydrite by pyrite, which is accompanied by textural reorganization of the

mineralogic assemblage that requires the presence of pores located at the replacement front. These pores allow hydrothermal fluids to enter in contact with anhydrite, which liberates sulfur ions in solution that participate to the precipitation of pyrite and affect its isotopic composition according to the anhydrite buffer model. Chapter 2 was published on *Lithos*. Conceptualization, petrographic and microprobe analyses, geochemical modelling, and writing was done by S. Pujatti; microthermometry, writing, and editing by Y. Klyukin; editing and supervision by M. Steele-MacInnis; editing and supervision B.M. Tutolo.

Black smoker chimneys found at hydrothermal vent fields are dramatic expressions of the effects of focused fluid flow in the oceanic lithosphere, and represent localized geochemical anomalies. Chapter 3 explores instead less conspicuous, but extremely more pervasive effects of water-rock interactions that occur at low temperature as cold seawater infiltrates ultramafic lithologies that are widespread at slow-spreading ridges. Specifically, Chapter 3 examines the mechanism and implications of porosity generation during low-temperature alteration of serpentinized peridotite due to seafloor weathering reactions. Tomographic investigation at nanometric and micrometric scales revealed the presence of pores located at the grain boundaries of olivine. We characterized the connectivity of the pore structures by computing values of the Euler characteristic, which is a topologic invariant parameter, i.e., a number that describes a shape or structure regardless of how the system is deformed (Vogel et al., 2010). The pore networks show significant connectivity, suggesting the establishment of open system conditions with respect to seawater. The expected export of dissolved Mg and Si that results from the dissolution of olivine contributes to the chemistry of seawater and can affect the coupled carbonate-silicate cycle. Chapter 3 was published on *Earth and Planetary Science Letters*. Conceptualization, sample preparation, tomographic

analyses, data processing, and writing by S. Pujatti; tomographic analysis and editing by O. Plümper; conceptualization, editing and supervision by B.M. Tutolo.

Chapter 4 investigates the coupled evolution of porosity and chemical properties of abyssal serpentinites recovered at different sites from the seafloor of the Atlantic Ocean. Serpentinization reactions involve generation of  $H_2$  by reduction of water coupled with oxidation of iron that partitions into secondary minerals. Moreover,  $H_2$  in the presence of  $CO_2$  reacts to form  $CH_4$ . Both  $H_2$  and  $CH_4$  sustain metabolic pathways that are consistent with the earliest life forms on Earth. Well-established correlations between density and serpentinization degree of peridotites suggest the presence of a link between their porosity and Fe redox content. Statistical analysis and interpretation of geochemical trends revealed a more complex system than expected, due to the introduction of variability attributed to low-temperature alteration processes that postdate serpentinization reactions. Chapter 4 has been submitted to *Lithos*. Conceptualization, sample preparation, analysis of porosity content, data processing, and writing by S. Pujatti; conceptualization, editing, and supervision by B.M. Tutolo.

## **2 Chapter 2 Anhydrite replacement reaction in nodular pyrite breccia and its geochemical controls on the $\delta^{34}\text{S}$ signature of pyrite in the TAG hydrothermal mound, 26° N Mid Atlantic Ridge**

### **Abstract**

The Trans-Atlantic Geotraverse (TAG) active mound is a seafloor hydrothermal deposit that has been sampled by drilling to the base of its alteration zone, providing a rare opportunity for *in situ* investigation of the effects of water-rock interactions. The  $\delta^{34}\text{S}$  signature of sulfide minerals in seafloor hydrothermal settings is commonly explained by invoking isotopic mixing and fractionation based endmember models. Here, we present textural evidence of the replacement reactions that underlie the fractionation model endmember, found in core samples recovered from the TAG active mound during ODP expedition 158. The samples were obtained at the TAG-1 area, at the transition between shallower pyrite-silica ( $\pm$  anhydrite) breccias and deeper pyrite-silica breccias. The shallower breccias show porous domains associated with anhydrite, quartz and pyrite. Similar textures were also observed in the deeper samples, in which anhydrite is absent. Our results suggest that at stockwork depths, anhydrite is removed during its interaction with hydrothermal fluids, leaving behind pores lined by quartz crystals and partially filled by pyrite. The textural evolution suggests that pyrite grows at the expense of anhydrite, leading to  $\delta^{34}\text{S}$  values in pyrite controlled by the isotopic fractionation factor between  $\text{SO}_4^{2-}$  and  $\text{H}_2\text{S}$ . Our petrographic observations are supported by geochemical modelling at *in situ* temperatures, estimated from analysis of fluid inclusions in quartz. Our interpretation is in agreement with previously published  $\delta^{34}\text{S}$  data from the TAG active mound. Both the highest  $\delta^{34}\text{S}$  signatures in disseminated pyrite and the lowest  $\delta^{34}\text{S}$  signatures in vein-related mineralization, as well as the progressive  $^{34}\text{S}$ -enrichment

with depth recorded by the isotopic stratification at the TAG active mound can be explained based on the temperature at which water-rock interactions occurred. This research provides direct evidence of the mineral replacement processes occurring within the active TAG sulfide mound and their link to established models of isotopic fractionation. The textural evidence for these processes is characterized in detail and can aid the interpretation of the evolution of other seafloor hydrothermal deposits.

## 2.1 Introduction

### 2.1.1 *Background*

The evolution of fluids discharged at seafloor hydrothermal settings is typically explored by analyzing the sulfur isotopic composition of the hydrothermal fluids, and of the mineral precipitates found in vent chimneys and in the subseafloor of the discharge zone. Several studies have employed sulfur isotopic methods to infer the processes affecting hydrothermal fluids during their path from the recharge zone, through the reaction zone, to the discharge zone (e.g., Aoyama et al., 2014; LaFlamme et al., 2018; McDermott et al., 2015; Ono et al., 2007; Peters et al., 2010). However, petrographic evidence of these processes is scarce, due to the intrinsic challenges related to recovering rock sample from seafloor hydrothermal systems located beneath several kilometers of water. The Trans-Atlantic Geotraverse active hydrothermal mound (referred to as TAG or TAG mound from here onward) is one of the few examples of an actively venting seafloor hydrothermal system that has been sampled in the third dimension (Humphris et al., 1995), providing the opportunity to identify rock textures that provide direct evidence of the mineral replacement processes occurring within the subseafloor of hydrothermal systems and affecting the chemistry of venting fluids.

The sulfur isotopic signature of fluids discharged at seafloor hydrothermal vents is primarily set by the processes that occur in the so-called “reaction zone”, a high-temperature domain located in fractured rocks above magma chambers or shallow intrusions where heat drives convective circulation of fluids. In the hot reaction zone, the  $\delta^{34}\text{S}$  of the fluids is dictated by (1) leaching of sulfur from mineral sulfide in the host rock ( $\delta^{34}\text{S} \approx 0\text{‰}$ ; Shanks et al., 1995) and (2) thermochemical sulfate reduction (TSR) of sulfate derived from seawater recharge ( $\delta^{34}\text{S} \approx 21\text{‰}$ ; Rees et al., 1978). TSR is rapid at temperatures above 250 °C and in the presence of fayalite and magnetite; under such conditions sulfate is quantitatively reduced to sulfide (Shanks et al., 1981). However, TSR is estimated to occur from relatively low temperatures (starting from 80-160 °C, Cross et al., 2004 and references therein). While recharging seawater infiltrates the oceanic crust, the majority of its sulfate content will be reduced to sulfide before the recharging fluids reach the reaction zone. Furthermore, due to the retrograde solubility of anhydrite (Blount and Dickson, 1969), most seawater sulfate will precipitate in the form of anhydrite in the recharge zone as fluids are heated above 150 °C (Mills and Elderfield, 1995). Hence, only a limited (< 1 mmol/kg) amount of sulfate actually reaches the reaction zone (Bischoff and Seyfried, 1978). The signature of the resulting hydrothermal fluid can thus be understood on the basis of the relative proportions of sulfur leached from the crustal protolith and sulfur sourced from TSR of seawater sulfate in a *two component mixing model* (Shanks et al., 1995).

During fluid ascent along the upflow conduit towards the discharge zone fluid-rock interactions can further modify the isotopic composition of the hydrothermal fluid. According to the *anhydrite buffer model* (Ohmoto et al., 1983) the  $\delta^{34}\text{S}$  value in hydrothermal  $\text{H}_2\text{S}$  and sulfide minerals is buffered by the sulfur isotopic content of previously precipitated anhydrite that has in turn inherited its  $\delta^{34}\text{S}$  signature from seawater. The resulting  $\delta^{34}\text{S}$  value in sulfide minerals depends on

the equilibrium isotope fractionation factor between  $\text{SO}_4^{2-}$  and  $\text{H}_2\text{S}$ , which is approximately 21‰ at 300 °C and 15‰ at 400 °C, and can explain  $\delta^{34}\text{S}$  range from 0‰ to 6‰ in sulfides (Ohmoto et al., 1983; Ohmoto and Lasaga, 1982; Ono et al., 2007). In natural systems both endmember models will participate in producing the sulfur isotopic signature recorded in sulfides, and coupled analysis of  $^{34}\text{S}$  and  $^{33}\text{S}$  ratios in vent  $\text{H}_2\text{S}$  and sulfide minerals permits inference of the relative contribution of each endmember (Ono et al., 2007).

To date, most studies of sulfide-anhydrite-fluid interaction in seafloor hydrothermal systems have focused on characterizing the isotopic geochemistry of the mineral precipitates and modelling the chemical evolution of the mineral-forming fluids. To build upon this extensive background, we use thermodynamic modelling coupled with textural and fluid inclusion observations of recovered drill cores from the actively venting TAG mound. Together, these data suggest that at TAG (and presumably at other similar seafloor hydrothermal mounds) fluid-rock interactions in the shallow subseafloor affect the isotopic budget of sulfide minerals that precipitate from solution. The mechanism proposed in this study extends on the well-established anhydrite buffer model (Ohmoto et al., 1983) to provide a detailed investigation of the types of fluids responsible for the mineral replacement reactions highlighted. The textural evolution described in this study can help to interpret the rock record sampled at other seafloor hydrothermal settings.

### *2.1.2 Geology of the active TAG mound*

The Trans-Atlantic Geotraverse hydrothermal vent field is situated on the Mid-Atlantic Ridge (26° 08' N) and was first identified in 1972-1973 during the cruises of the Trans-Atlantic Geotraverse project of the National Oceanic and Atmospheric Administration (NOAA) (Rona et al., 1975; Scott et al., 1974a, 1974b). TAG is the only example of an actively venting, basalt-hosted seafloor hydrothermal system formed at a slow-spreading ridge that has been explored through seafloor

drilling, during Expedition 158 of the Ocean Drilling Program (ODP). These efforts resulted in a complete stratigraphic section of the interior of both the mound and the deeper stockwork zone (Fig. 2 - 1), making TAG one of the best studied seafloor hydrothermal mounds on the Mid-Atlantic Ridge.

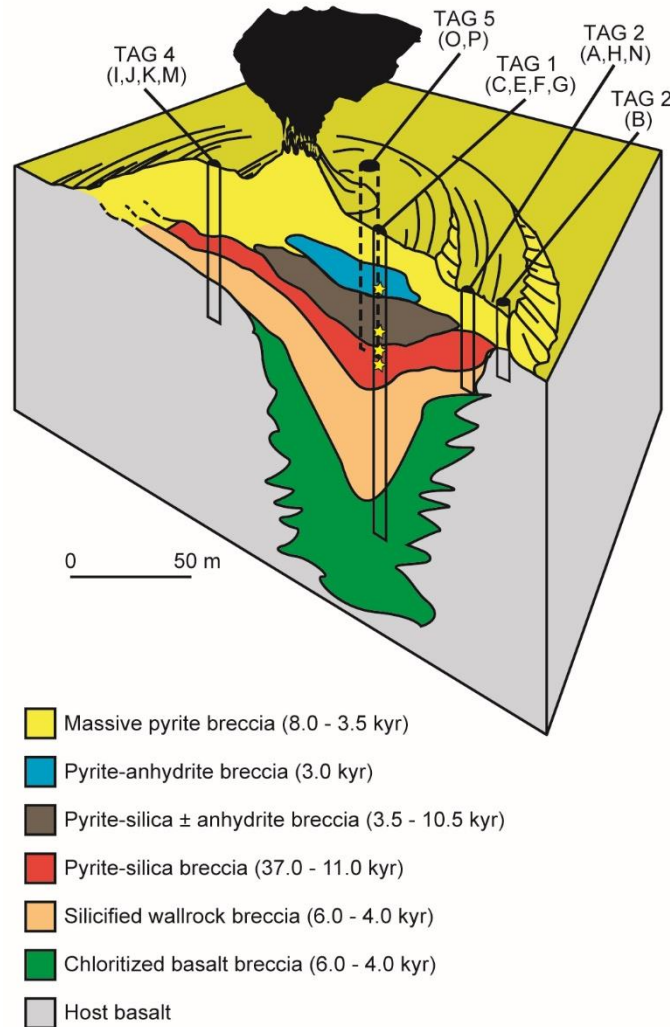


Fig. 2 - 1. Schematic cross-section of the internal stratigraphy of the TAG mound, based on drill cores recovered during ODP Leg 158. Yellow stars show the location of the samples analyzed in this study. Modified after Humphris et al. (1995). The ages reported in the legend are after Lalou et al. (1993); Lalou et al. (1998); You and Bickle (1998).

Geophysical studies have shown that TAG is located on the hanging wall of an active detachment fault (Canales et al., 2007; DeMartin et al., 2007; Tivey et al., 2003). Detachment faulting along

slow-spreading ridges can account for crustal accretion by means of tectonic extension over as much as 50% of the Mid-Atlantic Ridge (Humphris et al., 2015). Seismic surveys have not identified a magmatic heat source at TAG (Canales et al., 2007). Instead, heating of seawater-derived fluid is believed to occur in the root zone of the detachment fault, at depths of more than 7 km (DeMartin et al., 2007).

The internal stratigraphy of TAG (Fig. 2 - 1) is composed of approximately vertically stacked breccias that include: (1) a cover of massive pyrite breccia formed by the accumulated chimney material from the top of the mound down to the first 15 meters below the seafloor (mbsf); (2) an anhydrite zone which consists of pyrite-anhydrite breccia (15-30 mbsf) and pyrite-silica  $\pm$  anhydrite breccia (30-45 mbsf); (3) the stockwork zone made of pyrite-silica and wall rock breccia (45-100 mbsf) that show a progressive enrichment in silica with depth; (4) chloritized basalts (100-125 mbsf, the maximum drilling depth in the TAG area) which are a transitional lithology to the unaltered basalts that host TAG (Humphris et al., 1995).

Most of the seafloor mixing between entrained seawater and upwelling hydrothermal fluids occurs in the pyrite-anhydrite breccia found in (2) the anhydrite zone (Humphris and Tivey, 2000). Pyrite-silica  $\pm$  anhydrite breccia found at the base of the anhydrite zone are a transitional lithology in which the quartz content progressively increases with depth. In pyrite-silica breccia found in (3) the stockwork zone anhydrite is completely removed except for occasional anhydrite-filled veins that mark the penetration of seawater within the mound. From the anhydrite zone to the stockwork, cherty quartz gradually substitutes for anhydrite as the main component in the matrix until no sulfate precipitate is left.

Studies of U-Th isotopes in pyrite and anhydrite grains recovered during dives of the *Alvin* submersible and during ODP Leg 158 reconstructed the timing of the lithologic evolution of the

TAG mound (Lalou et al., 1993; Lalou et al., 1998; You and Bickle, 1998). The pyrite-silica breccias that form the top of the stockwork zone were found to be the oldest, with ages ranging from 37,000 to 11,000 years (You and Bickle, 1998). Dredged samples of this lithology are up to 50,000 years old (Lalou et al., 1993). The second oldest lithology is the pyrite-silica ± anhydrite breccia, which records significant seawater entrainment and consequent precipitation of anhydrite at approximately 10,500 years (You and Bickle, 1998). The oldest massive pyrite breccias found at the top of the mound have ages of 8,000 to 7,000 years (You and Bickle, 1998), showing that, by that stage, the hydrothermal system was evolved enough to show signs of zone refining. The chloritized basalts and wall rock breccias that define the outer portions of the interior of the mound are dated 6,000 to 4,000 years (You and Bickle, 1998). The youngest ages are recorded in sulfide specimens from the very top of the mound and the pyrite-anhydrite breccias that form the bulk of the anhydrite zone, which are 3,600 to 2,200 years old (Lalou et al., 1993; You and Bickle, 1998). TAG experiences episodic hydrothermal activity with stages of quiescence that can last more than ten times longer than the intervening episodes of active venting (Lalou et al., 1993; Lalou et al., 1998; You and Bickle, 1998).

### 2.1.3 $\delta^{34}S$ signatures at TAG

The isotopic signature of sulfur is expressed in this work in standard ( $\delta$ ) notation as permil difference to the Vienna-Canyon Diablo Troilite (V-CDT) reference:

$$\delta^{34}S = \left( \frac{(^{34}S/^{32}S)_{Sample}}{(^{34}S/^{32}S)_{V-CDT}} - 1 \right) * 1000 \quad \text{Eq. 2-1}$$

The  $\delta^{34}S$  values of sulfide minerals analyzed from TAG core samples range from 0.4‰ to 10.3‰ (Gemmell and Sharpe, 1998). This range is similar to the  $\delta^{34}S$  signatures found at other sediment-starved seafloor hydrothermal systems hosted in basaltic rocks, for example on the South Middle

Atlantic Ridge (SMAR) or at site along the southern East Pacific Rise (EPR), where sulfides record  $\delta^{34}\text{S}$  values that range from 1.5‰ to 8.9‰ (Peters et al, 2010) and 0.9 to 8.9‰ (Marchig et al., 1990, 1997), respectively. The  $\delta^{34}\text{S}$  values found in sulfide at ultramafic-hosted hydrothermal system like Rainbow show a broader range, from 0.5‰ to 12.5‰ (Lein et al., 2001; Rouxel et al., 2004).

The distribution of average values of  $\delta^{34}\text{S}$  in sulfides at TAG, grouped by textural style, correlates with the type of sulfide precipitate (Gemmell and Sharpe, 1998): disseminated pyrite grains record the highest average  $\delta^{34}\text{S}$  values (8.4‰) whereas sulfides in anhydrite veins have the lowest average  $\delta^{34}\text{S}$  values (6.7‰). Sulfides associated with anhydrite veins occur across most of the drilling depth at TAG, with the deepest sample recovered from a depth of 116.37 mbsf. Disseminated mineralization is instead distributed preferentially in the deeper parts of the active mound, extending from the pyrite-silica breccia to the deepest part of the stockwork and wallrock breccias.

A vertical profile of  $\delta^{34}\text{S}$  signature in sulfides at TAG reveals an isotopic stratification, where the different stratigraphic zones (Fig. 2 - 1) show progressively  $^{34}\text{S}$ -enriched signatures at increasing depths (Fig. 2 - 2). The highest degree of variability in  $\delta^{34}\text{S}$  values is encountered in the pyrite-anhydrite breccia and pyrite-silica  $\pm$  anhydrite breccia that comprise the anhydrite zone. The isotopic stratification at TAG has been attributed to the distribution of vein-related sulfide mineralization through the hydrothermal mound (Knott et al., 1998), but lacks a genetic model to explain it.

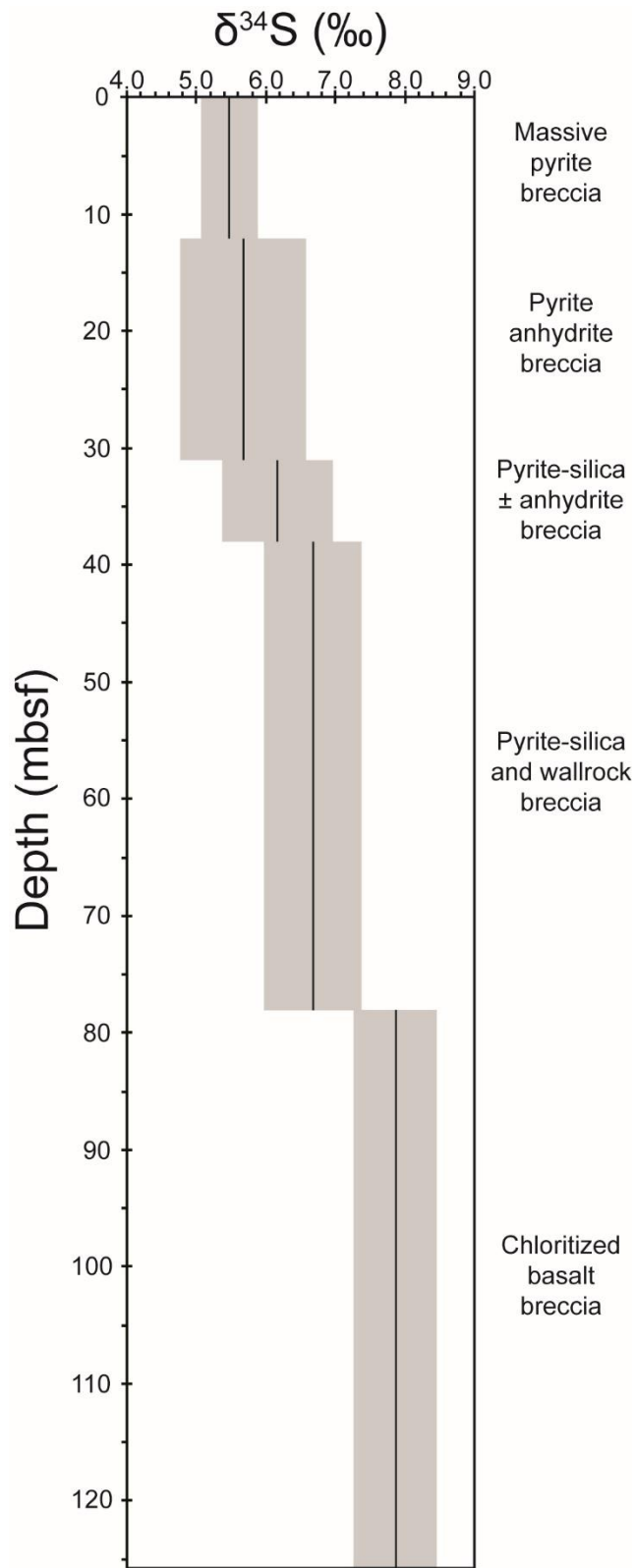


Fig. 2 - 2.  $\delta^{34}\text{S}$  vs depth at the TAG-1 area. Grey shaded areas indicate the standard deviation. Modified after Knott et al., 1998.

#### 2.1.4 Sample selection

The objective of this study is to investigate the mineral replacement reactions that control the textural evolution of rock samples at TAG. We specifically focused on processes that occur where entrained seawater interacts with hydrothermal fluids in the subseafloor as evidenced by the significant amount of sulfate precipitated in the anhydrite zone. Therefore, we selected rock samples from drill core from the anhydrite zone (shallowest) and nearby lithologies, and from greater sampling depths beneath the anhydrite zone. The rationale for this approach is that with increasing depth beneath the mound it is expected that the system will be predominantly permeated by upwelling hydrothermal fluid, rather than seawater entrained from the seafloor. The subseafloor of the TAG mound is made of approximately vertically stacked breccias, thus sample selection following the lithologic sequence through pyrite-anhydrite breccia, pyrite-silica  $\pm$  anhydrite breccia and pyrite-silica breccia enables us to study a partial vertical transect from the anhydrite zone to the stockwork zone (Fig. 2 - 1). With this approach, the textural effects linked to fluid mixing can be differentiated from those related to the action of hydrothermal fluids.

Samples were collected during ODP Leg 158, Site 957 from the TAG-1 area and obtained from the IODP Bremen Core Repository. All analyses were conducted on specimens recovered during coring of Hole C, which was located approximately 20 m south-east of the central upflow conduit that shows black smoker activity. Rock cores recovered from Hole C were chosen because they were most likely to record the highest chemical gradients that would produce more evident rock textures.

Table 2 - 1. Sampling depth and lithologic information on the samples analyzed in this study.

Sample ID	Sample Depth (mbsf)	Lithology	Zone	Comment
-----------	---------------------	-----------	------	---------

7-N-2_71-76	21.56	pyrite-anhydrite breccia	Anhydrite Zone	Sulfide grains in an anhydrite matrix
7-N-2_130-134	22.15	pyrite-anhydrite breccia	Anhydrite Zone	Multiple nodular pyrites surrounded by quartz
13-N-1_132-138	38.52	pyrite-silica $\pm$ anhydrite breccia	Transition to Stockwork	Two compositional domains: massive sulfides, matrix-sustained breccia
15-N-1_86-91	43.06	pyrite-silica $\pm$ anhydrite breccia	Transition to Stockwork	Two compositional domains: anhydrite vein, pyrite-silica breccia
16-N-1_43-47	47.02	pyrite-silica breccia	Stockwork Zone	Widespread nodular texture with pyrite + pores + quartz

We selected 5 core samples on the basis of the rationale described above and sample availability.

A summary of the properties of the sample suite used for this study is shown in Table 2 - 1. The modal mineralogy determined by optical microscopy and electron microprobe analysis is shown in Table 2 - 2, aside from sample 16-N-1\_43-47 which is entirely composed of pyrite and silica.

Table 2 - 2. Modal abundance of the mineral associations recognized by optical microscopy and confirmed by EMP, expressed in wt%. The column titled “13-N-1 Average” reports the mean of the wt% calculated in distinct compositional domains recognized in sample 13-N-1. The same applies to sample 15-N-1\_86-91.

Wt%	7-N-2_71-76	7-N-2_130-134	13-N-1 Average	15-N-1 Breccia	15-N-1 Vein	15-N-1 Average
Chalcopyrite	5.1	3.5	2.6	/	3.3	1.6
Pyrite	52.5	44.1	66.2	47.6	10.0	29.8
Anhydrite	35.1	47.0	2.7	7.8	80.7	42.2
Silica	7.2	5.4	28.6	44.7	6.0	26.4

## 2.2 Methods

### 2.2.1 Petrographic analysis

Petrographic inspections were carried out in transmitted and reflected light on standard thin sections (30  $\mu\text{m}$  thick) and thick sections from quarter core samples (150  $\mu\text{m}$  thick). The thin sections were cut and polished dry (without water) and the thick sections were prepared using oil as the lubricant in order to preserve anhydrite. A total of 5 quarter core samples were studied (Table 2 - 1). Optical microscopy showed a mineral assemblage of pyrite, anhydrite, quartz and minor chalcopyrite.

Elemental analyses of minerals in the thin sections were obtained using wavelength-dispersive X-ray spectroscopy (WDS) mapping with a JEOL JXA 8200 Electron Microprobe (EMP) at the University of Calgary Laboratory for Electron Microbeam Analysis. Maps covering an area of 1  $\text{cm}^2$  were obtained on a representative portion of each sample; two samples (13-N-1 and 15-N-1) showed evident zonation of the mineral distribution in two distinct compositional domains and hence two maps were obtained. The EMP was operated at 20 kV with a spot size of 1  $\mu\text{m}$ , a dwell time of 15 ms and a current of 30 nA. Further details on the standardization of EMP analyses and the analytical procedure used to quantify the modal mineralogy in the thin sections are reported in Appendix A.

Cathodoluminescence (CL) observations were made on a FEI Quanta 250 FEG environmental field emission scanning electron microscope (SEM) equipped with a Gatan MonoCL4 Elite detector at an accelerating voltage of 7.5 keV at the University of Calgary Laboratory for Electron Microbeam Analysis.

### 2.2.2 *Microthermometry*

We analyzed fluid inclusions (FI) hosted in quartz in two samples: 7-N-2\_71-76 and 7-N-2\_130-134. For fluid inclusion analysis, the samples were prepared as doubly-polished 150  $\mu\text{m}$  thick sections by Burnham Petrographics (Rathdrum, Idaho). These sections were examined petrographically to identify coeval fluid inclusion assemblages (FIAs; Goldstein and Reynolds, 1994), which were categorized as primary or secondary assemblages according to petrographic criteria. Only inclusions within well constrained FIAs were subsequently analyzed by microthermometry, and, if present, at least three inclusions per FIA were analyzed in order to check for internal consistency. Microthermometry was done using a Linkam THMS600 heating/freezing stage at the Department of Earth and Atmospheric Sciences, University of Alberta. Temperature measurements were calibrated using synthetic fluid inclusions according to the triple point of  $\text{CO}_2$  at  $-56.6\text{ }^\circ\text{C}$ , the triple point of  $\text{H}_2\text{O}$  at  $0.0\text{ }^\circ\text{C}$ , and the critical point of  $\text{H}_2\text{O}$  at  $373.9\text{ }^\circ\text{C}$ . Salinity of the fluid inclusions was calculated using the last melting temperature of ice (Bodnar, 1993). Pressure at homogenization, bulk density, and isochore were calculated using the Driesner (2007) and Driesner and Heinrich (2007)  $\text{H}_2\text{O}$ - $\text{NaCl}$  equation of state, as implemented by Klyukin et al. (2019, 2020). Isochores were then projected from the temperature and pressure of homogenization to the estimated trapping pressure. Trapping pressures were estimated as hydrostatic pressure at the depth at which the samples were collected: samples 7-N-2\_71-76 and 7-N-2\_130-134 were retrieved at a depth of 21.56 mbsf and 22.15 mbsf respectively, with a water column above Hole C at the TAG-1 area that is 3548 m deep. Hence, we estimated trapping pressures of  $\sim 360$  bar for both samples.

### 2.2.3 Thermodynamic modelling

Thermodynamic modelling was carried out with the Geochemist's Workbench (GWB) software package (Bethke et al., 2018) version 12.0.6 with a 0-400 °C, 350 bar thermodynamic database created using the DBCreate software package (Kong et al., 2013), based upon thermodynamic data for minerals and aqueous species previously compiled by Simmons et al. (2016). The React module was used to calculate mineral saturation curves.

Table 2 - 3. Chemical species used in the thermodynamic models to represent bottom ocean seawater (BSW) and TAG hydrothermal fluid. All concentrations are mmolal.

Chemical Species	BSW	TAG Black Smoker
O <sub>2(aq)</sub>	0.1	/
H <sub>2(aq)</sub>	/	0.37
H <sub>2S(aq)</sub>	/	6.7
HCO <sub>3</sub> <sup>-</sup>	2.3	3.4
SO <sub>4</sub> <sup>2-</sup>	27.9	/
NO <sub>3</sub> <sup>-</sup>	0.0003	/
NH <sub>4</sub> <sup>+</sup>	/	0.65
SiO <sub>2(aq)</sub>	0.16	22
Na <sup>+</sup>	464	584
Cl <sup>-</sup>	546	659
Br <sup>-</sup>	0.84	1.045
K <sup>+</sup>	9.8	18
Al <sup>3+</sup>	0.00002	0.01
Ca <sup>2+</sup>	10.2	26
Mg <sup>2+</sup>	52.7	0
Fe <sup>3+</sup>	0.0000015	/
Fe <sup>2+</sup>	/	5.17
Ba <sup>2+</sup>	0.00014	0.02
Mn <sup>2+</sup>	0	0.71

Cu <sup>2+</sup>	0.000007	0.13
Zn <sup>2+</sup>	0.00001	0.083
Pb <sup>2+</sup>	0	0.00011

BSW composition from Bruland (1983) and McCollom (2007, 2008). TAG Black Smoker fluid composition from Campbell et al. (1988), Douville et al. (2002) and Charlou et al. (1996, 2002); NH<sub>4</sub><sup>+</sup> from maximum values shown in Tivey (2007) for the case of mid-ocean ridges.

Representative values were chosen for the chemical composition of bottom ocean seawater (BSW) (Bruland, 1983; McCollom, 2007, 2008) and the hot hydrothermal fluid (Campbell et al., 1988; Charlou et al., 1996, 2002; Douville et al., 2002; Tivey, 2007) exhaled from the black smoker vents at TAG. The species modelled and the values used for their concentrations are reported in Table 2 - 3. Equilibrium path calculations in Janecky and Seyfried (1984) have shown that the precipitation of Ca sulfate occurs rapidly upon mixing, and seawater can be heated conductively up to 240 °C before it mixes substantially with hydrothermal fluids. Furthermore, modelling studies examining the Sr isotopic composition of anhydrite at TAG show that seawater must be preheated conductively before mixing with hydrothermal fluids in order for the mixed fluid to become supersaturated with respect to anhydrite (Chiba et al., 1998; Teagle et al., 1998). To reflect such conditions in our models, BSW was heated to 200 °C before fluid mixing. The inputs in our models included the *in situ* pH, calculated by heating a fluid of BSW composition to 200 °C and a TAG hydrothermal fluid to 380 °C. The following endmember scenarios were modelled: (1) simple conductive cooling of upwelling hydrothermal fluids with TAG black smoker composition and (2) mixing between BSW and the TAG hydrothermal fluid. Mineral precipitation was suppressed in these models to investigate the maximum saturation state achievable by the mineral precipitates. The curves describing saturation states are shown only for the mineral phases recognized by optical microscopy and EMP. In the mixing model, a fluid with BSW composition was speciated at 2 °C, heated to 200 °C, and reacted with a TAG hydrothermal fluid with an initial

temperature of 380 °C in a 1:1 mass ratio, so that 1 kg of hydrothermal solution reacted with 1 kg of BSW. Instead of employing a temperature of 350 °C to represent the maximum temperature of the hydrothermal fluids, according to our FIA results, we choose to use 380 °C to represent the whole range of temperature conditions likely experienced within the TAG mound at the TAG-1 area. In fact, the highest trapping temperatures estimated by FIA at TAG are on the order of 380 ° - 390 °C (Petersen et al., 1998).

Conductive cooling of a TAG hydrothermal fluid was modelled from 380 °C to 0 °C. The saturation state of pyrite was investigated at the conditions in which hydrothermal fluid reacts with anhydrite in the wall rock under water/rock ratios of 1, 10 and 100.

Water/rock ratios (W/R) reported in this study are defined on a mass basis, so that a W/R of 1 corresponds to 1 kg of solution interacting with 1 kg of solid.

## 2.3 Results

### 2.3.1 Petrographic textures

#### 2.3.1.1 Nodular pyrite

We characterized the petrographic relationships in rock samples recovered from the vertically stacked lithologies of pyrite-anhydrite breccia, pyrite-silica ± anhydrite breccia and pyrite-silica breccia that constitute a partial vertical transect across the TAG mound. Pyrite grains showing a distinctive nodular texture are present in samples sourced from all the studied lithologies, although the associated mineral assemblage varies with increasing depth.

In samples of pyrite-anhydrite and pyrite-silica ± anhydrite breccias, millimeter-scale subhedral grains of pyrite are surrounded by rims of subhedral quartz that forms coronas with bipyramidal prismatic habit, suggesting inward growth into open space (Fig. 2 - 3a). The crystal size of this

type of quartz is 100-250  $\mu\text{m}$ , which is distinctively coarser than the cherty quartz that replaces anhydrite in the matrix (10-30  $\mu\text{m}$ ). Between the quartz coronas and the sulfide, fragments of anhydrite and pores can be seen (Fig. 2 - 3a, 2 - 3b, 2 - 3e).

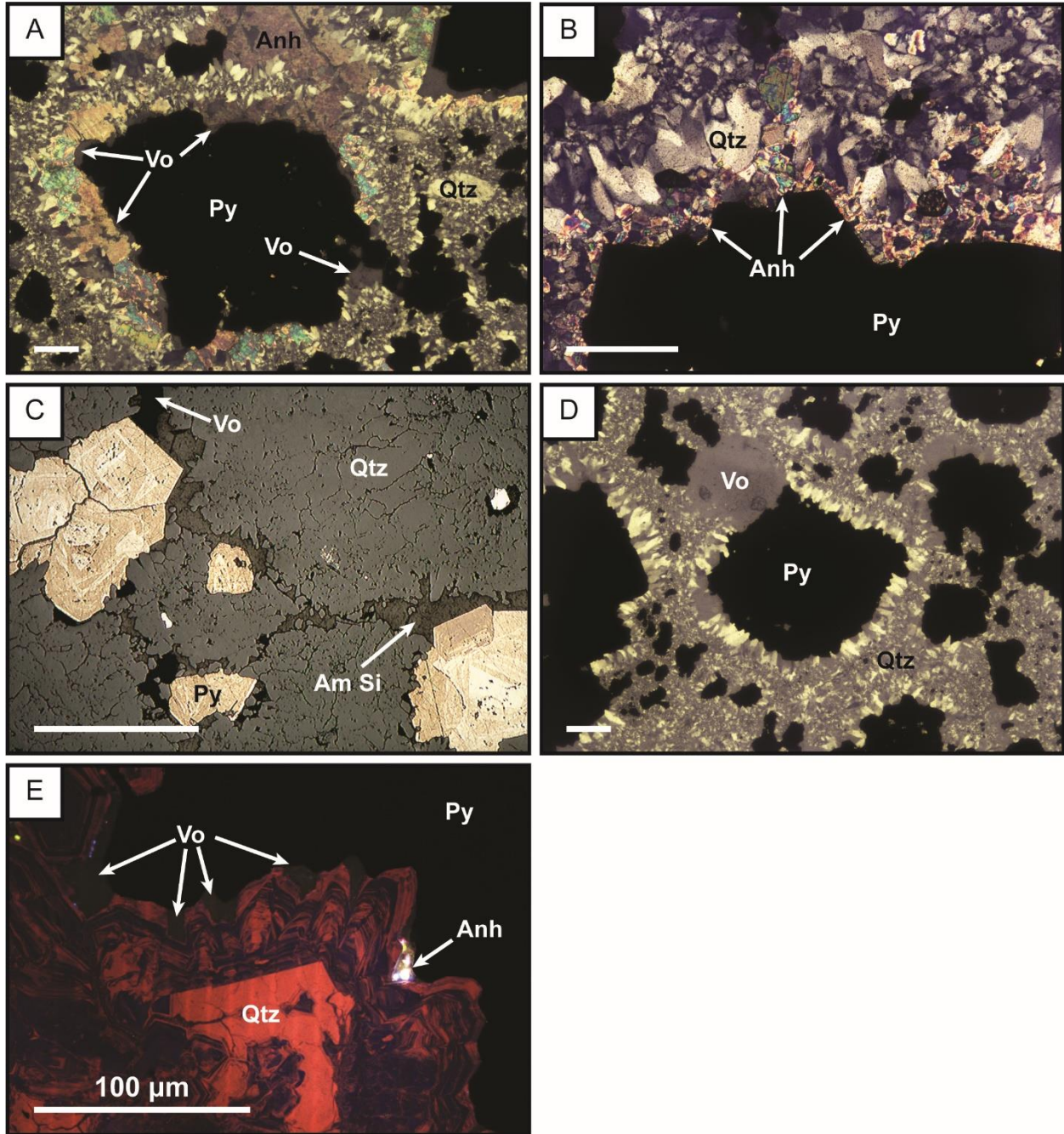


Fig. 2 - 3. Nodular pyrite texture. Images a, b and d acquired under cross-polarized, transmitted light, whereas c was collected under reflected light, and e is an SEM-cathodoluminescence image. Anh =

anhydrite; Py = pyrite; Qtz = quartz; Vo = voids (pores). a) Association of subhedral pyrite and quartz with anhydrite and pores, giving a nodular appearance, sample 13-N-1\_132-138. b) Interface of the nodular texture from the anhydrite zone, sample 7-N-2\_130-134. c) Pyrite grains disseminated in a matrix of quartz aggregates, crosscut by veins partially filled with amorphous silica. Pyrite shows euhedral crystal faces when it grows into the veins, whereas the faces in contact with quartz are irregular and associated with pores, sample 15-N-1\_86-91. d) Defining texture in stockwork zone samples. Subhedral pyrite associated with residual porosity surrounded by coronas of coarse-grained, sub-euhedral quartz and disseminated in a matrix of microcrystalline quartz, sample 16-N-1\_43-47. e) Growth zonation in euhedral quartz grown in open space (labeled Vo). Residual anhydrite is present at the interface between pyrite and quartz, sample 15-N-1 86-91. All scale bars are 250  $\mu\text{m}$ , except in Fig. 2 - 3e where the scale bar is 100  $\mu\text{m}$ .

Similar textures are also present in the stockwork sample (sample 16-N-1\_43-47). Here, nodular clasts of pyrite have coronas of subhedral quartz and pores that lack anhydrite, which has been completely removed from the system (Fig. 2 - 3c-d). The intermediate stage between the anhydrite zone and stockwork zone is recognized in samples from the transitional pyrite-silica  $\pm$  anhydrite breccias, which preserve small fragments of anhydrite ( $\sim 20 \mu\text{m}$ ) that fill the pore space between quartz and pyrite, standing as evidence of the progressive removal of anhydrite with increasing depth (Fig. 2 - 3e). The CL texture of quartz in Fig. 2 - 3e shows euhedral growth zones of oscillating CL intensity associated with pores, which is likely the result of hydrothermal growth of quartz into open space (Rusk, 2012).

### *2.3.1.2 Mineral replacement reaction*

The formation of the nodular texture identified in TAG samples requires the presence of hydrothermal fluids simultaneously undersaturated with respect to anhydrite and supersaturated with respect to pyrite, so that the former mineral can be removed from the system to permit open space growth of quartz and pyrite, with the latter forming wide, millimeter-scale nodules. Petrographic observations confirm the former presence of such hydrothermal fluids in samples 7-N-2 and 13-N-1 (recovered from the anhydrite zone and the transitional breccias): anhydrite shows widespread evidence of dissolution in the form of triangular and cubic etch pits (Fig. 2 - 4a), and fragmentation due to mechanical reworking within the mound (Fig. 2 - 4a-b). Textures of pyrite

suggest replacement of anhydrite: pyrite appears to nucleate in etch pits and grows along the grain boundaries of anhydrite (Fig. 2 - 4a, 2 - 4b). Furthermore, the grain boundaries of pyrite were commonly observed to impinge into adjacent anhydrite (Fig. 2 - 4c).

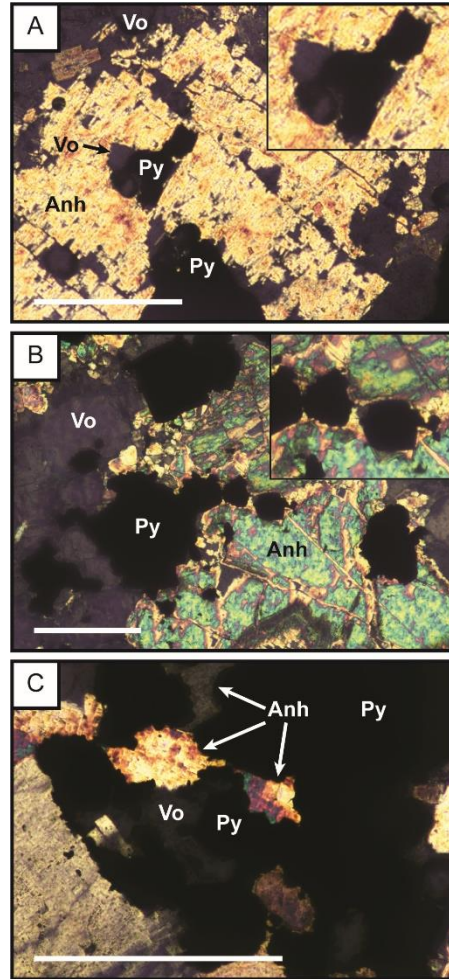


Fig. 2 - 4. Anhydrite replaced by pyrite. All photomicrographs were acquired by cross-polarized, transmitted light. Anh = anhydrite; Py = pyrite; Qtz = quartz; Vo = voids (pores). a) Triangular and polygonal etch pits in anhydrite that are partly filled by pyrite, shown in detail in the inset, sample 7-N-2\_130-134. b) Pyrite grows from etch pits, fractures and along the grain boundaries of anhydrite, highlighted in the inset, sample 7-N-2\_71-76. c) The grain boundaries of pyrite bulge into anhydrite, sample 13-N-1\_132-138. All scale bars are 250  $\mu\text{m}$ .

### 2.3.1.3 Paragenetic sequence

Establishing a precise paragenetic sequence in the TAG-1 area samples is challenging due to the dynamic and episodic character of fluid circulation within the mound (Lalou et al., 1993; Lalou et

al., 1998; You and Bickle, 1998), which causes overprinting and recrystallization of the mineral assemblage precipitated during early growth stages. However, a few textural observations can aid in determining the paragenetic relationships between the mineral phases recognized within the nodular texture.

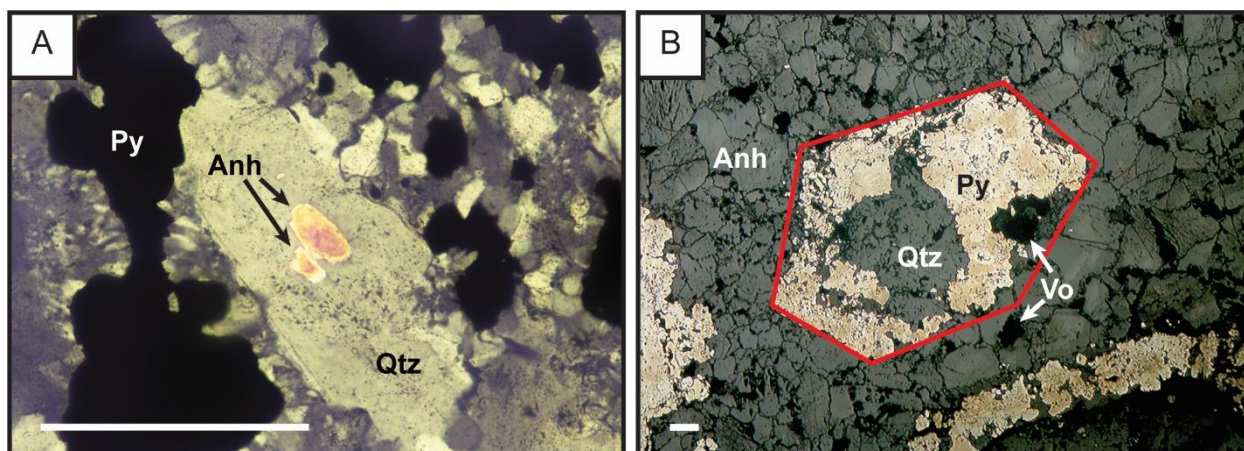


Fig. 2 - 5. Textures indicative of paragenetic relationships. Anh = anhydrite; Py = pyrite; Qtz = quartz; Vo = voids (pores). a) Crystals of anhydrite are enveloped within a coarse crystal of quartz, resembling a poikilitic texture. Sample 13-N-1\_132-138, cross polarized transmitted light. b) A grain of marcasite pseudomorphically replaced by an assemblage of pyrite and quartz (outlined in red), embedded in a matrix of coarse-grained anhydrite. The association of pyrite with quartz suggests that their growth stages overlapped at least partially, allowing replacement of marcasite while preserving enough structural integrity to produce a partial pseudomorph, sample 7-2-N\_71-76, reflected light. All scale bars are 250  $\mu\text{m}$ .

Firstly, we observed inclusions of anhydrite completely enclosed within a single coarse quartz crystal (Fig. 2 - 5a). The host quartz does not show healed fractures that could have allowed the penetration of seawater; therefore, we interpret this observation as evidence of anhydrite formation prior to the precipitation of quartz. Secondly, samples 7-N-2 and 13-N-1 show examples of pyrite intergrown with aggregates of quartz, forming prismatic crystal shapes with pyramidal terminations that are pseudomorphic replacements of early mineral precipitate (Fig. 2 - 5b). In principle, both anhydrite and marcasite can crystallize with the habit shown in Fig. 2 - 5b. However, anhydrite in the matrix has a distinctively smaller grain size than the pseudomorph, and it does not show euhedral morphologies or coarse grain sizes similar to the replaced grain in Fig.

2 - 5b. Hence, it is more likely that these pseudomorphs formed after marcasite rather than anhydrite. In fact, the inversion of marcasite to pyrite is known to occur under hydrothermal conditions (Yao et al., 2020) and marcasite is metastable compared to pyrite at all temperatures relevant for this study (Gronvold and Westrum, 1976; Yao et al., 2020). Furthermore, pseudomorphs of pyrite after marcasite have already been recognized at TAG (Knott et al., 1998). Finding quartz in association with pyrite in these pseudomorphic replacement products suggest that the growth stage of these minerals can overlap.

The same nodular texture highlighted in this section was also recognized during ODP Leg 158 (Knott et al., 1998) and in a fossil hydrothermal system in Cyprus (Plate 3.27 in Constantinou, 1972). The paragenetic sequence that leads to the formation of the nodular texture is summarized in Fig. 2 – 6.

Mineral	Anhydrite Zone	Transitional Zone	Stockwork Zone
Anhydrite	<b>██████████</b>	-----	
Pyrite	<b>██████████</b>	<b>██████████</b>	<b>██████████</b>
Quartz		-----	<b>██████████</b>
Chert	-----	<b>██████████</b>	<b>██████████</b>

Fig. 2 - 6. Paragenetic sequence of the minerals identified within the nodular texture. Solid bold lines indicate that the mineral is abundant and is one of the main constituents in samples from a specific zone. Dashed lines mark minerals that were present only sporadically.

### 2.3.2 Fluid Inclusions

We analyzed fluid inclusion assemblages (FIAs) hosted in quartz to constrain the temperatures of processes that formed the textures in the anhydrite zone. The FIAs identified in the samples are secondary, trapped along healed fractures (Fig. 2 - 7, left inset). The fluid inclusions (FI) are invariably two-phase and liquid-rich at room temperature. Fluid inclusions within any individual FIA showed consistent microthermometric properties and homogenized to the liquid phase (Fig. 2

- 7, right inset). Rarely, FI initially appeared to be vapor-rich at room temperature; however, these "vapor-rich" inclusions showed ice-melting temperatures identical to those of the accompanying liquid-rich inclusions, and did not homogenize at temperatures exceeding 500 °C. As such, these "vapor-rich" inclusions are interpreted as partially leaked FIs.

First melting was observed near -20 °C, consistent with the eutectic temperature of fluids in the system H<sub>2</sub>O-NaCl. Last ice-melting temperatures ranged between -1.9 and -3.3 °C, corresponding to salinities from 3.2 to 5.5 wt% NaCl (Bodnar, 1993). The measured temperatures of homogenization ( $T_h$ ) vary between 310 and 360 °C, and average  $T_h$  of individual FIA ranged from 320 to 345 °C (Fig. 2 - 7). Trapping temperatures inferred from the intersection between estimated trapping pressures and isochores (Fig. 2 - 7), range between 367 °C and 348 °C in sample 7-N-2 71-76 (average 355 °C) and between 356 °C and 350 °C in sample 7-N-2 130-134 (average 352 °C). We measured a total of 23 FIs, belonging to 7 different FIAs. The total number of inclusions measured for each FIA ranged from 2 to 5. Averaged  $T_h$  vs salinity plot for each FIA, total number of FI measured in each FIA, and standard deviations are reported in the inset in Fig. 2 - 7.

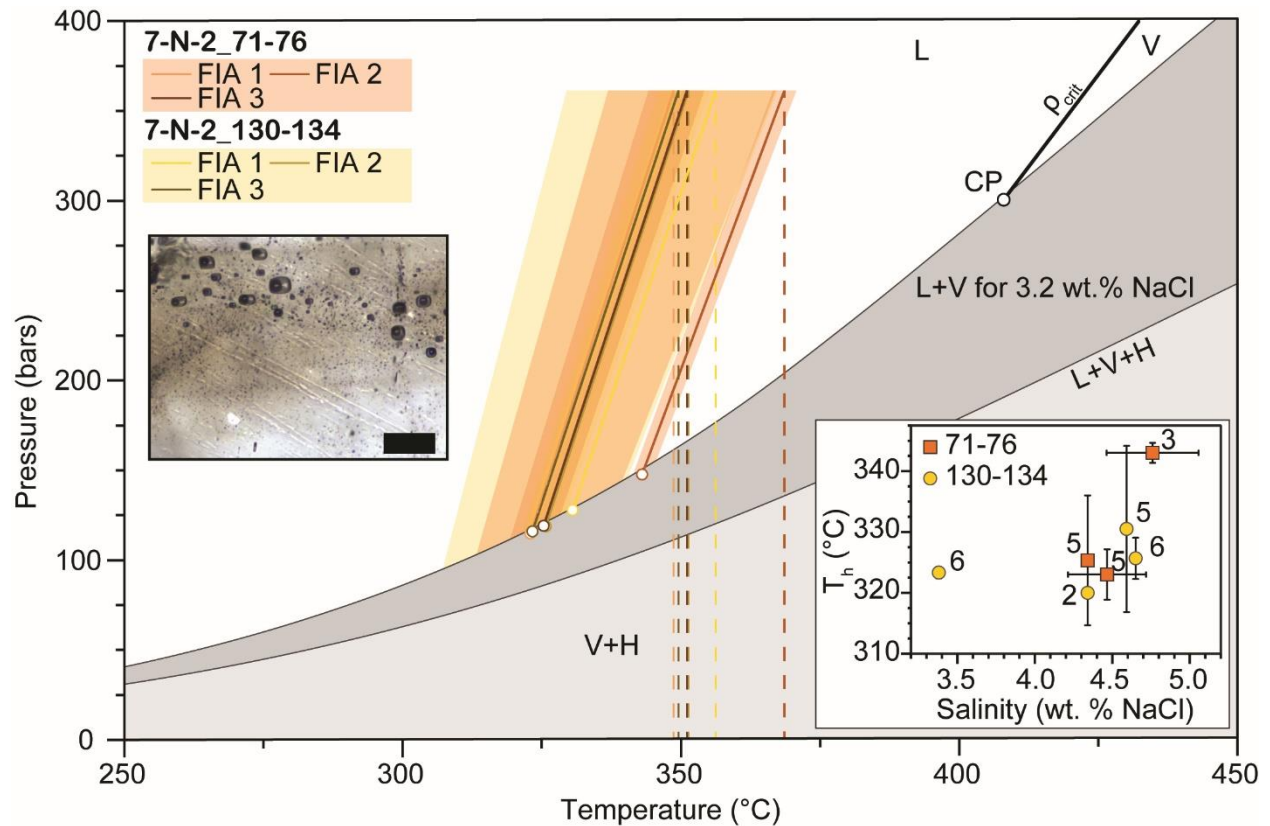


Fig. 2 - 7. Pressure-Temperature phase diagram showing the homogenization conditions and isochores of fluid inclusion assemblages from samples 7-N-2\_71-76 and 7-N-2\_130-134. The dark gray-shaded region represents the region of liquid-vapor immiscibility (L+V), the light gray-shaded region represents the region of vapor-halite immiscibility (V+H) for a bulk composition of 3.2 wt% NaCl (seawater salinity). Also shown are the critical point (CP) and critical isochore (thick black line labeled  $\rho_{crit}$ ) for a fluid of 3.2 wt% NaCl. Solid lines indicate isochores of fluid inclusion assemblages. The colored regions represent the full range of homogenization conditions and isochores for all individual FIs. The dashed lines project to the trapping temperatures estimated at 360 bar. The inset on the bottom-right corner shows the salinities of the FIAs against homogenization temperatures ( $T_h$ ), averaged for each FIA with error bars indicating standard deviation. The number next to the data point indicates the number of individual fluid inclusions contained in FIA. The inset on the left reports a composite (focus-stacked) photomicrograph showing representative fluid inclusion assemblages from sample 7-N-2\_130-134. The black scale bar on the bottom-right is 25  $\mu\text{m}$ . The exact number of FI analyzed in each FIA, as well as its average position and standard deviation are shown in the inset.

### 2.3.3 Modelling saturation states

Thermodynamic modelling was used to predict the saturation state of the minerals recognized by EMP mapping in two endmember cases: mixing and conductive cooling. The first involves mixing between bottom seawater (BSW) and upwelling TAG hydrothermal fluid (Fig. 2 - 8a); the second simulates conductive cooling of the TAG hydrothermal fluid in the absence of anhydrite or in the

presence of varying masses of anhydrite (Fig. 2 - 8b). In both models, quartz is slightly supersaturated across the whole temperature range. Anhydrite shows distinctively different behaviors: the interaction between seawater and hydrothermal fluids (Fig. 2 - 8a) causes anhydrite supersaturation at 366 °C and low degrees of mixing (4 % seawater, 96 % hydrothermal fluid). Simulations in which the hydrothermal fluid was set to temperatures higher than 380 °C resulted in anhydrite becoming supersaturated at higher temperatures (not shown). During conductive cooling (Fig. 2 - 8b), anhydrite is undersaturated across the whole temperature range, likely owing to the reducing nature of the unmixed hydrothermal fluids. The saturation state of pyrite during mixing (Fig. 2 - 8a) is several orders of magnitude higher than that of anhydrite across most of the temperature range. During cooling of the hydrothermal fluids due to mixing, pyrite becomes thermodynamically stable from a temperature of 370 °C and low degrees of mixing (3% seawater, 97% hydrothermal fluid). In the case of conductive cooling (Fig. 2 - 8b), pyrite becomes supersaturated at 288 °C, a lower temperature than in the case of mixing because the conductive cooling scenario lacks a supply of seawater sulfate. When the hydrothermal fluid is reacted with a mass of anhydrite, simulating the interaction with wall rock precipitate, pyrite becomes supersaturated after minimal degrees of cooling and attains the highest supersaturation at low water/rock ratios (W/R) (Fig. 2 - 8b).

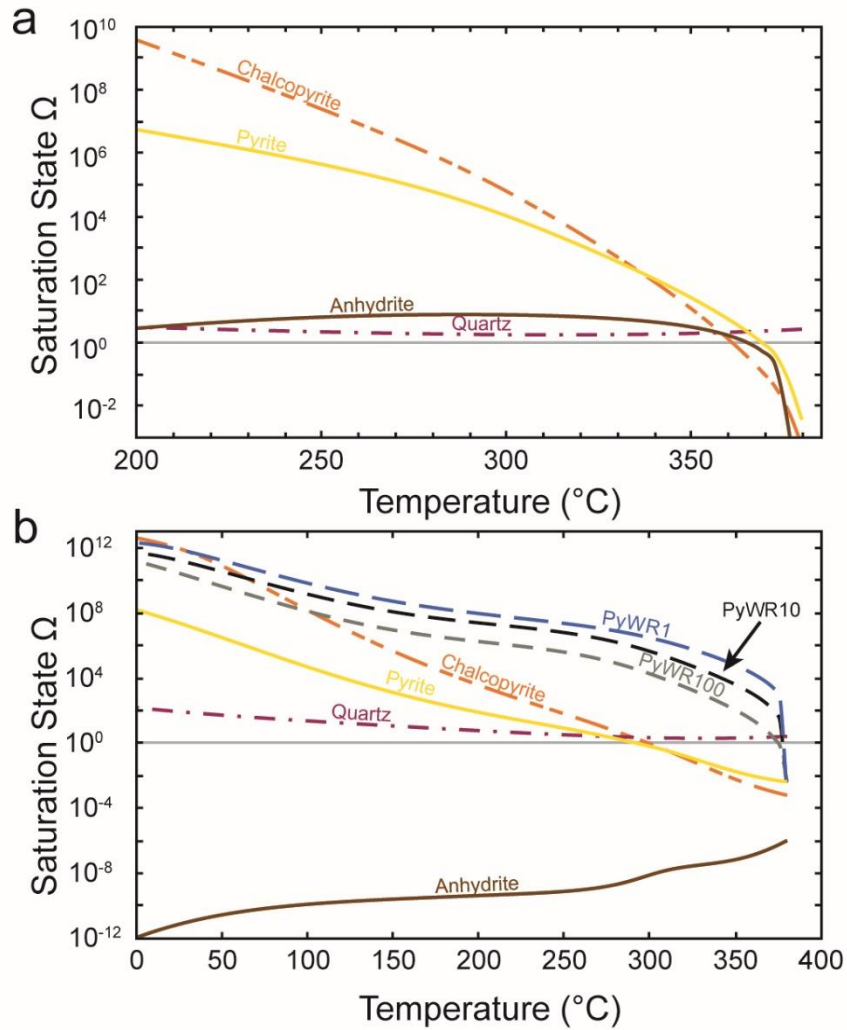


Fig. 2 - 8. Results of thermodynamic modelling. a) Mineral saturation state versus temperature during mixing between BSW and TAG hydrothermal fluid. Anhydrite is supersaturated across most of the simulated temperature range. The solid grey line indicates equilibrium saturation conditions. b) Mineral saturation state versus temperature during conductive cooling of TAG hydrothermal fluids. The curves labelled PyWR1/PyWR10/PyWR100 show the saturation state of pyrite when the hydrothermal fluid reacts with anhydrite under water-rock ratios of 1, 10 and 100, respectively.

## 2.4 Discussion

### 2.4.1 Anhydrite dissolution

Self-organization of mineral distributions within the TAG mound due to water-rock interactions produce the distinctive rock textures described in this study. These provide direct evidence of the

mineral replacement steps involved in the isotopic fractionation process described by the anhydrite buffer model.

Anhydrite in samples recovered from core 7-N-2 shows clear signs of dissolution expressed either by triangular or polygonal etch pits or by fragmentation of large crystals of anhydrite found in the matrix (Fig. 2 - 3b, 2 - 4a). Fragmentation is caused by processes that lead to physical disruption within the mound, such as tectonic activity, fluid overpressure, or collapse during stages of hydrothermal quiescence (Knott et al., 1998). Fluid overpressure could also be responsible for the formation of the large crystals of anhydrite in the matrix of samples from the anhydrite zone, because it can relieve several meters of lithospheric load and thereby permits crystal growth into open space (Knott et al., 1998). Dissolution of anhydrite at TAG can be caused by: (i) cooling during local seawater recharge within TAG or during stages of hydrothermal inactivity, due to the retrograde solubility of anhydrite (Blount and Dickson, 1969); or (ii) the interaction with sulfate undersaturated, low density, high temperature hydrothermal fluids (Scheuermann et al., 2019; Woodruff and Shanks, 1988). Case (ii) is depicted in Fig. 2 - 8b, which shows that during conductive cooling of TAG hydrothermal fluids anhydrite is undersaturated across the entire simulated temperature range.

We interpret the textures observed as a product of dissolution of wall rock anhydrite under the action of hot hydrothermal fluids (Scheuermann et al., 2019) that have not mixed significantly with seawater and are thus sulfate-undersaturated (Woodruff and Shanks, 1988). Pyrite partly fills etch pits in anhydrite (Fig. 2 - 4a) and grows from etch pits and fractures in anhydrite (Fig. 2 - 4b), which suggests that the dissolution of anhydrite and growth of pyrite are tightly coupled.

If, instead, anhydrite dissolution at TAG were caused by seawater infiltration without mixing with hydrothermal fluids, for example during a phase of hydrothermal quiescence, there would be no

drive to precipitate sulfides because seawater is oxidized, and sulfur dominantly occurs as sulfate. Anhydrite at depth is localized in veins (up to 45 cm thick) that are recognized down to the base of the stockwork zone at 125 mbsf (Knott et al., 1998). This type of mineralization implies that, after limited degrees of mixing between seawater and hydrothermal fluid, anhydrite becomes supersaturated and precipitates *in situ*, along the infiltration pathways.

Closed system conditions with respect to seawater, required to let relatively unmixed hydrothermal fluids interact with anhydrite, could be attained as anhydrite itself precipitates in the mound during fluid mixing (Fig. 2 - 8a), clogging pores and leading to shielding of internal portions of the mound. Local seawater entrainment can lead to anhydrite precipitation by means of conductive heating, without the need to enter in direct contact with the upwelling hydrothermal fluids. As this process continues, an impermeable anhydrite barrier can form that separates focused hydrothermal flow from diffuse flow (Lowell et al., 2003).

Anhydrite becomes supersaturated during mixing when the hydrothermal fluid cools below 366 °C, which matches the maximum venting conditions reported at TAG (Tivey et al., 1995). This suggests that the interior of the TAG mound is an extremely dynamic chemical environment, where anhydrite can both precipitate and dissolve, in very close spatial proximity, depending on the local geochemical conditions.

#### 2.4.2 *Anhydrite replacement by pyrite*

We observed pyrite replacing anhydrite, growing in etch pits, fractures, and along the grain boundaries of anhydrite (Fig. 2 - 4). Pyrite also replaces fragmented anhydrite (Fig. 2 - 3b) which is likely highly reactive due to its higher reactive surface area compared to the coarser crystals of anhydrite. Pyrite is also commonly seen impinging on and replacing anhydrite (Fig. 2 - 4c).

The fluid responsible for the replacement of anhydrite by pyrite must have been simultaneously undersaturated with respect to anhydrite and supersaturated with respect to pyrite. This condition is only met over a narrow temperature interval from 366 °C to 370 °C (Fig. 2 - 8a) during seawater-hydrothermal fluid mixing, whereas fluid inclusions analysis indicates that the replacement took place at temperature of ~350 °C. Hence, it is unlikely that mixing was the dominant mechanism responsible for the observed replacement reactions. During conductive cooling of hydrothermal fluids, however, the fluid is simultaneously undersaturated with anhydrite and supersaturated with respect to pyrite only when the fluid cools below 288 °C. Nevertheless, anhydrite is abundant throughout the hydrothermal mound, and thus could provide a source of sulfur, which, in turn, could contribute to pyrite growth. At geologically realistic fluid-to-anhydrite ratios of 1, 10, and 100, dissolving anhydrite can provide an effective source of sulfur that can increase the saturation state of pyrite by up to 6 orders of magnitude (Fig. 2 - 8b). Supersaturation can, in turn, facilitate the nucleation and growth of pyrite in the mound after even modest degrees of conductive cooling of the hydrothermal fluid. Therefore, the model shown in Fig. 2 - 8b seems capable of explaining the textures in Fig. 2 - 3 and 2 - 4.

#### 2.4.3 *Nodular texture and related growth processes*

Our petrographic investigation included samples from pyrite-anhydrite breccias that make up the anhydrite zone *sensu stricto*; pyrite-silica breccias that make up the top of the stockwork zone; and the pyrite-silica ± anhydrite breccia that forms a transitional layer between the first two lithologies. These observations therefore constitute a partial vertical transect through the TAG hydrothermal mound. A distinctive texture was recognized in samples from the stockwork zone, in which disseminated coarse-grained pyrite with nodular appearance was surrounded by porosity and a rim of coarse-grained quartz that commonly showed bladed and prismatic bipyramidal habits. Quartz

crystals were organized radially around pyrite, with the crystallographic *c* axis aligned perpendicular to the external surface of the sulfide grains (Fig. 2 - 3d). Similar textures were recognized in shallower samples, showing less internal organization and the presence of anhydrite occupying parts of the pores between quartz and pyrite (Fig. 2 - 3a-b).

The samples from the transitional pyrite-silica  $\pm$  anhydrite breccias show instances of coarse-grained quartz enveloping anhydrite in a poikilitic-like texture (Fig. 2 - 5a). This texture implies that the mineral inclusions formed before the host quartz. As anhydrite is buried to greater depths where quartz becomes more stable, as evidenced by the progressive increase in silica content of the breccia (Fig. 2 - 1), it is replaced by quartz and occasionally preserved as mineral inclusion.

Pyrite associated with an aggregate of subhedral quartz with bladed and prismatic habit, similar to the quartz variety observed rimming pyrite at depth, was observed pseudomorphically replacing a large crystal of marcasite (Fig. 2 - 5b). The phase transition from marcasite to pyrite can occur spontaneously in hydrothermal environments at high temperatures (Yao et al., 2020). This texture therefore suggests that the association of pyrite and eu/subhedral quartz occurs during hydrothermal flow at high temperature, which is more representative of the interactions with an unmixed hydrothermal fluid rather than a mixed fluid that is cooled by the interaction with cold seawater.

The paragenetic relationships inferred from Fig. 2 - 5a and 2 - 5b imply that samples from the anhydrite zone are experiencing the incipient stage of microstructural organization of the minerals composing the nodular texture, which attains full developed in the deeper stockwork samples that are predominantly affected by quartz-saturated, hot and relatively unmixed hydrothermal fluids. The coarse crystals of quartz that appear to be indenting pyrite are evidence of growth of quartz into open space, as would be expected in the presence of porous pathways surrounding the nodular

sulfide grains. Such pathways work as conduits that deliver hot hydrothermal fluids to the interface between anhydrite and pyrite, enabling simultaneous dissolution of anhydrite and precipitation of pyrite. In samples from the transitional pyrite-silica  $\pm$  anhydrite breccias traces of anhydrite were found in pores at the interface between pyrite and quartz grown in open space conditions (Fig. 2 - 3e).

Our geochemical models show that the fluids responsible for the formation of the nodular texture are predominantly of hydrothermal origin. The fact that this texture is observed more commonly at depth and becomes the defining texture of rocks in the stockwork is consistent with our models (Fig. 2 - 8b). Mixing will be predominant at shallow depths within the anhydrite zone, whereas hydrothermal fluids undergoing conductive cooling will be dominant at depth, where seawater infiltration is less prevalent.

The considerations above permit inferences about the processes governing the internal growth of the hydrothermal mound over time. Since the incipient textural stages are found in shallow samples and become more advanced with depth, the surface that defines the boundary between the anhydrite zone and the stockwork zone must migrate upwards over time, following the direction of the channelized fluid flow. Conversely, the base of the stockwork zone should migrate towards greater depths over time, as increasingly larger volumes of basalt become hydrothermally altered. This process will continue until cessation of hydrothermal venting occurs. Several causes can cease fluid flow, for example: a) tectonic deformation, which can lead to internal reworking of the plumbing of the mound, cutting off the vent system from the heat source at depth; b) cooling of the heat source itself; c) variations in fluid pathways due to mineral dissolution and precipitation processes.

A summary of the processes responsible for the formation of the nodular texture is presented in the conceptual model in Fig. 2 - 9.

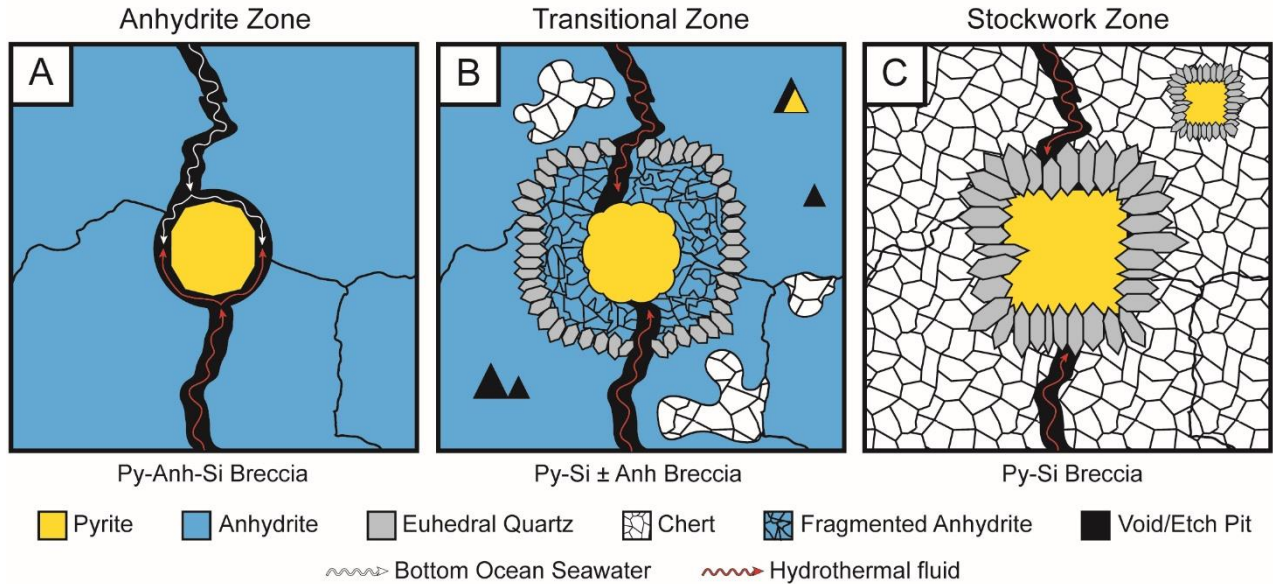


Fig. 2 - 9. Conceptual model for the formation of nodular pyrite textures observed within the TAG mound. a) In the anhydrite zone, pyrite grains are disseminated in a matrix made of coarse-grained anhydrite, which precipitates during mixing of BSW and hydrothermal fluids. b) With progressive aging the rocks are buried to depth, migrating to a transitional layer permeated dominantly by anhydrite-undersaturated hydrothermal fluids: (i) etch pits form and can be partly filled by pyrite; (ii) aggregates of chert replace anhydrite in the matrix; (iii) anhydrite becomes fragmented and replaced by bulging pyrite. A rim of coarse grained eu/subhedral quartz forms around the disseminated pyrite, where anhydrite has dissolved permitting the growth of quartz into open space. c) Further burial brings the rocks into the stockwork zone, where anhydrite is completely removed from the system and replaced by cherty quartz in the matrix. Pyrite and quartz within the nodular texture grow and attain eu/subhedral habit.

#### 2.4.4 $\delta^{34}\text{S}$ stratigraphy at TAG

The stratification of sulfur isotopic signatures observed at TAG shows a progressive increase in  $\delta^{34}\text{S}$  values from an average of 5‰ in the surficial massive pyrite breccias to an average of 8‰ in the stockwork zone (Fig. 2 - 2). This distribution of isotopic values can be explained in terms of isotopic exchange occurring in the near-surface environment within the TAG mound at progressively lower temperatures as the fluid gets closer to the seafloor, according to the prediction of the anhydrite buffer model (Ohmoto et al., 1983). The highest variability in  $\delta^{34}\text{S}$  signatures in

sulfides at TAG is found in the pyrite-anhydrite breccia and pyrite-silica  $\pm$  anhydrite breccia that make the anhydrite zone (5.2‰ to 7.1‰). Most fluid mixing is expected to occur in the anhydrite zone, thus it is the region where the highest variability in chemical conditions occur, depending on the relative proportion of entrained seawater against upwelling hydrothermal fluid that interact at each point in time.

According to the anhydrite buffer model, if isotopic equilibration occurred at 350 °C, which is a representative average temperature estimated from FIAs in this study, the resultant H<sub>2</sub>S would have a  $\delta^{34}\text{S}$  value of 4.1‰ (Ohmoto et al., 1983; Ono et al., 2007). The average  $\delta^{34}\text{S}$  values in sulfide minerals at TAG is 6.4‰ (Herzig et al., 1998), thus isotopic fractionation likely does not always proceed to equilibrium due to limited residence time of the fluids beneath the hydrothermal mound. The lowest and highest  $\delta^{34}\text{S}$  values at TAG are found in association with (i) anhydrite veins and (ii) disseminated mineralization, respectively (Knott et al., 1998). The association with anhydrite in group (i) implies presence of entrained seawater under mixing conditions and an accompanying cooling of the hydrothermal fluid. The evolution of the sulfur isotopic composition will be dictated by the fractionation factor between  $\text{SO}_4^{2-}$  and H<sub>2</sub>S, which increases with decreasing temperatures, resulting in a mixed fluid with progressively lower  $\delta^{34}\text{S}$  values (Ohmoto et al., 1983). Linking the case of disseminated mineralization (ii) to our results is less straightforward, because the term “disseminated” used in the early work on TAG is a qualitative descriptor subject to interpretation. In Knott et al. (1998), disseminated pyrite found in pyrite breccias is described as “disseminated in late silica in vugs”, and quartz in these rocks is seen as “Mostly vuggy polycrystalline aggregates... with clear euhedral halos around Py aggregates” and in deeper rocks that are part of the altered wall rock basalt as “fine microcrystalline aggregates... [forming] halos around disseminated pyrite”. Importantly, these descriptions match with the characterization of the

nodular texture that was highlighted in this study. Provided that disseminated pyrite grains displaying nodular textures have grown according to the mechanism proposed in this study, the disseminated sulfides have reached the textural maturity depicted in Fig. 2 - 9b and 2 - 9c. According to our interpretation they would be found in textural domains that interact prevalently with hot hydrothermal fluids. Isotopic fractionation between  $\text{SO}_4$  derived from dissolving anhydrite and the  $\text{H}_2\text{S}$  in the hydrothermal fluid would thus occur at higher temperature and producing higher  $\delta^{34}\text{S}$  values when compared with sulfides in group (i) of vein-related mineralization.

## 2.5 Conclusion

In this study, core samples recovered from Hole C in the TAG-1 area during ODP Leg 158 have been investigated by means of petrographic and modelling techniques. In summary:

- Pyrite was commonly observed bulging into anhydrite, growing from its etch pits and replacing fragmented anhydrite, which are features indicative of a mineral replacement reaction.
- Pores associated with pyrite, anhydrite, and quartz are organized in a nodular texture which evolves with depth. Anhydrite is gradually lost from the matrix, which is overgrown and replaced by cherty aggregates of microcrystalline quartz.
- Interpretation of the textures allows us to identify the direction of growth of the interface between anhydrite and stockwork zone at TAG.
- Thermodynamic modelling suggests that anhydrite is undersaturated in hydrothermal fluids that are undergoing conductive cooling, which are likely to predominantly affect the

stockwork zone. To precipitate pyrite at elevated temperatures, these fluids have to interact with previously precipitated wall rock anhydrite.

- When a seafloor hydrothermal system like TAG presents a developed anhydrite zone, the  $\delta^{34}\text{S}$  signature of  $\text{H}_2\text{S}$  in the upwelling hydrothermal fluid and recorded by precipitated sulfides will be modified according to the prediction of the anhydrite buffer model.
- Our model is consistent with the stratification of  $\delta^{34}\text{S}$  values at TAG and can explain the distinct distributions of sulfur isotopic values between vein-related and disseminated mineralization.

The availability of rock core samples from the entire stratigraphic section found at TAG permitted the study of progressive “snapshots” that record the spatial and temporal evolution of mineral assemblages and replacement textures in the lithologies that make the interior of the TAG mound. Such a record is representative of the modern geologic history of the interior of the mound and enables us to make inferences about the processes that control its growth, which otherwise can only be inferred indirectly via geophysical studies (Pontbriand and Sohn, 2014) or from the evolution of the surficial bathymetry in time (Barreyre et al., 2012).

**Acknowledgments.** This research used samples and data provided by the International Ocean Discovery Program (IODP). We acknowledge the support of the Natural Sciences and Engineering Research Council of Canada (NSERC) for providing funding for this research under Discovery Grant numbers RGPIN-2018-03800 and RGPIN-2018-04370. We would like to extend our gratitude to Karin Los for help in sample selection from the Bremen Core Repository, Robert Marr for helping with EMP acquisition, Christopher Debuhr for his help with SEM CL analysis, and

Mickey Horvath for preparing our samples. The authors wish to thank Crystal Laflamme, an anonymous reviewer and Cecile Prigent for their critical comments which helped to improve the interpretations, structure and overall clarity of this paper.

### **3 Chapter 3 Weathering-driven porosity generation in altered oceanic peridotites**

#### **Abstract**

Ultramafic rocks exposed at slow and ultra-slow spreading mid-ocean ridges represent a significant and extremely reactive portion of the oceanic lithosphere. Thus, mechanistic understanding of the processes by which seawater infiltrates into and reacts with these rocks is essential for constraining their contribution to the chemistry of the oceans and the coupled carbonate-silicate cycle. Recent observations indicate that nanoscale processes contribute to seawater-driven alteration of ultramafic rocks, but conventional petrographic and tomographic observations of the associated physical features are challenging to link to these nanoscale features. Moreover, multiple generations and varying conditions of fluid infiltration often obscure the relative roles of higher-temperature serpentinization, where reactions are mostly isochemical, and lower-temperature weathering reactions, where observations suggest the release of massive amounts of magnesium. Here we bridge these scales and investigate the specific role of weathering processes in dissolution-driven porosity generation by integrating focused ion beam scanning electron microscopy nanotomography and micro-computed X-ray tomography imaging of the pore structures preserved in drill cores of serpentinized oceanic peridotites. Relict olivine crystals in all imaged samples contain abundant etch pits, and those in the higher-resolution FIB-SEM imagery show the presence of channel-like dissolution structures. The pore channels preferentially affect olivine along grain boundaries and show anisotropic distribution likely controlled by crystallographic features. The pores formed via olivine dissolution are interpreted to result from dissolution of serpentinized peridotite at conditions where serpentine and carbonate precipitation

are kinetically inhibited, i.e., at weathering conditions. Importantly, the calculated connectivity of the imaged pore structures increases as the scale of investigation increases, suggesting that weathering-driven olivine dissolution facilitates further seawater infiltration and olivine dissolution, a positive feedback that can sustain continued magnesium extraction until the rocks are ultimately cut off from seawater circulation via sedimentation. Thus, while much attention has been directed towards constraining geochemical fluxes from the higher-temperature alteration of ultramafic rocks, our results support literature studies suggesting that mineral dissolution, and hence elemental fluxes, are significant at the lower temperatures of seafloor weathering. Our data thus provide mechanistic evidence of the physical process contributing to the observed elemental loss from weathered oceanic peridotites.

### 3.1 Introduction

Decades of seafloor dredging and oceanic drilling have demonstrated that ultramafic rocks are frequently exposed at slow and ultra-slow spreading mid-ocean ridges (Warren, 2016). They constitute a significant portion of slow-spreading oceanic crust and make up an estimated 20-25% of the crust generated at slow-spreading ridges (Cannat et al., 2010). Ultramafic rocks equilibrate in the lithospheric mantle at high temperature at nominally anhydrous conditions and are, therefore, chemically unstable and thus highly reactive when exposed to near-surface, fluid-saturated conditions (Beinlich et al., 2018). Harzburgites, which are composed of olivine (forsterite-enriched) and orthopyroxene (enstatite-enriched), with minor amounts of clinopyroxene and spinel, represent 75% of the recovered peridotites sampled near the Mid-Atlantic Ridge (MAR), the most frequently sampled slow-spreading ridge environment (Warren, 2016).

Natural samples of oceanic peridotites are typically heavily altered and the primary textures and mineralogic associations are not preserved, except for spinel (Yu and Tikoff, 2020). Alteration

results from the chemical and mineralogic changes that occur during the interaction between ultramafic rocks and seawater and/or hydrothermal fluids. The former case is termed “seafloor weathering”, which consists of (oxidative) alteration of the upper several hundreds of meters of seafloor-exposed ultramafic rocks and is often accompanied by the precipitation of secondary carbonate minerals (Bach et al., 2013; Kelemen et al., 2011). On the other end of the spectrum, the interaction between ultramafic lithologies and hydrothermal fluids includes a series of metasomatic reactions that occur at intermediate to high temperatures (up to ~400 °C) and range from serpentinization to chloritization, epidotization, steatization, rodingization and listvenization (Bach et al., 2013).

The variability of alteration styles that affect ultramafic rocks in the oceanic lithosphere can make it challenging to identify the specific contribution of each reaction process, and the effects of high-temperature hydrothermal reactions can be difficult to separate from low-temperature weathering processes (Bach et al., 2011). Serpentinization is a hydration reaction and the most common type of hydrothermal alteration that affects ultramafic rocks. It is typically accompanied by minimal mobility of major elements, with serpentinization-derived fluids containing minimal concentrations of Mg and SiO<sub>2</sub> (Seyfried et al., 2015), the primary components of the mineral olivine and orthopyroxene of which the rocks are composed. Unfortunately, specific serpentinization reactions can be challenging to recognize, because a single specimen of peridotite can be subject to multiple fluid infiltration events, at varying temperature and pressure conditions, and ultimately be characterized by complex alteration patterns (e.g., Andréani et al., 2007). On the other hand, low-temperature seafloor weathering often overprints the initial, higher-temperature phase of water-driven alteration. It can be expressed in the form of olivine and brucite dissolution (Klein et al. 2020; Snow and Dick, 1995) and accompanying Mg release, or carbonate

mineralization of relict olivine and/or serpentine/brucite (Bach et al., 2011), where Mg can also be mobilized (de Obeso et al., 2021). Thus, it can be extremely challenging to identify the specific alteration processes affecting an ultramafic rock sample and their relative contributions to elemental fluxes. Nevertheless, because of the relative abundance and exceptional reactivity of ultramafic rocks in oceanic settings, it is essential to mechanistically constrain these reaction processes to assess their role in controlling the chemical composition of the oceans and contributing to seafloor weathering feedbacks on the global carbon cycle (Brady and Gislason, 1997; Coogan and Gillis, 2013; Krissansen-Totton and Catling, 2017).

Hydration associated with serpentinization reactions and carbonation associated with seafloor weathering require inputs of H<sub>2</sub>O for the former and CO<sub>2</sub> for the latter, which in turn rely on the presence of pore space. Pores act as pathways that permit the infiltration of fluids and solutes through the rock system to reach pristine mineral surfaces and progress the reaction. Hydration of peridotite can be kinetically limited at low temperatures (Tutolo et al., 2018), whereas carbonation reactions are kinetically fast and typically transport-limited (Xiong and Giammar, 2014), thus their progress is dependent on the ability of fluids and solute to infiltrate into fresh portions of the rock (Kelemen and Hirth, 2012; Plümper et al., 2012; Tutolo et al., 2016). Therefore, the alteration of peridotite can be strongly affected by grain-scale microstructures, which control the local hydrology and determine the spatial distribution of precipitate in the system (Lacinska et al., 2017). Electron microscopy and neutron scattering studies (Andréani et al., 2004; Boudier et al., 2010; Tutolo et al., 2016) have revealed the presence of nanometer-sized pores in altered peridotite, and the spatial distribution of pore structures at micrometric scale has been observed in both experimentally and naturally altered peridotite (Jöns et al., 2017; Osselin et al., 2022).

Here, we bridge observations from nm- to  $\mu\text{m}$ -scale to examine pore structures in serpentinized peridotites and constrain the nature of porosity generation and evolution during the alteration of peridotite. We observe an array of sizeable pores with smooth walls and channel-like morphologies, formed via the dissolution of brucite and/or olivine. The absence of secondary precipitates in these pores demands a mechanism for de-coupling dissolution of Mg-rich minerals from secondary phase precipitation, which is consistent with rapid olivine dissolution and kinetically inhibited Mg-silicate and Mg-carbonate precipitation at the low temperatures of seafloor weathering (below approximately 100 °C, Bach and Früh-Green, 2010; Snow and Dick, 1995). This mechanism opens connected fluid-pathways and increases the susceptibility of ultramafic rocks to seawater-driven chemical and heat extraction. In this way, our findings provide a specific, physical link between observed, multi-scale pore structures and their alteration processes. These findings further help to explain past observations of extensive Mg loss during weathering of oceanic peridotite.

## 3.2 Methods

### 3.2.1 *Geological samples*

The analyzed samples are shown in Fig. 3 - 1, and Table 3 - 1 reports the abbreviated names used throughout the text to refer to the samples, the analytical techniques employed, the resulting voxel dimensions, mineral modes, and serpentinization degree of the samples. The mineral assemblage and modes were estimated via visual inspection of thin section (FIB-1-209, FIB-2-209) and tomographic volumes (Micro209, Micro357, Micro304). A more detailed summary of the drilling sites described in this section can be found in Appendix B, and a scan of the thin section from which FIB-1-209 and FIB-2-209 were collected is shown in Appendix B.

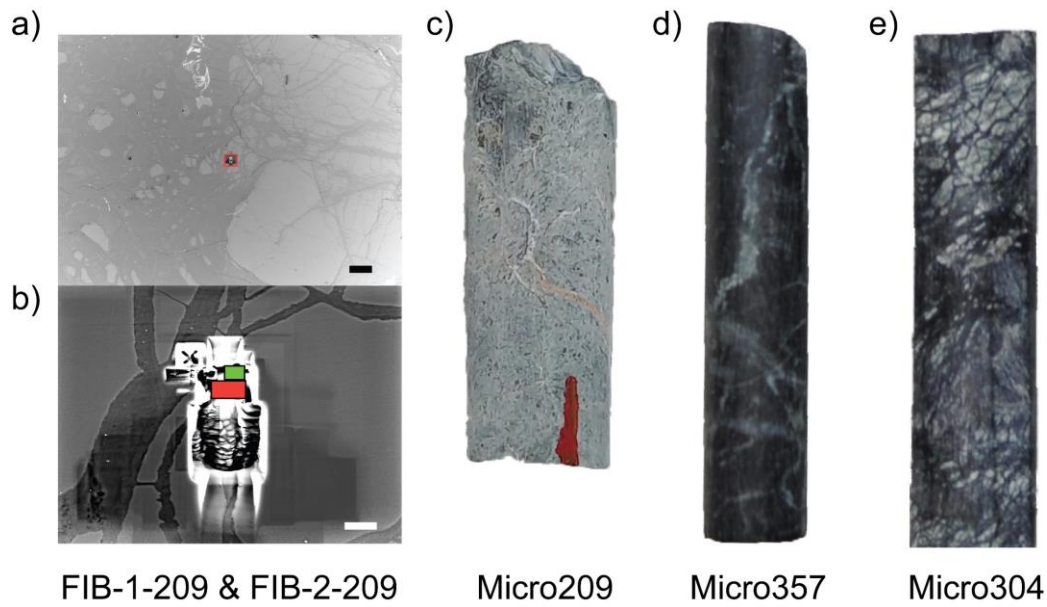


Fig. 3 - 1. Samples investigated in this study. a) BSE image showing the location of FIB-SEM cuttings: the FIB-SEM data sets were acquired from kernel-textured olivine. The large grains on the right side of the image are pyroxene crystals. Black scale bar = 200  $\mu\text{m}$ . b) zoomed image showing the area marked by a red rectangle in Fig. 3 - 1a. The location of FIB-1-209 is marked by the green rectangle, the location of FIB-2-209 is marked by a red rectangle. White scale bar = 10  $\mu\text{m}$ . c) Micro209 (mini)core with approximate diameter of 6 mm. The red marking at the base of the sample was made to ease the identification of its orientation. d) Micro357 (mini)core, with an approximate diameter of 5 mm. A white talc vein can be seen crossing the sample. e) Micro 304 (mini)core, with an approximate diameter of 5 mm. Remnants of pyroxene are light-colored and present throughout the sample.

### 3.2.1.1 Leg 209 data sets FIB-1-209 and FIB-2-209

Ocean Drilling Program (ODP) Leg 209 was carried out in 2003 and resulted in drilling at eight sites from 14°43' to 15°44'N along the Mid-Atlantic Ridge, on well-exposed outcrops of peridotite found on both sides of the rift valley (Kelemen et al., 2004). Leg 209 investigated the processes that control the generation of oceanic lithosphere at magma-starved ridge sections. Site 1274 is the northernmost drill location along the rift valley and is found ~31 km north of the western intersection between MAR and the 15°20' Fracture Zone, recovering mainly peridotites and few meter-scale gabbroic intrusions (Kelemen et al., 2004). Seafloor weathering alteration at Site 1274 is recognized in the uppermost ~90 m of hole penetration in the form of oxidative carbonates and iron oxyhydroxides-clay alteration veins and haloes. Core Section 209-1274-A-3R1 is made

chiefly of harzburgite with subordinate dunite bands that have been heavily serpentinized. Sample 209-1274-A-3R1 61-71 was recovered from a representative portion of the overall core section at ~17.51 meters below seafloor (mbsf) and is delimited at its top and bottom by the presence of orange iron oxyhydroxide and carbonate veins (Kelemen et al., 2004).

Table 3 - 1. Sample names adopted in the main text, summary of analytical techniques employed with obtained voxel dimensions, serpentinization degrees and mineral assemblage.

IODP/ODP sample name	Renamed data set	Analysis technique	Voxel dimensions	Serpentinization degree (%)	Mineral assemblage <sup>a</sup>
ODP 209-1274-A-3R1 61-71	FIB-1-209	FIB-SEM	X, Y = 2 nm; Z = 10 nm	85%	Ol = 6%; prx (+ bastite) = 9%; spl = <1%; srp = 85%
ODP 209-1274-A-3R1 61-71	FIB-2-209	FIB-SEM	X, Y = 8 nm; Z = 10 nm		
ODP 209-1272-A-21R1 55-57	Micro209	μ-CT	X, Y, Z = 1.6 μm	99%	Ol = 1-2%; prx (bastite) = 10%; spl = <1%; srp = >95%
IODP 357-72-B-8R2 47-49	Micro357	μ-CT	X, Y, Z = 1.6 μm	65%	Ol = 7%; prx (+ bastite) = 7%; spl = 1%; tlc = 20%; srp = 65%
IODP 304-1309B-11R1 110-114	Micro304	μ-CT	X, Y, Z = 1.6 μm	75%	Ol = 4%; prx (+ bastite) = 20%; spl = <2%; srp = 75%

<sup>a</sup>Micro209 was almost entirely serpentinized, all the pyroxene was present as bastite recognized by pseudomorphic replacement of serpentine oriented along cleavage planes. Micro357 and Micro304 contained both unreplaced pyroxene and bastite, and the reported % values for Micro357 and Micro304 are a sum of remnant pyroxene plus bastite replacements. Ol = olivine remnants, prx = pyroxene, spl = spinel, tlc = talc, srp = serpentine.

### 3.2.1.2 Leg 209 sample Micro209

Site 1272 was also drilled during ODP Leg 209 and is located on the western flank of the Mid-Atlantic rift valley, close to the top of the inside corner high, south of the 15°20' Fracture Zone. The predominant alteration style identified at Hole 1272A is serpentinization. However, low-

temperature oxidative alteration is also present in the form of red-brown clays and iron oxyhydroxides associated with aragonite veins and iowaite mineralization (Bach et al., 2004; Appendix B). Several faults have been identified at Hole 1272A and their location is signaled by the presence of fault gouge and locally increased veining. Fault gouge is expected to be saturated with fluids and highly conductive to fluid flow compared to the surrounding wallrock (Kelemen et al., 2004). Sample Micro209 was recovered from a depth of ~99.5 mbsf and is made of heavily serpentinized protogranular harzburgite. Pyroxene is only preserved as relictive bastite, as the sample is almost entirely serpentinized, with a low presence of olivine remnants (<2%, Table 3 - 1). Several interpreted faults have been identified in the vicinity of Micro209: at 89.7 mbsf in Section 19R-1; at 99.58 mbsf in Section 21R-1; at 100.6 mbsf in Section 21R-2; at 108.6 mbsf in Section 23R-1.

### *3.2.1.3 Expedition 357 sample Micro357*

International Ocean Discovery Program (IODP) Expedition 357 drilled an east-west transect across the southern wall of the Atlantis Massif, an oceanic core complex (OCC) located ~15 km west of the median-axis valley of the MAR, to investigate potential links between serpentinization processes and their influence on microbial populations in the shallow seafloor. The sample analyzed here was recovered from Hole B at Site 72, located close to the summit of the corrugated detachment surface found on the top of the Atlantis Massif, to the north of the carbonate cap above the Lost City hydrothermal field. Hole B drilled through a section interpreted as a detachment fault zone located in serpentinized peridotite (Früh-Green et al., 2017). Sample Micro357 was recovered from ~12 mbsf from an interval of serpentinized harzburgite that shows the presence of metasomatic talc-chlorite veins and patches. Sample Micro357 contains abundant talc and shows the lowest serpentinization degree reported in this study, with the highest preservation of olivine

remnants. Within the same core section as sample Micro357, shipboard X-ray powder diffraction analyses identified the presence of carbonate in veins, which amounted to ~6 wt%. Furthermore, photomicrographs collected during Expedition 357 from Micro357 show the presence of olivine neoblasts pseudomorphically replaced by carbonate minerals (Früh-Green et al, 2017).

#### *3.2.1.4 Expedition 304/305 sample Micro304*

IODP Expedition 304/305 targeted the Atlantis Massif at 30°N, to study the processes that determine the formation of oceanic core complexes and the exhumation of ultramafic lithologies to the seafloor. Site 1309 is situated on the central dome of the Atlantic Massif, where the latest and lowest-temperature metamorphic alteration is recorded by white veins infilled by carbonate and sulfide ± chlorite or carbonate associated with saponite. This stage is inferred to occur at low temperature, possibly at 100-120 °C, as recorded at the bottom of Hole 1309D (Blackman et al., 2006b).

The sample analyzed in this study was recovered from serpentized harzburgite recovered from Hole 1309B. Serpentine veins at this hole are commonly associated with fine-grained carbonate, which was also observed replacing ribbon-textured serpentine during IODP Expedition 304/305 (Blackman et al., 2006b). Moreover, calcite and/or aragonite veins were locally recognized. The Micro304 sample was recovered from 58.1 mbsf and is part of an ultramafic unit made of protogranular harzburgite that records the contact with the upper gabbroic units. A mm-wide white zone of talc-tremolite-carbonate alteration is present at the contact between mafic and ultramafic rocks and intrudes into the ultramafic unit along fractures. Micro304 records an intermediate serpentinization degree and contained abundant pyroxene, both as bastite and unreplaced crystals.

### 3.2.2 *Site variability*

The samples included in this study were all recovered from the first 100 mbsf at drilling sites located at slow-spreading segments of the Mid-Atlantic Ridge and having young ages (<2 m.y., Grimes et al., 2008; Cooperdock and Stockli, 2018). All sites show evidence for low-temperature water-rock interactions in the form of secondary mineral precipitates - carbonate and iron oxyhydroxides are the most common occurrences, together with iowaite identified during ODP Leg 209 and saponite recognized during IODP Expedition 304. All sites drilled through shallow and faulted sections of exposed oceanic lithosphere, where the faults could have acted as preferential pathways that facilitated the entrainment of seawater. All samples consist of serpentinized harzburgite, which was the dominant lithology retrieved from most drilling sites with the exception of IODP Expedition 304, which chiefly recovered gabbroic rocks. Micro357 presents some compositional variability as it was affected by silica metasomatism that overprinted serpentinization, producing thick talc veins.

### 3.2.3 *Focused ion beam-scanning electron microscopy*

Focused ion beam scanning electron microscopy (FIB-SEM) analyses were carried out on one thin section sourced from Ocean Drilling Program (ODP) core sample 209-1274-A-3R1 61-71. The data sets were collected with a FEI Helios NanoLab™ G3 DualBeam FIB-SEM at the Electron Microscopy Center at Utrecht University (NL) in backscattered mode and under a high vacuum. Regions of interest were identified at the contact between the serpentine matrix and unreplaced olivine crystals and coated with platinum to prevent beam damage during acquisition. The voxel dimensions in data set FIB-2-209 are 8 nm in the  $x$  and  $y$  directions and 10 nm along  $z$ . To characterize the presence of pores smaller than the voxel size of FIB-2-209, we collected data set

FIB-1-209 next to the FIB-2-209 area. FIB-1-209 has voxel dimensions of 2 nm along  $x$  and  $y$  and 10 nm along  $z$ .

#### *3.2.4 Synchrotron-based microtomography*

Samples Micro209, Micro304, and Micro357 were prepared by grinding on a polishing wheel to obtain cylindric cores with an approximate diameter of 5 mm (~6 mm for Micro209). The samples were scanned with a parallel, monochromatic X-ray beam on the Biomedical Imaging beamline of the Canadian Light Source (BMIT-ID, Wysokinski et al., 2015). The photon energy employed was 35-45 keV and varied depending on the sample thickness to achieve optimal transmission of ~30%. Cubic voxels with dimensions of 1.6  $\mu\text{m}$  were recorded with a PCO Edge 5.5 camera coupled to a 50  $\mu\text{m}$  LuAG:Ce scintillator (Crytur) via an optical system (Optique Peter) with 4x magnification. The distance between the sample and detector was 20 cm and phase retrieval methods (Paganin et al., 2002) were applied to optimize the spatial coherence of the beam. The dynamic camera range was used at approximately 20% and 2000 projections were acquired. Data reconstruction was performed in tofu/ez-ufo software package (Faragó et al., 2022).

#### *3.2.5 Processing, segmentation and quantification of tomographic data*

All image processing and quantification of segmented pores were performed with the ThermoFisher Scientific PerGeos software package, whereas the segmentation steps were carried out with Object Research System (ORS) (Montreal, Quebec Canada) Dragonfly software. The micro-computed X-ray tomography ( $\mu\text{-CT}$ ) data sets required filtering of the raw data to obtain cleaner segmentation of the pore network. The same processing recipe has been employed for every sample to ensure consistency across the various data sets. The processing routine involved the initial application of a non-local means filter to remove image noise from the raw data and

subsequent application of Sobel, Bilateral and Median filters. Finally, the resultant data sets were combined using the following equation:

$$I_{final} = \frac{Bilateral * Sobel}{256} + Median * \left(1 - \frac{Sobel}{256}\right) \quad \text{Eq. 3-1}$$

Where  $I_{final}$  stands for final imaging result. When Eq. 3-1 is applied to 8-bit image data, it results in a grayscale image where voxels located at the edges of objects are identified by the Sobel filter and processed by Bilateral smoothing. Voxels that are not located on the edges of objects are instead smoothed according to the Median filter. The final step of the processing routine involved adjustment of the contrast and brightness of the data sets to facilitate the discrimination between dark areas indicative of pores and gray areas indicative of serpentine minerals. The segmentation of the porous regions was performed using an artificial intelligence algorithm with U-net architecture available in Dragonfly. Details about the training material employed for machine learning can be found in Appendix B.

The presence of intense shading and frequent ring artifacts precluded the quantification of the porosity content across the entire tomographic volume in sample Micro209. Therefore, local sub-volumes devoid of significant artifacts and showing relevant features were segmented individually. Hence, no statistically significant pore size distribution (PSD) could be extracted from sample Micro209. In samples Micro357 and Micro304, it was possible to segment and quantify the pore volume across the entire 3D volume, thus permitting a statistically significant determination of the PSD. The PSD was calculated by quantifying the volume of interconnected pores and assuming that the pore volume equates to a sphere whose diameter is the equivalent spherical diameter. To account for segmentation artifacts related to random noise in the background images, pores that contained less than nine voxels were excluded from computations in each data set. To interpret the

distribution of the pore networks, pores with volumes smaller than 125 voxels have been removed from the visualizations. The Euler characteristic  $\chi$  was calculated for each pore after an automatic separation step in PerGeos. The Euler characteristic is an indicator of the degree of connectivity of a structure, and negative values of  $\chi$  indicate a higher degree of connectivity (Vogel et al., 2010). Further details about the calculation of  $\chi$  values can be found in Appendix B.

### 3.3 Results

The textural distribution of analyzed pores and mineral phases for each sample shows characteristics typical of altered peridotites. FIB-SEM images and grain-scale observations demonstrate the incipient generation and growth of the pore network in the form of dissolution channels that affect olivine remnants (Fig. 3 - 2).

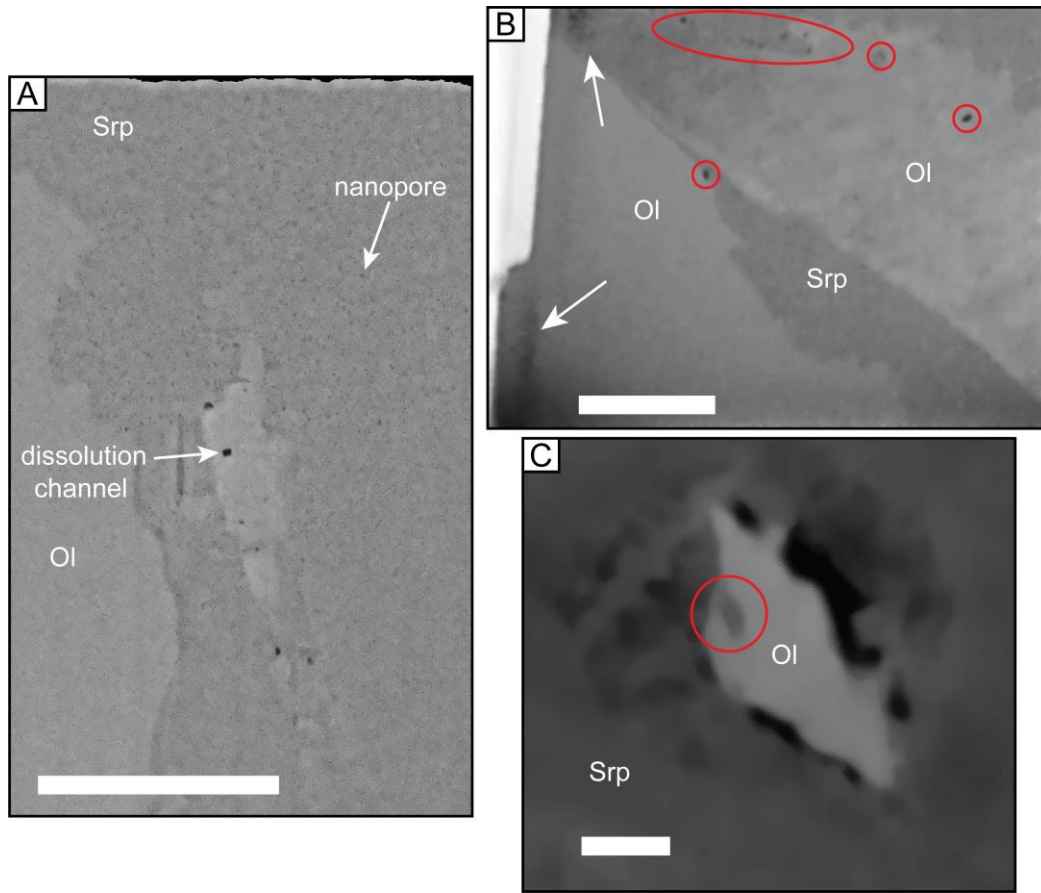


Fig. 3 - 2. Orthoslices presenting the results of FIB-SEM analyses and grain-scale observations. (a) FIB-SEM image, data set FIB-1-209. Nanometric pores are recognized in the serpentine matrix as small dark spots. Coarser dark spots found in contact with olivine are dissolution channels. Scale bar = 1  $\mu$ m. (b) FIB-SEM image, data set FIB-2-209. White arrows point to shading artifacts that were excluded from the quantification of porosity. Red circles highlight the presence of pores. Scale bar = 1  $\mu$ m. (c)  $\mu$ -CT image, sample Micro209. Pores partially rim the grain boundary of olivine. An etch pit is highlighted with a red circle. Scale bar = 50  $\mu$ m. Ol = olivine; Srp = serpentine.

At the micron-scale,  $\mu$ -CT data illustrate that pores form clusters with a spatial distribution that is controlled by the presence of olivine remnants (Fig. 3 - 3). A summary of the abbreviated names used to refer to the analyzed samples and references to their full names can be found in Table 3 - 1.

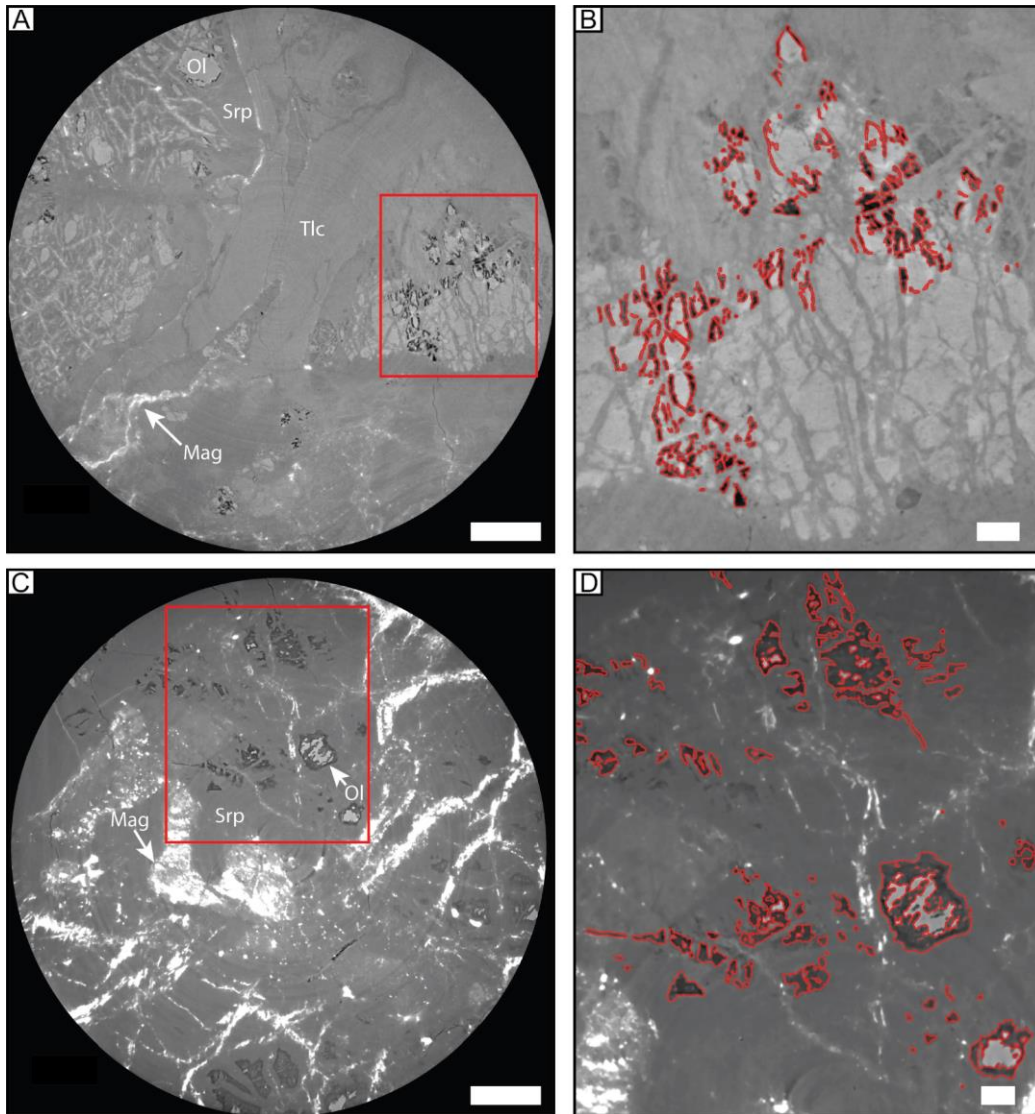


Fig. 3 - 3. Orthoslices depicting the results of core-scale observations from  $\mu$ -CT data sets. (a) Sample Micro357, showing an association of olivine, serpentine, talc and magnetite. The red rectangle highlights an area rich in pores. Scale bar = 500  $\mu$ m. (b) Close-up of the area outlined with a red rectangle in Fig. 3 - 2a. Pores outlined with red markings partly envelop olivine grains. Scale bar = 100  $\mu$ m. (c) Sample Micro304. Bright magnetite in veins and pseudomorphous bastite (center-left of the image) in a serpentine matrix with sparse olivine crystals. (d) Close-up of the area highlighted with a red rectangle in Fig. 3 - 2c. The pores have been outlined with red markings. Scale bar = 100  $\mu$ m. Ol = olivine; Mag = magnetite; Srp = serpentine; Tlc = talc.

### 3.3.1 FIB-1-209

FIB-SEM analyses of FIB-1-209 (Fig. 3 - 2a) represent the highest resolution imagery presented here and thus record the distribution of the finest pore sizes. In this data set, a broad crystal and

isolated, smaller ( $\sim 1 \mu\text{m}$  along its longest dimension) grains of olivine are surrounded by a darker gray serpentine matrix. Two distinct size classes of pores are present: 1) nanometer-sized pores (with diameter  $< 30 \text{ nm}$ ), which are scattered through the serpentine matrix (visible as isolated dark dots); 2) coarser pores (diameters  $> \sim 30 \text{ nm}$ ), which are located either at the grain boundary of the central olivine grain or within the unreplaced crystal, close to the grain boundary. The 3D reconstruction of FIB-1-209 (Fig. 3 - 4a) shows that both classes of pores form channels that are subparallel and elongated along the  $z$ -direction of the tomographic volume.

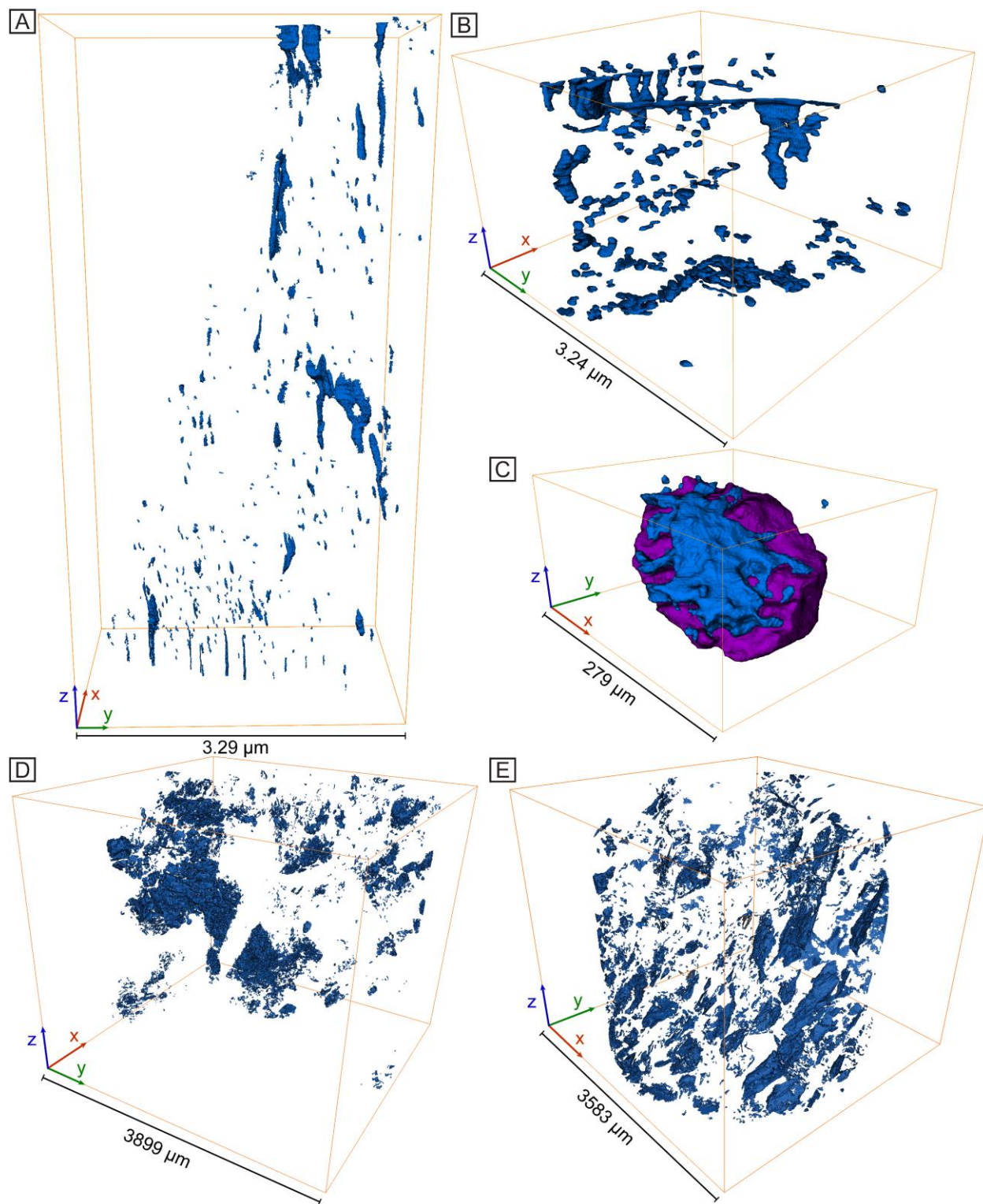


Fig. 3 - 4. Tomographic volumes reconstructed from FIB-SEM and  $\mu$ -CT data sets. Pores smaller than 125 voxels have been hidden to ease the visualization of the main pore structures. (a) Data set FIB-1-209. Dimensions:  $x = 1.91 \mu\text{m}$ ,  $y = 3.29 \mu\text{m}$ ,  $z = 6.66 \mu\text{m}$ . (b) Data set FIB-2-209. Dimensions:  $x = 2.98 \mu\text{m}$ ,  $y$

= 3.24  $\mu\text{m}$ , z = 2.09  $\mu\text{m}$ . (c) Sample Micro209,  $\mu\text{-CT}$  data set. Purple = olivine; blue = pores. Dimensions: x = 279  $\mu\text{m}$ , y = 256  $\mu\text{m}$ , z = 139  $\mu\text{m}$ . (d) Sample Micro357. Dimensions: x = 3899  $\mu\text{m}$ , y = 3899  $\mu\text{m}$ , z = 3454  $\mu\text{m}$ . (e) Sample Micro304. Dimensions: x = 3583  $\mu\text{m}$ , y = 3583  $\mu\text{m}$ , z = 3023  $\mu\text{m}$ .

The coarse channels have dimensions < 200 nm (Fig. 3 - 5a) and have relatively smooth surfaces and conical shapes (e.g., Fig. 3 - 4a, top). They do not exhibit branching or significant lateral connectivity, as is confirmed by the observation that all calculated values of the Euler characteristic,  $\chi$ , for this sample are  $\geq -2$  (Fig. 3 - 6a), which represents the least negative  $\chi$  distribution (i.e., least connected) we report (Fig. 3 - 6).

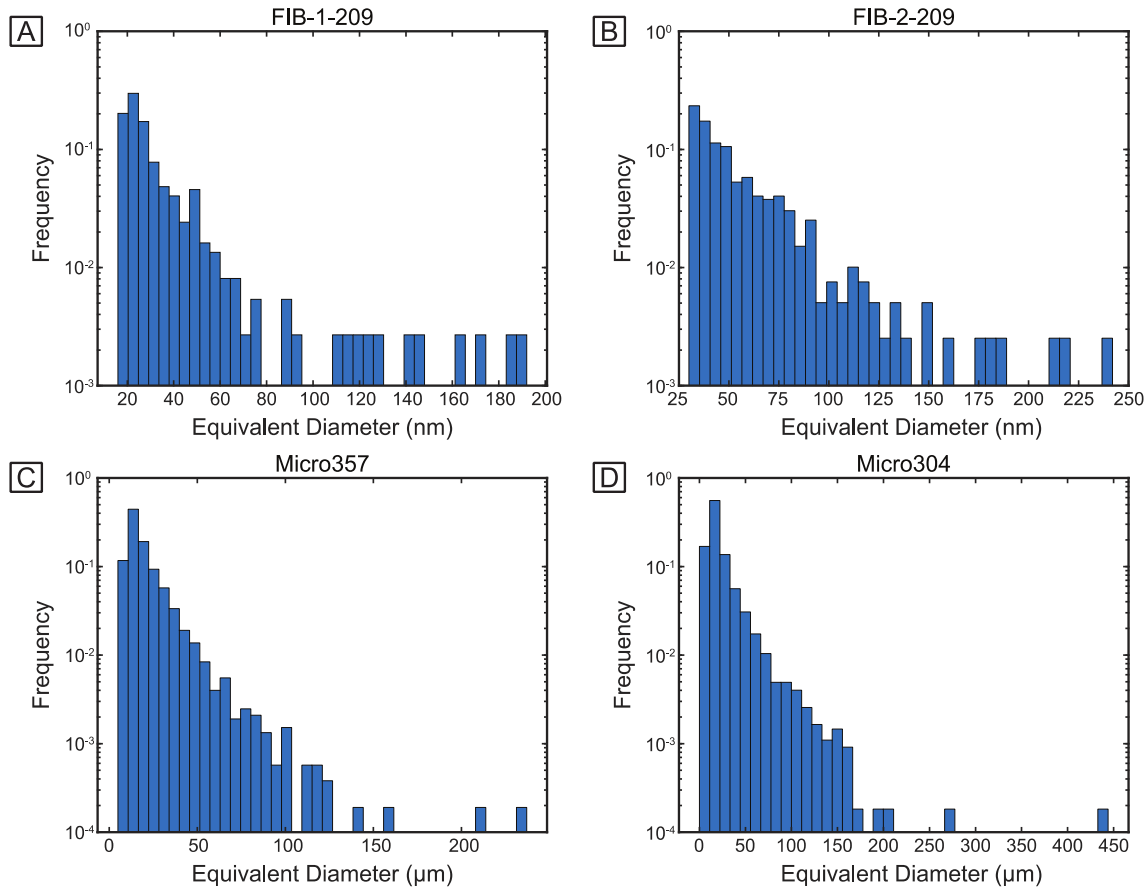


Fig. 3 - 5. Pore size distribution (PSD) of statistically significant quantifications of pore size distributions. Number of bins = 40. (a) PSD of sample 209-1274-A-3R1 61-71 data set FIB-1-209, n = 398. (b) PSD of sample 209-1274-A-3R1 61-71, data set FIB-2-209, n = 397. (c) PSD of sample Micro357, n = 5253. (d) PSD of sample Micro304, n = 5474.

### 3.3.2 FIB-2-209

FIB-SEM analyses of sample FIB-2-209 permitted to record pore structure with minimum sizes of 8 nm along the  $x$  and  $y$  directions and 10 nm along the  $z$  direction, thus having similar, but slightly coarser size than those of FIB-1-209 (Table 3 - 1). Similar to FIB-1-209, FIB-2-209 contains domains of olivine surrounded by a darker gray serpentine matrix. However, due to the lower resolution of data set FIB-2-209 compared to FIB-1-209, it is possible that the nanometer-sized pores were present also in data set FIB-2-209 but were less completely imaged (Fig. 3 - 2). Therefore, the population of pores identified from data set FIB-2-209 broadly corresponds to the coarser porosity observed in data set FIB-1-209. Pores in FIB-2-209 primarily occur at the grain boundary of unreplaced olivine grains (red circles in Fig. 3 - 2b). 3D visualization of the FIB-2-209 tomographic volume shows the presence of vertically elongated, channel-shaped pores that stretch along the grain boundaries of unreplaced olivine (e.g., Fig. 3 - 4b, top). The individual and separated pore channels initially observed in sample FIB-1-209 appear more evolved in FIB-2-209, with an increased degree of lateral connectivity indicative of pore coalescence as they evolve from linear towards more planar features. The increased degree of connectivity is reflected by more negative values of  $\chi$ , down to -5, indicating that the coarser pore structures in FIB-2-209 are more than twice as connected as in FIB-1-209 (Figs. 3 - 6a and 3 - 6b). Overall, data sets FIB-1-209 and FIB-2-209 show comparable pore size distributions and connectivity values, with the difference that FIB-1-209 also captured isolated and nanometer-sized pores present in the serpentine matrix, which could not be detected in FIB-2-209 due to its lower spatial resolution.

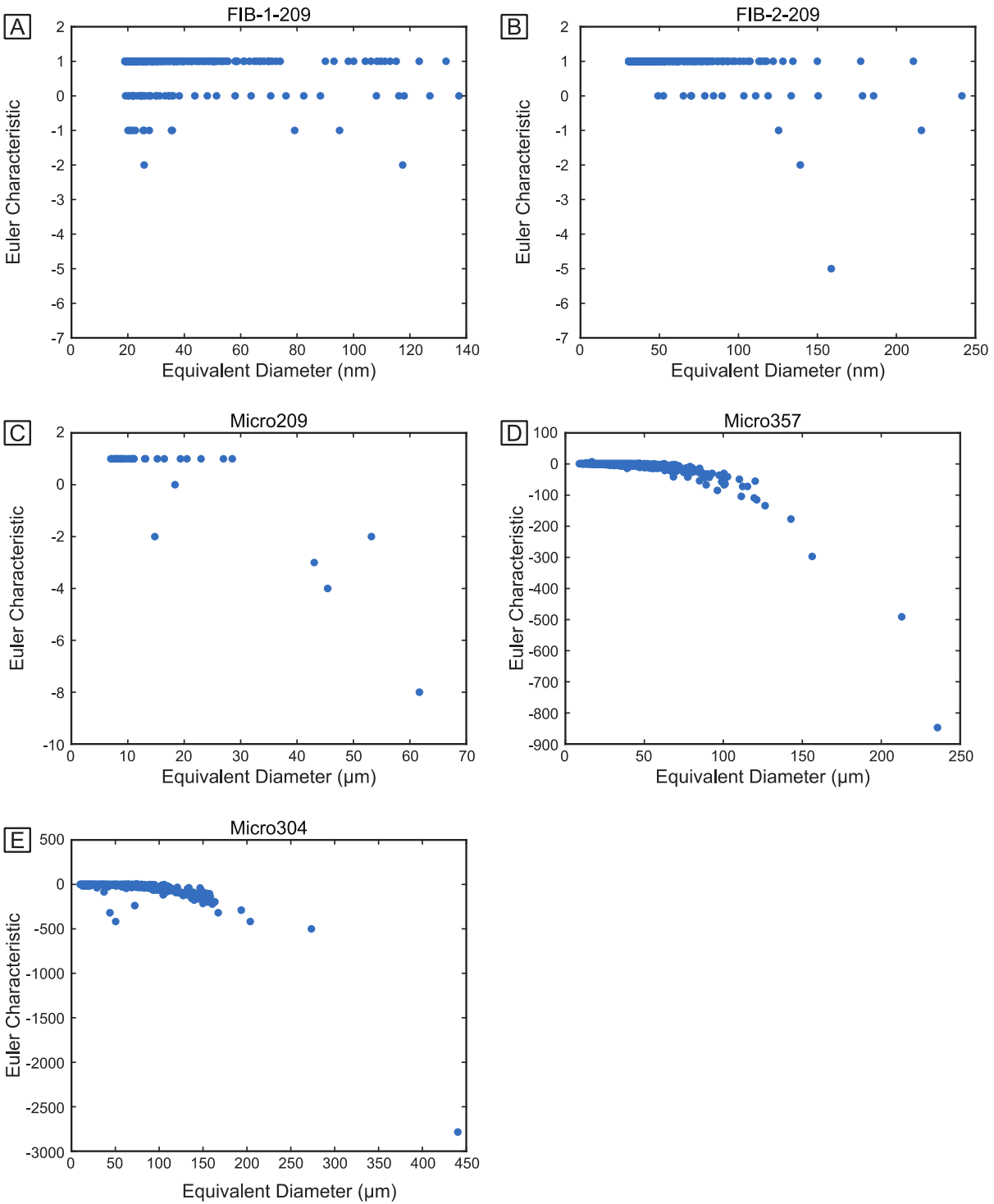


Fig. 3 - 6. Plots of Euler characteristic values as a function of the equivalent spheric diameter. More negative values of the Euler characteristic ( $\chi$ ) represent increased degree of connectivity. (a) Sample 209-1274-A-3R1 61-71 data set FIB-1-209,  $n = 398$ . Minimum  $\chi = -2$ . (b) Sample 209-1274-A-3R1 61-71, data set FIB-

2-209, n = 397. Minimum  $\chi = -5$ . (c) Sample Micro209, n = 36. Minimum  $\chi = -8$ . (d) Sample Micro357, n = 5253. Minimum  $\chi = -847$ . (e) Sample Micro304, n = 5474. Minimum  $\chi = -2785$ .

### 3.3.3 *Micro209*

Processed sub-volumes from sample Micro209 contain olivine surrounded by serpentine, with porous areas located along the olivine-serpentine grain boundaries (Fig. 3 - 2c), similar to the texture identified in the previous two samples. However, in sample Micro209, the observed pores exist at a significantly larger (micrometric) scale, and their structure has evolved towards more planar morphologies – i.e., individual pores do not have circular outlines but develop laterally along the olivine-serpentine grain boundaries. Additionally, etch pits can be observed impinging into unreplaced olivine (e.g., Fig. 3 - 2c, red circle). In 3D, the pore structure envelopes the relict olivine, in direct contrast to the channeled pores observed at smaller scales in FIB-1-209 and FIB-2-209 (Figs. 3 - 2a and 3 - 2b, respectively). The lateral expansion appears to occur via the development of individual porosity channels that expand radially from the central pore mass. Figure 3 - 6c shows that the most negative value of  $\chi = -8$  indicates that pores in sample Micro209 are marginally more connected than those in FIB-2-209 ( $\chi = -5$ ).

### 3.3.4 *Micro357*

The altered peridotite imaged in sample Micro357 is characterized by a central, conspicuous serpentine vein overprinted in its center by talc. The other primary textural domain is made of remnants of olivine that range in size from  $\sim 20 \mu\text{m}$  to  $\sim 200 \mu\text{m}$ . They have been partly to fully replaced by serpentine and magnetite, forming a mesh texture (Fig. 3 - 3a, left side) where thin magnetite veinlets are aligned along the mesh rims. Olivine is also present in clusters devoid of oxides and dissected by serpentine veinlets (Fig. 3 - 3a, red rectangle). Similar to sample Micro209, pores are localized at olivine grain boundaries in both textures present in Micro357, and  $\sim 6 \mu\text{m}$  to

~20  $\mu\text{m}$  thick pore structures envelop olivine remnants. The pores are best developed within the dissected olivine structure (e.g., Fig. 3 - 3a, red rectangle).

Nevertheless, not every olivine remnant is surrounded by pores, likely due to the distribution of local fluid pathways. 3D visualization demonstrates that the pores are organized in clusters - the central vein separates the two major pore clusters in Micro357 (Fig. 3 - 4d) imaged in this sample (Fig. 3 - 3a). The channel-shaped pores observed in the FIB-SEM data sets (Figs. 3 - 4a and 3-4b) cannot be identified in Micro357; at the scale of  $\mu\text{-CT}$  analyses only coarser and more developed pore structure can be detected, which are recognized around unreplaced olivine remnants and more frequently encountered within the domains of dissected olivine. The PSD suggests coalescence of pores coinciding with the creation of a coarser pore network (Fig. 3 - 5c). Within this coarser pore network, more lateral connections between individual pores have formed, achieving higher calculated connectivity than all the samples described thus far (FIB-1-209, FIB-2-209, and Micro209). The two coarser connected pore volumes identified for Micro357 have  $\chi$  of -491 and -847 (Fig. 3 - 6d), indicating a degree of connectivity that is two orders of magnitude greater than the previous samples.

### 3.3.5 *Micro304*

In sample Micro304, bright oxide minerals and scattered olivine grains are surrounded by a serpentine matrix that dominates the sample volumetrically (Fig. 3 - 3c). The oxides are organized in veins and secondary veinlets (Fig. 3 - 3c bottom left and top right) or in clusters associated with serpentine that pseudomorphically replace pyroxene (i.e., bastite, Fig. 3 - 3c center and top left). Olivine is present as isolated grains (Fig. 3 - 3c red rectangle) or small clusters made of several grains (Fig. 3 - 3c bottom). Olivine remnants show irregular morphologies that result from the presence of pores along their grain boundaries. In Micro304 porosity affects the rock so

extensively that some grains of olivine have been completely removed, leaving behind voids that mimic the morphology of olivine fragments (Fig. 3 - 3d). Moreover, elongated etch pits can be seen protruding within domains of remnant olivine (Fig. 3 - 3d). Pores rimming olivine and etch pits observed in Micro304 are the most developed compared to all studied samples, with pore size ranging from  $\sim 6 \mu\text{m}$  to  $\sim 50 \mu\text{m}$ .

The 3D pore network in Micro304 shows the presence of several coarse pore clusters that are preferentially oriented and slightly inclined compared to the vertical direction of the tomographic volume (Fig. 3 - 4e). Because the porosity is well developed, it affects the coarser grains of olivine. As a result, it forms large pore clusters more frequently than in Micro357, in which pores were primarily found around fine-grained olivine remnants. This aspect is reflected in the pore size distribution of Micro304, which shows both the presence of 2 large pores with sizes greater than  $250 \mu\text{m}$ , and a higher abundance of pores ranging from  $50 \mu\text{m}$  to  $200 \mu\text{m}$  than Micro357 (Fig. 3 - 5d). However, the overall textural style in Micro357 and Micro304 appears similar, with pores located at the grain boundaries of olivine and enveloping its remnants. The preservation of the morphology inherited by olivine fragments can also be recognized in 3D, where the larger pores preserve prismatic shapes (Fig. 3 - 4e, most easily identified at the bottom-right side). Lateral coalescence of the pores in Micro304 is the most developed of all samples analyzed, and results in pores forming an almost continuous envelope around olivine crystals. This textural style leads to the formation of large pores, with the size of the individual pores depending on the grain size of primary olivine crystals, achieving in Micro304 a maximum equivalent diameter of  $\sim 440 \mu\text{m}$  (Fig. 3 - 5d). Coarser pore sizes are accompanied by an enhanced degree of connectivity, evidenced by the recorded minimum  $\chi$  value of  $-2785$  (Fig. 3 - 6e).

## 3.4 Discussion

In this section, we describe the preferential orientation of pores observed in our FIB-SEM data sets and in Micro304 (Section 3.4.1), examine the potential of serpentinization processes to explain the genesis of the pore structures identified in the analyzed samples (Section 3.4.2), consider the spatial association of the samples to alteration features identified in the core sections from which the samples were sourced, and interpret the pore structures in a kinetic framework (Section 3.4.3). Finally, we explore the implications of our findings for interpreting the role of low-temperature peridotite weathering in ocean geochemistry and the coupled silicate-carbonate cycle (Section 3.4.4).

### *3.4.1 Anisotropic distribution of pores*

Most segmented pores in the FIB-SEM data sets (Fig. 3 - 4a and 3 - 4b) are subparallel and display a preferential orientation, particularly evident in the dissolution channels. Several studies describing the anisotropic dissolution of olivine crystals have shown that the dissolution rate of olivine is fastest along its crystallographic b-axis (Grandstaff, 1978; Awad et al., 2000; King et al., 2014; Peuble et al., 2015). Anisotropic dissolution has been suggested to arise from the preferential orientation of M(1) crystallographic sites in olivine parallel to [010]. M(1)-oxygen bonds attain a more negative charge than M(2)-oxygen bonds, leading to more favorable protonation of oxygen bond to the M(1) sites (Awad et al., 2000). Alternatively, the elongated shape of the pore channels could result from preferential dissolution along olivine subgrain walls; however, their presence could not be assessed with the analytical approach employed in this study. At the micrometer-scale, preferential orientation of the coarser pores was recognized in Micro304 (Fig. 3 - 4e). Because the pores in Micro304 form envelopes around olivine grains, the observed preferential pore orientation may result from the anisotropic distribution of primary olivine crystals.

Crystallographic preferred orientations (CPOs) similar to the preferential orientations recognized in this study have been identified elsewhere and attributed to the action of the asthenospheric mantle flow, that via plastic deformation leads to subgrain wall formation with statistically non-random distribution and consequent alignment of subgrain walls creating a CPO, with the (010) planes orienting subparallel to the direction of the mantle flow (Peuble et al., 2015). The pores observed in this study are located at the grain boundaries of olivine, consequently the preferential orientation of the olivine grains is likely to control the spatial distribution of the pores.

#### *3.4.2 Serpentinization-generated nanopores*

Serpentinization is the main style of hydrothermal alteration in samples investigated here, and also the most commonly identified alteration style in peridotite cores drilled from the oceanic crust, thus we explore its potential to explain the observed pore textures. Notably, all of our tomographic data sets are characterized by an absence of secondary phases filling the pores located at olivine grain boundaries. Thus, any geochemical process capable of explaining the textures reported here must be consistent with the lack of in situ precipitation of secondary products.

Serpentinization reactions are commonly understood in terms of an interface-coupled dissolution-precipitation mechanism (ICDP, Plümper et al., 2012), which involves the formation of secondary phases in a thin fluid film located at the interface with reacting primary minerals. Local precipitation of alteration phases is central to the ICDP mechanism, because it leads to the local buildup of differential stresses due to the increase in solid volume when primary phases are converted to secondary minerals, ultimately leading to fracturing of the rock that generates new pores. However, because the pore morphologies we observe (Fig. 3 - 4) are not planar, they could not have formed due to fracturing. Nevertheless, neutron scattering studies (Tutolo et al., 2016) suggest that the formation of new pores accompanies serpentinization reactions. The newly

generated pores are expected to be nanometer-sized (Tutolo et al., 2016), and thus likely correspond to the nanopores identified within the serpentine matrix only in our highest-resolution data set FIB-1-209 (Fig. 3 - 2a). These pores were noticed only in the serpentine matrix and are not associated with other mineral phases. Moreover, due to the low reactivity of serpentine in seawater-derived fluids at low temperatures (Luce et al., 1972; Bales and Morgan, 1985), we conclude that this specific, nanometer-sized grouping of pores formed during serpentinization reactions. The pore structure shown by natural and experimentally serpentinized olivine crystals typically consists of funnel-shaped etch pits that evolve to networks of polyhedral and pyramidal mounts that impart an indented morphology to the altered olivine grains, and generally are distributed homogeneously across crystal faces (Lafay et al., 2012). The pore structures that affect olivine grains observed in our FIB-SEM data sets are strikingly different, showing sparse pores with high aspect ratio that penetrate deeply into olivine fragments, forming elongated dissolution channels. Due to the lack of textural similarities between the planar fractures or funnel-shaped etch pits expected to form due to serpentinization reactions (Plümper et al., 2012) and the elongated dissolution channels shown in this study, we conclude that the pores associated with olivine dissolution formed by some process other than serpentinization (Velbel, 2009).

#### *3.4.3 Porosity generation during seafloor weathering*

The samples analyzed here were all recovered from drilling sites that showed extensive evidence of seawater-driven low-temperature alteration (e.g., carbonate veins, oxidative haloes, and, in Leg 209 rocks, iowaite and nontronite mineralization, Appendix B). Most samples were in close proximity to carbonate precipitates (Section 3.1.1, Appendix B), suggestive of seawater infiltration (Bach et al., 2011) except for Micro209, which was close to several interpreted faults that likely acted as pathways for focused fluid flow in the subseafloor (Bach et al., 2004; Section 3.2.1.2;

Appendix B). Open-system conditions consistent with these observations would result in open pore space that lacks in situ precipitate by preventing attainment of the extreme levels of supersaturation required to precipitate secondary Mg-silicates (Arizaleta et al., 2020; Che et al., 2021; Mulders and Oelkers, 2021; Tosca, 2015) and carbonates (Berninger et al., 2014; Power et al., 2017) at low temperatures (i.e., < 100 °C, Snow and Dick, 1995; Bach and Früh-Green, 2010) by exporting Mg and Si in reaction fluids, away from the reaction interface. Because olivine dissolution is very rapid at the aforementioned conditions (log rate =  $\sim -10$  mol/m<sup>2</sup>/s at pH = 8 and T = 25 °C, Oelkers et al. 2018), secondary phase precipitation becomes the rate-limiting step (Tutolo et al., 2018) and net Mg and Si export in the fluid phase can thus be achieved. In this scenario, secondary minerals will be precipitated at a hydrologically-controlled distance from the location of olivine dissolution (e.g., stagnation points where fluids experience longer residence time), if at all. Recent experiments examining olivine dissolution in seawater at ambient temperatures support this observation – although CaCO<sub>3</sub> can readily precipitate during early stages of seawater-olivine interaction, Mg-carbonates do not, and Mg-silicates precipitate sluggishly (Fuhr et al., 2022). Together, these observations suggest that the pore textures examined here formed due to the interaction between seawater and harzburgites at temperatures close to ambient conditions (< 100 °C, Snow and Dick, 1995, Bach and Früh-Green, 2010), a process commonly referred to as seafloor weathering. Open-system conditions required by seafloor weathering reactions would result in a highly interconnected pore network that enables the percolation of seawater through the serpentinite. The largest and most representative tomographic volumes presented in this study (Micro357 and Micro304) show the lowest (i.e., most interconnected) Euler characteristic values (Fig. 3 - 6). The reported connectivity values represent minima, because the voxel dimensions of our  $\mu$ -CT data sets (1.6  $\mu$ m) cannot capture the nanometer-scale pore

structures detected with the FIB-SEM analyses (Fig. 3 - 2a, 3 - 2b, 3 - 4a, 3 - 4b). The latter are expected to act as pore throats that would further increase the interconnectivity of the pore structure. Whereas Euler characteristic values cannot be used to determine a quantitative threshold between open- and closed-system conditions, in samples Micro357 and Micro304 they define a highly interconnected network that, in concert with the previously outlined kinetic reasoning, suggests infiltration of weathering fluids that percolated through (and reacted with) the grain boundaries of olivine.

#### *3.4.4 Elemental fluxes and implications*

Low-temperature seafloor weathering processes result in elemental fluxes that increase seawater alkalinity and impose significant controls on the atmospheric concentration of CO<sub>2</sub> (Brady and Gislason, 1997; Coogan and Gillis, 2018), exerting a negative feedback that removes carbon from the atmosphere at rates on par with continental weathering (Coogan and Gillis, 2013). Significant magnitudes of atmospheric CO<sub>2</sub> drawdown require comparable magnitudes of chemical fluxes between the oceanic crust and seawater. Snow and Dick (1995) initially suggested loss of Mg during low-temperature weathering of peridotite due to its interaction with seawater, which dramatically impacts the global Mg budget of the ocean. The removal of brucite from the mineralogic assemblage in altered peridotite (Beinlich et al., 2018) cannot explain the mass balance required to justify the degree of Mg loss (Snow and Dick, 1995, Klein et al., 2020) – i.e., olivine dissolution is required, and is exemplified by the textures reported in this study. Evidence of Mg exports comes from isotopic studies on altered oceanic crust (Huang et al., 2018), which revealed that the equivalent of ~12% of the continental riverine input of Mg is extracted from the oceanic crust during low-temperature alteration. Several studies observed elemental mobility during alteration of peridotite both in experimental and natural seafloor settings (Snow and Dick,

1995; Lacinska et al., 2017). Moreover, recent studies on ophiolitic samples from Oman (de Obeso and Kelemen, 2020; de Obeso et al., 2021) reveal that Mg can be mobilized during alteration, as evidenced by the presence of meter-wide magnesite veins, and a loss of up to 30% of the original Mg content in the most altered rocks.

Table 3 - 2. Estimation of the yearly Mg flux extracted during weathering of serpentinized peridotite according to the weathered fraction ( $\Phi$ ) quantified in this study.

Data		Results	
Ridge length (km)	14660 <sup>a</sup>	Area created (m <sup>2</sup> /yr)	167124
Exhumation rate (mm/yr)	11.4 <sup>a</sup>	Weathered volume (m <sup>3</sup> /yr)	2.84*10 <sup>8</sup>
Peridotite density (kg/m <sup>3</sup> )	3300	Removed fraction (porosity) m <sup>3</sup>	1.26*10 <sup>6</sup>
Molar mass Forsterite (kg/mol)	0.140691 <sup>b</sup>	Dissolved mass (kg/yr)	4.17*10 <sup>9</sup>
Weathering depth (m)	1700 <sup>c</sup>	Dissolved olivine (mol/yr)	2.97*10 <sup>10</sup>
Weathered fraction ( $\Phi$ )	0.00445 <sup>d</sup>	Mg flux (mol/yr)	1.48*10 <sup>10</sup>
Riverine Mg input (mol/yr)	5.5*10 <sup>12</sup> <sup>e</sup>	Fraction of riverine input (%)	0.27

<sup>a</sup>After Cannat et al. (2010). The ridge length is calculated as the proportion of global length of slow-spreading ridges that exhume new ultramafic crust. Due to the asymmetric exhumation that occurs along detachment faults at slow-spreading ridges, the exhumation rate is assumed to be equal to the average half-spreading rate at slow-spreading ridges.

<sup>b</sup>Molar mass calculated for pure forsterite endmember Mg<sub>2</sub>SiO<sub>4</sub>.

<sup>c</sup>Depth estimated by considering a maximum weathering temperature of 100 °C with a geothermal gradient of 60 °C/km.

<sup>d</sup>Calculated as the average total porosity quantified from tomographic data in samples Micro357 and Micro 304.

<sup>e</sup>After Elderfield and Schultz (1996); Berner and Berner (1987).

Dissolution of olivine during seafloor weathering of peridotite generates Si-enriched pore fluids that can contribute to the reservoir of biogenic silica used by silicifying organisms like radiolaria, sponges, and diatoms (Tréguer et al., 2021). Alternatively, dissolved Si and Mg can accumulate in pore fluids at stagnation points within the rock's pore network, becoming supersaturated with respect to secondary Mg-phyllsilicates that consequently precipitate from solution in a process known as reverse weathering (Tréguer et al., 2021). The absence of secondary Mg-phyllsilicates

in our samples is likely attributable to the fine size of the observed pore structures, which is capable of suppressing the nucleation of secondary minerals (Putnis and Mauthe, 2001). In Table 3 - 2 we report an approximate estimation of the yearly flux of Mg removed from serpentinites due to dissolution of olivine based on the average pore volume quantified in samples Micro357 and Micro304. We obtain a yearly Mg flux of approximately 14.8 Gmol, which is one order of magnitude lower than the intermediate estimate calculated in Snow and Dick (1995), and corresponds to less than 1% of the yearly riverine input of Mg in seawater. Because samples Micro357 and Micro304 are relatively young (<2 m.y. old, Blackman et al., 2006b), we can expect that export of Mg will continue in off-axis environments until (i) all remnants of olivine dissolve, or (ii) oceanic crustal rocks experience significant reduction in permeability that isolates them from seawater circulation, which is predicted to occur for crustal ages older than ~65 m.y. (Coogan and Gillis, 2018). In fact, the tomographic data for Micro357 and Micro304 show the presence of remnants of olivine (Fig. 3 - 3), which occupy 7.01 % and 4.13 % of the tomographic volumes, respectively, and averaging at 5.57%. Following the calculation scheme summarized in Table 3 - 2, if we assume complete dissolution of the average volume of olivine remnants found in Micro357 and Micro304 and add this volume fraction (0.0557) to the weathered fraction based on the quantified pore volume (0.00445), we estimate a maximum yearly flux of 200 Gmol of Mg to seawater during low-temperature weathering of serpentinitized peridotite.

### 3.5 Conclusions

In this study, we have reported the result of image processing of tomographic volumes acquired on serpentinitized harzburgites recovered by drilling from the oceanic crust. Pore structures and their degree of connectivity have been characterized at the nanometer scale, at the scale of a single olivine crystal, and across the whole pore network at the micrometer scale. The presence of

dissolution pores at the grain boundaries of olivine, the absence of secondary products in situ, and the preservation of serpentine minerals are consistent across all analyzed data sets. Our highest-resolution data sets revealed the presence of nanometric pores in the serpentine matrix, which we suggest formed due to serpentinization processes. We have also observed the presence of elongated dissolution channels, and recorded examples of lateral coalescence of these pore channels. The pores are preferentially oriented, likely due to a crystallographic preferred orientation inherited from olivine crystals. Observations on data sets Micro357 and Micro304 show that pores are found in clusters whose distribution in the rocks depends on the textural expression of olivine remnants (dissected olivine or isolated grains). When the dissolution pores are well developed, they form almost continuous envelopes around the remnants of olivine grains. Serpentinization is unlikely to have generated these observed pores, because they lack in situ secondary product that defines serpentinization. Rather, arguments based on kinetically controlled dissolution and precipitation rates indicate open-system conditions and rapid olivine dissolution rates, coupled to sluggish Mg-silicate and Mg-carbonate precipitation rates, which ultimately created the observed dissolution structures. In this way, the generation of pores during seafloor weathering of ultramafic rocks increases the permeability of the shallow oceanic lithosphere, maintains continued infiltration of seawater in the subsurface, and contributes to the global marine Si and Mg budgets.

**Acknowledgments.** This research used samples and data provided by the International Ocean Discovery Program (IODP). We acknowledge the support of the Natural Sciences and Engineering Research Council of Canada (NSERC) for providing funding for this research under Discovery Grant RGPIN-2018-03800. O. Plümper was supported by a European Research Council Starting grant (nanoEARTH; 852069). This study could not have been possible without the fellowship

granted to S. Pujatti by Interridge in 2018. Part of the research described in this paper was performed at the Canadian Light Source, a national research facility of the University of Saskatchewan, which is supported by the Canada Foundation for Innovation (CFI), NSERC, the National Research Council (NRC), the Canadian Institutes of Health Research (CIHR), the Government of Saskatchewan, and the University of Saskatchewan. We would like to thank Dr. Sergey Gasilov for operating the high-energy Biomedical Imaging beamline of the Canadian Light Source (BMIT-ID) and for his help and commitment to providing high-quality tomographic reconstructions. Finally, we would like to thank two anonymous reviewers for their critical comments which helped to improve this paper's impact and clarity.

## **4 Chapter 4 Fe oxidation and porosity generation in serpentized abyssal peridotite**

### **Abstract**

Serpentinization, the water-driven alteration of olivine-rich rocks, is a fundamental process contributing to planetary habitability and the maintenance of rock-based life on Earth. Serpentinization generates molecular hydrogen via the reduction of water and the coupled oxidation of Fe, which partitions into serpentine, brucite and magnetite. Magnetite formation controls the magnetic properties of serpentinites, and researchers have highlighted a link between increasing magnetic susceptibility and decreasing density of peridotites with increasing degree of serpentinization. Several analytical and theoretical studies have suggested that these increases in magnetization and decreases in density are accompanied by increasing porosity. Here, we investigate the potential correlation between porosity generation and serpentinization by analyzing the geochemical composition, Fe redox state, and porosity of 28 abyssal serpentinites recovered via drilling from the Atlantic Ocean seafloor. Principal component analysis applied to the resulting dataset revealed no direct links between these properties, which we suggest results from the introduction of variability due to low-temperature seafloor weathering processes. Seafloor weathering can modify the porosity of serpentinites by dissolving brucite, and it affects the Fe budget of serpentinites by inducing the replacement of magnetite by Fe(III) minerals like maghemite, hematite and goethite. Moreover, we also suggest that ophiolitic serpentinites would not show direct correlations between porosity and Fe redox content, due to geochemical transformations induced by metamorphism and porosity reworking linked to deformation induced by tectonic stresses.

## 4.1 Introduction

Serpentinization is a mineral hydration reaction that is common on Earth and other celestial bodies (Holm et al., 2015; McCollom et al., 2022); it occurs when ultramafic lithologies interact with water at low to intermediate temperature ( $< 400$  °C, Klein et al., 2014). During serpentinization, primary olivine and pyroxene are altered to form secondary assemblages chiefly composed of serpentine, magnetite and brucite (Moody, 1976), with attendant production of  $H_2$  (Klein et al., 2014; McCollom & Bach, 2009, McCollom et al., 2016b). The introduction of  $CO_2$  into serpentinization environments can lead to reactions with  $H_2$  and the formation of abiotic methane and other reduced hydrocarbon compounds (Cannat et al., 2010; McCollom et al., 2016a). Both  $H_2$  and  $CH_4$  can supply energy to chemosynthetic microorganisms (Russell, 2007; Russell et al., 2010; Schrenk et al., 2013) that exploit metabolic pathways that have been hypothesized to be consistent with the earliest organisms (Okland et al., 2012; Preiner et al., 2018; Russell et al., 2010; Schrenk et al., 2013) on Earth and other rocky bodies (Holm et al., 2015; Guillot and Hattori, 2013; Müntener, 2010; Schulte et al., 2006).

Serpentinization reactions produce  $H_2$  by the reduction of water and coupled oxidation of reduced Fe and its partitioning into secondary serpentine, magnetite, and brucite (Evans, 2008; Klein et al., 2009; Mayhew & Ellison, 2020; McCollom et al., 2016b, 2020). The transfer of Fe from primary paramagnetic minerals like olivine and pyroxene to ferrimagnetic magnetite is the main source of the magnetic properties of serpentinized rocks, which are characterized by increasing magnetic susceptibility with increasing degree of serpentinization (Bina & Henry, 1990; Maffione et al., 2014; Oufi et al., 2002; Saad, 1969; Toft et al., 1990). The extent of serpentinization is also proportional to decreasing rock density, which results from volumetric expansion (Klein and Le Roux, 2020) as primary minerals, e.g., forsterite with a molar volume of  $43.79 \text{ cm}^3/\text{mol}$ , react to

form serpentine, with a molar volume of  $108.5 \text{ cm}^3/\text{mol}$  (Macdonald & Fyfe, 1985), and via porosity generation. In fact, a quantitative justification of the magnetic behavior of serpentinized peridotites requires generation of porosity with increasing serpentinization degree (Toft et al., 1990).

Several studies have revealed trends of increasing porosity with increasing serpentinization degrees, thus requiring generation of pores (Saad, 1969; Toft et al. 1990; Tutolo et al., 2016). Saad (1969) showed that ophiolitic serpentinites from Red Mountain (CA) increase in magnetic remanence and magnetic susceptibility in a manner that is proportional to the serpentinization degree of the rocks. Furthermore, the author calculated the porosity contents of the serpentinites based on the difference between their bulk and grain density, which also demonstrated that porosity increased proportionally with the serpentinization degree. Toft et al. (1990) expanded on these results by comparing experimental measurements of magnetic susceptibility and density of serpentinites with theoretical calculations of the evolution of density and susceptibility with increasing serpentinization degree. The authors noticed discrepancies between the empirical and theoretical results, which could be reconciled by invoking a multi-stage serpentinization process involving a progressive increase in magnetite precipitation and generation of porosity accompanying the serpentinization reactions. Tutolo et al. (2016) applied neutron scattering techniques to abyssal and ophiolitic serpentinites to demonstrate that increasing degrees of serpentinization are accompanied by generation of pores, and that these pores are typically smaller than 500 nm. These results are corroborated by measurements of density and porosity of serpentinites recovered by oceanic drilling, which show increasing porosity proportional to decreasing rock density (Iturrino et al., 1996; Kelemen et al., 2004). The newly generated pores are thought to either be inherent to secondary serpentine minerals and associated with structural

defects resulting from stacking disorders associated with compression of the brucite layer during buckling of lizardite (Wicks & Whittaker, 1977), or curling of chrysotile which generates tubular defects (Yada K., 1967), or formed as fracture porosity. Numerical and imaging analysis suggest the latter results from stresses generated at the serpentinization front due to the volume increase that accompanies serpentinization of primary ultramafic minerals (Jamtveit et al., 2008; Kelemen & Hirth, 2012; Plümpner et al., 2012). This volumetric expansion is capable of producing enough pressure to fracture the host rock and sustain the serpentinization reaction as more fluid and solute can infiltrate the rock and reach the serpentinization front (Kelemen & Hirth, 2012).

The expectation of increasing porosity with increasing degrees of serpentinization, coupled to the well-documented increase in Fe oxidation with increasing serpentinization (Evans, 2008; Mayhew & Ellison, 2020), implies that Fe oxidation (and H<sub>2</sub> generation) and porosity should be directly correlated in rocks of varying degrees of serpentinization. If such a correlation were demonstrated, then efforts to understand the reactive transport process of serpentinization would require that parameterizations of this correlation be incorporated into both conceptual and quantitative models. Here, we probe the coupled generation of porosity and oxidation of Fe by characterizing the bulk Fe content, Fe oxidation state, and porosity variations with serpentinization extent in abyssal peridotites.

## 4.2 Methods

### 4.2.1 *Geological samples*

All samples in this study were obtained from the International Ocean Discovery Program (IODP) Bremen Core Repository (BCR) and consist of abyssal serpentinites sampled by drilling from the Atlantic Ocean seafloor.

#### 4.2.1.1 ODP 109

In 1986 Leg 109 of the Ocean Drilling Program (ODP) drilled young oceanic crust adjacent to the Mid-Atlantic Ridge, with the goal of investigating crustal accretion processes at mid-oceanic spreading centers and how magmatic processes are interlinked with tectonic processes and hydrothermal activity (Detrick et al., 1988). It was one of the earliest expeditions to recover peridotite by ocean drilling (together with Deep Sea Drilling Project Legs 37, 45, 82). Hole A at Site 670 is located on the western flank of the Mid-Atlantic Ridge rift valley, south of the Kane Fracture Zone at 23°09.995'N, 45°01.930'W, and achieved a total penetration of 92.5 m with a total recovery of 6.52 m. The recovered rocks consisted almost entirely of serpentinized upper-mantle peridotites with serpentinization degree ranging from 50% to 100%, divided between serpentinites *in sensu stricto* showing >75% serpentinization and serpentinized harzburgite with less extensive serpentinization. Sample 109-670-A-5R1-143-146 included in this study was recovered from a depth of 46.63 meters below the seafloor (mbsf) and consists of serpentinized dunite showing a tortoise-shell (or “megamesh”) texture.

#### 4.2.1.2 ODP 173

During Ocean Drilling Program (ODP) Leg 173, six sites were drilled along the southern Iberia Abyssal Plain to investigate the validity of genetic models that explain the rift-to-drift evolution of the central part of the West Iberia rifted margin (Whitmarsh & Wallace, 2001). Site 1068 is located at 40°40.955'N, 11°36.720'W, between two continental basement ridges close to the deep portion of the ocean-continent transition (OCT) zone, south of the Iberia Abyssal Plain. Hole 1068A was drilled to a depth of 955.8 mbsf and resulted in the recovery of approximately 60 meters of heavily serpentinized peridotite (with serpentinization degree of 90% or higher) from the crystalline basement. The low abundance of platinum-group elements in peridotites from Site

1068 suggests that they are of subcontinental origin (Hébert et al., 2001). The samples included in this study were recovered from depths that range from ~895 mbsf to ~954 mbsf, and consist of heavily serpentinized peridotite (all showing > 90% serpentinization degree) with harzburgitic composition. Unlike most ultramafic rocks recovered at Site 1068 for which shipboard visual inspections revealed the presence of plagioclase, the samples investigated here contained no identifiable plagioclase.

#### 4.2.1.3 ODP 209

ODP Leg 209 aimed to test genetic models of focused melt extraction near magmatic ridge centers at slow-spreading ridges. During Leg 209, mafic and ultramafic rocks were recovered in the proximity of the Mid-Atlantic Ridge between 14°43'N and 15°39'N. Nineteen holes were drilled at eight sites along two linear N-S series subparallel to the ridge strike and offset by the 15°20' Fracture Zone. The main lithologies recovered during Leg 209 were upper mantle peridotites and gabbroic rocks that make up a magma-starved section of the Mid-Atlantic Ridge, and revealed the presence of localized deformation along shear zones and brittle faults (Kelemen et al., 2004). Here, we examine samples recovered from Site 1268, Site 1272, and Site 1274.

Site 1268 is located at 14°50.7552'N, 45°4.6409'W, to the west of a steep scarp from which the *Shinkai* 6500 submersible recovered peridotite and gabbroic dredge samples in 1998. Hole 1268A achieved a penetration of approximately 147 m, recovering more than 78 m of rock cores with lithologies dominated by harzburgite, followed by intrusive gabbroic rocks, and dunite.

Site 1272 is located at 15°5.6665'N, 44°58.3003'W, on the western flank of the Mid-Atlantic rift valley, south of the 15°20' Fracture Zone, and is part of the eastern series of holes explored during Leg 209. Hole 1272A achieved a penetration of 131 m, with 37.5 m of recovered rock core. Two main lithologic sections are identified from Hole 1272A, separated by fault gouge that likely marks

the presence of a fault plane. The upper ~55 mbsf are composed chiefly of gabbro with subordinate dunite and harzburgite, whereas the ~75 m of core that form the lower section are almost entirely made of harzburgite with minor gabbro and rare dunite.

Site 1274 is located at 15°38.867'N, 46°40.582'W, ~31 km north of the intersection between MAR and the 15°20' Fracture Zone along the western flank of the Mid-Atlantic rift valley, and is the northernmost site part of Leg 209. Hole 1274A penetrated to a depth of 156 mbsf with recovery limited to approximately 35 m and consisting chiefly of serpentized harzburgite, dunite, and subordinate gabbro.

Leg 209 samples studied here were recovered from variable depths ranging from ~16 mbsf to ~147 mbsf and all consist of harzburgite, apart from sample 209-1274-A-15R1-101-103, which has a dunitic protolith. All samples show a serpentinization degree greater than 75%, up to >99% in the dunitic sample.

#### *4.2.1.4 IODP 304/305*

Integrated Ocean Drilling Program Expedition 304 and 305 targeted Atlantis Massif, an oceanic core complex located at 30°N, ~15 km to the west of the median-axis valley of the Mid-Atlantic Ridge, to study the dynamics of oceanic core complex formation and the consequent exposure of ultramafic rocks in young oceanic lithosphere. Overall, the main lithologies recovered during Expedition 304/305 consists of gabbro and gabbroic rocks, which constitute ~91% of the total recovery (Blackman et al., 2006b). The samples studied here were sourced from Hole U1309B and U1309D.

Hole U1309B is located at 30°10.11'N, 42°7.11'W and achieved a total penetration of 101.8 m with recovery of 46.53m. The recovered lithologies are dominated by diabase and gabbro that form

two intrusive series separated by a relatively thin (2-4 m) interval of serpentized harzburgite. The samples from Hole U1309B studied here were all located at the interval between the intrusive series, located between ~58 and 60 mbsf. These samples are characterized by a weaker degree of serpentization than others we examine here, ranging from 65% to 78%, which is a common feature of peridotite found at the contact with gabbroic intrusions (Cannat et al., 1995; Blackman et al., 2006a).

Hole U1309D is located at 30°10.12'N, 42°7.11'W, achieved a total penetration of 1415.5 m, with core recovery of 799.65 m. Similar to Hole U1309B, the upper portion of Hole U1309D shows the presence of two intrusive series separated by serpentized peridotite, but ultramafic rocks were also encountered in deeper parts of the hole. The samples studied here are composed of harzburgite and lherzolite recovered at depths from ~130 to 330 mbsf and are 61% to 81% serpentized.

#### *4.2.1.5 IODP 357*

IODP Expedition 357 drilled an east-west transect across the southern wall of the Atlantis Massif and a shorter north-south transect towards the central dome of the oceanic massif. Seventeen short holes were drilled at nine sites to investigate the tectonomagmatic, metamorphic, and biological processes linking serpentization reactions and microbial processes in the oceanic subseafloor. The lithologies recovered range from sedimentary carbonate and chalk in the sedimentary cover to mafic intrusions and ultramafic rocks, with the latter being the dominant rock type (Früh-Green et al., 2017). The samples studied here were recovered from Site 68 Hole B (30°7.51'N 42°5.747'W, penetration of 9.6 m, 6.34 m of recovery), Site 71 Hole C (30°7.7'N 42°9.206'W, penetration of 12.15 m, recovery of 4.44 m), Site 72 Hole B (30°7.794'N 42°7.323'W, penetration of 12.43 m, recovery of 6.49 m), and Site 76 Hole B (30°7.621'N 42°7.065'W, penetration of 16.31

m, recovery of 11.71 m). The samples are serpentinized peridotite that vary in protolith composition from harzburgite to lherzolite and wehrlite, and are ~61 % to 84% serpentinized.

#### *4.2.2 Chemical dataset*

The serpentinite samples were ground under acetone using an automated agate mortar and pestle system. The ground samples were sieved and analyzed for whole-rock major and minor elements, Fe(II) and H<sub>2</sub>O content at Activation Laboratories, Ontario, Canada (Actlabs). The loss on ignition (LOI) was determined by measuring the weight loss after roasting the samples for two hours at 1000 °C . The roasted samples were then fused in disks obtained by combining 0.75 g of sample with 9.75 g of a mixture of lithium metaborate and lithium tetraborate with lithium bromide as a releasing agent. After fusing the mixture in platinum crucibles and casting it in platinum molds, the samples were analyzed by wavelength dispersive X-ray fluorescence (WDXRF). The FeO content of the samples was determined via redox titration by using a cold acid digestion of ammonium metavanadate and hydrofluoric acid in an open system, with addition of ferrous ammonium sulphate after complete digestion and using potassium dichromate as titrating agent (modified Wilson method based on Wilson, 1960). The moisture content of the samples (H<sub>2</sub>O-) was determined gravimetrically by heating 2 g of sample at 105 °C. From the dried sample 0.3 g were collected and thermally decomposed at 1000 °C using an ELTRA CW-800 in a pure nitrogen atmosphere to determine the water content (H<sub>2</sub>O). The amount of H<sub>2</sub>O released during thermal decomposition was quantified via infrared absorption spectroscopy.

#### *4.2.3 Porosity dataset*

The samples were cut with a diamond saw to obtain approximately regular rectangular cuboids, with an average volume of approximately 1 cm<sup>3</sup>. The volume of the cuboids was then determined using a digital micrometer to measure the length of their sides. When the original sample was too

small or too fractured to obtain regular cuboids, a glass beads method was used instead (Consolmagno & Britt, 1998). Specifically, we measured the mass and standardized the internal volume of a small container (less than approximately 10 times the volume of the measured samples) by filling it with glass beads with 10  $\mu\text{m}$  diameter and known density. Assuming that the pore space between the glass beads is negligible, we measured the mass of the glass beads to calculate the internal volume of the container. The container volume was standardized by repeating the measurement 15 times to determine a standard deviation of  $\pm 0.015 \text{ cm}^3$ . Subsequently, we tested the volumetric measurement on a steel sphere of known volume and determined that 5-10 measurements per sample were sufficient to obtain a standard deviation of less than  $\pm 0.020 \text{ cm}^3$ . We then placed a sample with unknown volume in the standardized container, filled the remaining volume with glass beads and measured its total mass, which allows calculation of the sample volume according to:

$$V_r = \frac{V_c * (M_g - M_s + m_r)}{M_g - m_c} \quad \text{Eq. 4-1}$$

where  $V_r$  is the sample volume,  $V_c$  is the container volume,  $M_g$  is the mass of the container filled only with glass beads,  $M_s$  is the mass of the container filled with glass beads plus the sample,  $m_r$  is the sample mass,  $m_c$  is the mass of the empty container. The results of the volumetric determinations were used to normalize helium pycnometry measurements. Briefly, He-pycnometry relies on Boyle's law to calculate the grain density of the analyzed sample by measuring the pressure change between a reference cell and a sample-holding cell. Subtracting the grain density of the sample from its pre-determined bulk density permits porosity calculation. The standard deviation of the porosity measurements was determined with repeated acquisitions of grain density measurements. For the present dataset, five to eight measurement per sample were

sufficient to reduce the standard deviation to acceptable values (typically below 0.5%). He-pycnometry measurements were collected with a Quantachrome Instruments MVP-D160-E multipycnometer, according to a modified version of the method described by Consolmagno and Britt (1998), with the additional employment of cylindrical stainless steel spacers to minimize the empty volume within the sample holder of the He-pycnometer and thereby improve accuracy. All samples were dried in an oven at 60 °C for 24 h before running the pycnometry measurements.

#### *4.2.4 Data processing and analyses*

The chemical and porosity datasets were combined to investigate the presence of relevant trends. A preliminary analysis was carried out by producing a correlation matrix that encompassed all measured properties (Appendix C). To reduce the complexity of the combined dataset, concentrations of several oxides, namely CuO, K<sub>2</sub>O, TiO<sub>2</sub>, P<sub>2</sub>O<sub>5</sub>, V<sub>2</sub>O<sub>5</sub>, were excluded from the preliminary analysis as their values were close to or below the analytical detection limit. Moreover, to avoid redundancy, we utilized the H<sub>2</sub>O content of the analyzed samples in place of the results of LOI, because the latter results from the release of a range of volatiles species including CO<sub>2</sub> and S and is therefore a less direct proxy of the hydration reactions (i.e., serpentinization) experienced by the samples. The dimension of the preliminary correlation matrix was reduced by considering only properties that show a degree of correlation with the main features investigated in this study, i.e., Fe abundance in the form of FeO, Fe<sub>2</sub>O<sub>3</sub>, total Fe<sub>2</sub>O<sub>3</sub> (Fe<sub>2</sub>O<sub>3</sub>T), FeIII/total Fe (FeIII/FeT), and porosity content. The correlation was evaluated based on the Pearson's r coefficient with a cutoff value chosen for  $0 < r < 0.45$  and  $-0.45 < r < 0$ . The moisture content (H<sub>2</sub>O-) was also excluded from further investigation even though it showed a positive correlation with porosity values with an r coefficient of 0.58, because the data distribution showed independency from porosity variations and is likely not representative of the serpentinization process. A reduced correlation

matrix that encompasses the variables FeO, H<sub>2</sub>O, SiO<sub>2</sub>, Al<sub>2</sub>O<sub>3</sub>, Fe<sub>2</sub>O<sub>3</sub>T, MnO, MgO, Cr<sub>2</sub>O<sub>3</sub>, Fe<sub>2</sub>O<sub>3</sub>, Fe<sup>III</sup>/Fe<sup>T</sup>, and porosity was thus obtained.

The correlated properties obtained from the reduced correlation matrix were subjected to a Principal Component Analysis (PCA) algorithm for dimensionality reduction and to ascertain the most prominent features capable of explaining the variance of the dataset. Before running the processing algorithm, the porosity values were normalized by their standard deviations ( $\Phi_n$ ) to account for analytical uncertainty (Tamuz et al., 2005), and the whole dataset was normalized to achieve comparable values and prevent artificially heavier loadings for properties with greater absolute values.

An approximate primary modal mineralogy relevant to abyssal peridotite protoliths was reconstructed via a simplified CIPW (Hollocher, 2004). The oxide wt% were normalized to a total of 100 after subtracting the water content (H<sub>2</sub>O wt%). Furthermore, to produce a normative mineralogy that included only olivine, orthopyroxene, clinopyroxene, and chromite, the inputs for the CIPW calculator were limited to the SiO<sub>2</sub>, MnO, MgO, CaO, Cr and Fe contents with the latter converted to FeO total.

## 4.3 Results

### 4.3.1 Protolith classification

The results of the chemical analysis and pycnometry measurements are reported in Table 4 - 1. A lithologic classification of the protolith for each sample is also reported in Table 4 - 1 and plotted in the ternary diagram shown in Fig. 4 - 1. All analyzed samples have peridotite protolith as they contain < 45 wt% SiO<sub>2</sub> (Table 4 - 1) and > 40 wt% olivine (Fig. 4 - 1). The vast majority of samples (75%) included in this study plots in the harzburgite field, as would be expected from serpentinites

recovered by drilling from the seafloor of the Atlantic Ocean. In fact, harzburgites represent 75% of ultramafic rocks sampled from the Mid-Atlantic Ridge (Warren, 2016). One sample recovered during ODP Leg 109 and one from ODP Leg 209 plot in the dunite field, three IODP 304 samples and one IODP 357 sample are more primitive and plot as lherzolite, and one IODP 357 sample plots in the right part of the ternary diagram as wehrlite.

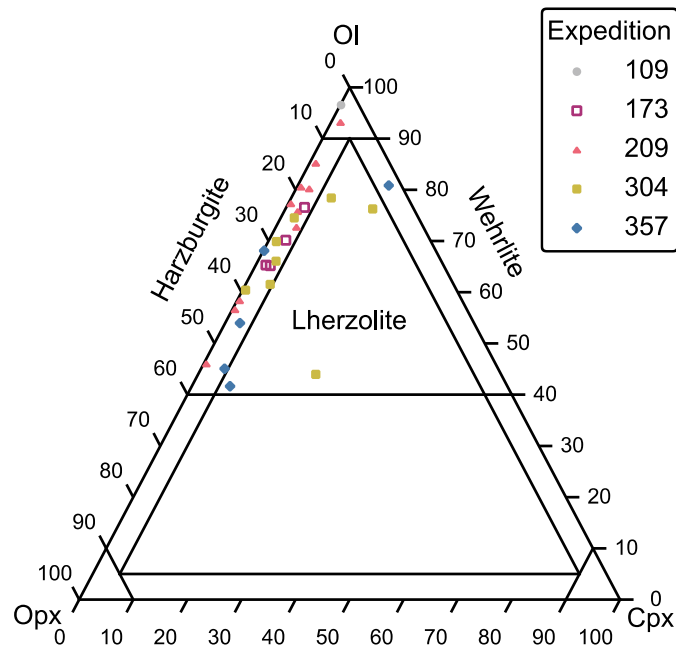


Fig. 4 - 1. Ternary diagram showing the lithologic classification of the peridotite protolith of the analyzed serpentinites. Most samples plot in the harzburgite field, with the exception of two dunites, four lherzolite and one wehrlite.

Table 4 - 1. Results of chemical analyses via WD-XRF, titrations and gravimetric method, and results of CIPW normative calculation.

Sample ID	IGSN number	LOI	H2O- wt%	H2O wt%	SiO2 wt%	Al2O3 wt%	Fe2O3T wt%	Fe2O3 wt%	FeO wt%	MnO wt%
109-670-A-5R1-143-146	IBCR0109RXLXY14	15.04	1	14.3	34.51	0.55	8.74	6.51	2	0.129
173-1068-A-21R1-11-15	IBCR0173RFXFY14	14.15	0.8	13.4	39.33	0.36	5.69	3.02	2.4	0.103
173-1068-A-28R1-5-6	IBCR0173RXHXY14	15.84	1.3	14.2	36.49	1.14	7.4	5.62	1.6	0.111
173-1068-A-29R2-21-24	IBCR0173RXIXY14	20.11	6.1	13.7	35.84	1.62	6.6	4.15	2.2	0.091
173-1068-A-29R3-29-32	IBCR0173RXKXY14	14.23	1	13.4	38.97	1.24	6.77	4.1	2.4	0.094

209-1268-A-2R2-44-46	IBCR0209RXYWY14	12.17	0.7	11.8	40.71	0.55	7.44	5.44	1.8	0.055
209-1268-A-3R2-112-114	IBCR0209RXZWY14	13.15	1	11	41.74	0.42	7.62	4.29	3	0.064
209-1268-A-15R3-88-91	IBCR0209RX1XY14	12.46	0.6	12.1	41.43	0.48	6.77	2.43	3.9	0.107
209-1272-A-16R1-121-123	IBCR0209RX6XY14	15.26	1.2	13.9	37.16	0.64	7.24	5.23	1.8	0.095
209-1272-A-26R1-65-67	IBCR0209RX8XY14	15.38	1.2	14	36.34	0.45	7.42	5.64	1.6	0.112
209-1274-A-5R1-118-120	IBCR0209RX9XY14	13.7	1	12.7	37.57	0.59	7.55	4.88	2.4	0.119
209-1274-A-6R2-70-72	IBCR0209RXAXY14	12.59	0.8	11.7	39.05	0.8	7.6	6.05	1.4	0.117
209-1274-A-15R1-101-103	IBCR0209RXBXY14	15.9	1	14.6	34.33	0.27	7.7	6.37	1.2	0.106
209-1274-A-16R1-76-77	IBCR0209RXCXY14	15.08	1	14.4	35.76	0.44	7.58	6.02	1.4	0.108
209-1274-A-27R1-58-61	IBCR0209RDXXY14	12.32	0.8	11.8	38.47	0.64	7.45	4.78	2.4	0.102
304-1309-B-11R1-98-100	IBCR0304RXJWY14	10.16	0.5	9.6	38.67	0.78	9.07	6.17	2.6	0.114
304-1309-B-11R1-110-114	IBCR0304RXKWY14	11.6	0.7	10.9	39.85	1.74	9.03	5.69	3	0.164
304-1309-B-11R2-32-34	IBCR0304RXLWY14	12.44	0.7	11.4	38.44	0.95	8.38	6.6	1.6	0.095
304-1309-D-23R1-142-143	IBCR0304RXNWX14	12.16	1.1	10.4	39.11	1.53	8.88	5.76	2.8	0.117
304-1309-D-27R3-12-15	IBCR0304RXOWY14	9.85	0.5	9	40.3	6.11	7.26	4.14	2.8	0.102
304-1309-D-31R1-18-21	IBCR0304RXPWY14	12.39	0.7	11.9	40.57	0.27	7.19	5.41	1.6	0.047
304-1309-D-63R3-54-57	IBCR0304RXRWY14	10.52	0.5	10.3	36.4	3.91	11.09	5.86	4.7	0.17
304-1309-D-64R1-56-58	IBCR0304RXSWY14	10.51	0.6	10.2	37.66	1.37	10.13	6.35	3.5	0.148
357-68-B-4R1-18-26	IBCR0357RXDWY14	9.7	0.8	8.9	42.44	3.14	7.44	3.77	3.3	0.116
357-68-B-4R1-51-54	IBCR0357RXFWY14	10.99	1.1	10.2	41.13	1.59	8.22	4.77	3.1	0.113
357-71-C-5R1-19-24	IBCR0357RXGWY14	12.31	0.6	12.4	39.3	0.76	8.37	7.03	1.2	0.074
357-72-B-8R2-47-49	IBCR0357RXHWY14	10.66	0.7	9.8	44.33	0.81	7.95	5.28	2.4	0.101
357-76-B-8R1-123-126	IBCR0357RXIWY14	15.48	0.8	11.5	36	0.61	7.96	6.4	1.4	0.149
Average		13.08	1.03	11.91	38.64	1.21	7.88	5.28	2.34	0.11

Table 4 - 1 continued.

Sample ID	MgO wt%	CaO wt%	Cr2O3 wt%	NiO wt%	Na2O wt%	K2O wt%	TiO2 wt%	Co3O4 wt%	CuO wt%	P2O5 wt%
109-670-A-5R1-143-146	40.6	0.03	0.28	0.3	0.06	< 0.01	0.01	0.018	< 0.005	0.01
173-1068-A-21R1-11-15	38.17	0.4	0.2	0.162	0.11	< 0.01	0.01	0.015	< 0.005	0.01
173-1068-A-28R1-5-6	37.16	0.7	0.32	0.25	0.06	< 0.01	0.02	0.013	< 0.005	< 0.01
173-1068-A-29R2-21-24	35.15	0.62	0.28	0.258	0.07	< 0.01	0.04	0.013	< 0.005	0.01
173-1068-A-29R3-29-32	37.08	0.58	0.23	0.202	0.08	< 0.01	0.02	0.011	< 0.005	0.01
209-1268-A-2R2-44-46	36.94	0.02	0.31	0.28	0.11	0.01	0.01	0.017	< 0.005	0.01
209-1268-A-3R2-112-114	34.5	0.02	0.25	0.258	0.08	0.01	0.01	0.014	0.005	< 0.01

209-1268-A-15R3-88-91	37.53	0.02	0.23	0.27	0.09	< 0.01	0.01	0.014	< 0.005	< 0.01
209-1272-A-16R1-121-123	38.68	0.02	0.29	0.299	0.12	< 0.01	0.01	0.014	< 0.005	< 0.01
209-1272-A-26R1-65-67	38.61	0.07	0.21	0.289	0.08	< 0.01	< 0.01	0.014	< 0.005	0.01
209-1274-A-5R1-118-120	39.62	0.44	0.23	0.288	0.04	< 0.01	0.03	0.018	< 0.005	< 0.01
209-1274-A-6R2-70-72	38.75	0.75	0.29	0.268	0.04	0.01	0.02	0.017	< 0.005	0.01
209-1274-A-15R1-101-103	39.64	0.28	0.28	0.294	0.05	< 0.01	0.01	0.016	< 0.005	0.01
209-1274-A-16R1-76-77	39.1	0.16	0.31	0.294	0.04	< 0.01	0.01	0.011	< 0.005	< 0.01
209-1274-A-27R1-58-61	39.3	0.46	0.3	0.287	0.04	< 0.01	0.01	0.018	< 0.005	0.01
304-1309-B-11R1-98-100	38.28	0.55	0.31	0.269	0.07	< 0.01	0.04	0.017	< 0.005	0.01
304-1309-B-11R1-110-114	35.36	0.98	0.4	0.172	0.1	0.01	0.07	0.015	< 0.005	0.01
304-1309-B-11R2-32-34	37.12	0.32	0.39	0.266	0.05	< 0.01	0.01	0.014	< 0.005	0.01
304-1309-D-23R1-142-143	36.18	0.72	0.4	0.23	0.06	< 0.01	0.06	0.015	< 0.005	0.01
304-1309-D-27R3-12-15	29.67	4.51	0.33	0.215	0.56	0.01	0.07	0.016	< 0.005	0.01
304-1309-D-31R1-18-21	37.6	0.12	0.14	0.289	0.08	0.01	0.01	0.012	< 0.005	0.01
304-1309-D-63R3-54-57	34.88	1.57	0.59	0.208	0.1	0.01	0.07	0.017	0.005	0.01
304-1309-D-64R1-56-58	34.88	3.52	0.62	0.208	0.11	< 0.01	0.09	0.017	0.009	0.01
357-68-B-4R1-18-26	34.28	0.94	0.34	0.232	0.21	0.11	0.04	0.015	< 0.005	0.01
357-68-B-4R1-51-54	35.46	0.59	0.15	0.286	0.15	0.15	0.03	0.016	< 0.005	0.01
357-71-C-5R1-19-24	37.81	0.03	0.25	0.188	0.06	< 0.01	0.01	0.009	< 0.005	0.01
357-72-B-8R2-47-49	34.42	1.58	0.28	0.245	0.15	0.01	0.02	0.014	< 0.005	0.01
357-76-B-8R1-123-126	35.64	3.55	0.36	0.251	0.13	0.01	0.02	0.014	< 0.005	0.01
Average	36.87	0.84	0.31	0.25	0.10	0.03	0.03	0.01	0.01	0.01

Table 4 - 1 continued.

Sample ID	V2O5 wt%	Total	Porosity	Porosity St. Dev	Olivine	Cpx	Opx	Spinel	Lithology
109-670-A-5R1-143-146	< 0.003	100	6.66	0.1	95.81	0.14	3.29	0.77	Dunite
173-1068-A-21R1-11-15	0.004	99	14.71	0.17	65.02	1.87	32.69	0.42	Harzburgite
173-1068-A-28R1-5-6	0.007	99.7	4.93	0.26	76.05	3.35	19.94	0.66	Harzburgite
173-1068-A-29R2-21-24	0.007	101	17.95	0.5	69.65	3.10	26.54	0.71	Harzburgite
173-1068-A-29R3-29-32	< 0.003	99.8	12.02	0.12	64.84	2.72	31.92	0.52	Harzburgite
209-1268-A-2R2-44-46	0.005	98.8	9.21	0.13	57.83	0.09	41.37	0.71	Harzburgite
209-1268-A-3R2-112-114	0.005	98.5	8.84	0.11	45.59	0.09	53.66	0.66	Harzburgite
209-1268-A-15R3-88-91	0.005	99.9	6.53	0.17	56.10	0.09	43.14	0.68	Harzburgite
209-1272-A-16R1-121-123	< 0.003	100	7.62	0.2	76.56	0.09	22.57	0.77	Harzburgite
209-1272-A-26R1-65-67	< 0.003	99.2	2.11	0.96	79.81	0.33	19.10	0.75	Harzburgite

209-1274-A-5R1-118-120	0.003	100	10.37	0.35	79.50	2.02	17.76	0.73	Harzburgite
209-1274-A-6R2-70-72	0.005	100	5.86	0.16	72.08	3.40	23.85	0.67	Harzburgite
209-1274-A-15R1-101-103	< 0.003	99	1.38	0.37	92.31	1.34	5.58	0.77	Dunite
209-1274-A-16R1-76-77	< 0.003	99.1	3.35	0.16	84.41	0.76	14.07	0.76	Harzburgite
209-1274-A-27R1-58-61	0.004	99.7	5.17	0.18	75.08	2.10	22.11	0.72	Harzburgite
304-1309-B-11R1-98-100	0.006	98.6	3.39	0.16	74.02	2.49	22.81	0.67	Harzburgite
304-1309-B-11R1-110-114	0.007	99.8	2.45	0.19	61.28	4.52	33.76	0.43	Harzburgite
304-1309-B-11R2-32-34	0.009	98.7	4.28	0.17	69.42	1.49	28.41	0.68	Harzburgite
304-1309-D-23R1-142-143	0.011	99.8	7.44	0.09	65.69	3.33	30.40	0.58	Harzburgite
304-1309-D-27R3-12-15	0.011	99.3	3.46	0.35	43.71	21.64	34.08	0.57	Lherzolite
304-1309-D-31R1-18-21	< 0.003	98.9	4.93	0.26	59.97	0.55	38.76	0.73	Harzburgite
304-1309-D-63R3-54-57	0.009	100	5.58	1.01	77.99	7.37	14.11	0.53	Lherzolite
304-1309-D-64R1-56-58	0.014	99.6	1.02	0.36	75.88	16.05	7.56	0.52	Lherzolite
357-68-B-4R1-18-26	0.008	99.4	2.23	0.06	44.80	4.32	50.29	0.59	Harzburgite
357-68-B-4R1-51-54	0.004	99.2	1.58	0.19	53.59	2.71	42.98	0.72	Harzburgite
357-71-C-5R1-19-24	0.006	99.3	3.97	0.42	67.79	0.14	31.60	0.47	Harzburgite
357-72-B-8R2-47-49	0.006	101	1.67	0.56	41.40	7.02	50.98	0.60	Lherzolite
357-76-B-8R1-123-126	0.004	100	8.85	0.21	80.32	16.71	2.32	0.65	Wherlite
Average	0.01		5.98	0.28					

#### 4.3.2 Correlation matrix

Only a subset of the correlation matrix spanning the variables reported in Table 4 - 1 shows a Pearson's coefficient higher than 0.45 for positive correlations and lower than -0.45 for negative correlations (Fig. 4 - 2; a correlation matrix spanning the full range of analyzed variables can be found in Appendix C). Several correlations are identifiable in Fig. 4 - 2, however only a few are clearly defined. The H<sub>2</sub>O content, a proxy for the degree of serpentinization (Evans, 2008), is negatively correlated with FeO content ( $r = -0.58$ ), has a weak positive correlation with Fe<sup>III</sup>/Fe<sup>T</sup> ( $r = 0.42$ ) and appears independent of the Fe<sub>2</sub>O<sub>3</sub> abundance. H<sub>2</sub>O is also positively correlated with MgO ( $r = 0.70$ ), and is negatively correlated with SiO<sub>2</sub> and Al<sub>2</sub>O<sub>3</sub> ( $r = -0.66$  and  $-0.56$ ,

respectively). FeO content is positively correlated with  $\text{Al}_2\text{O}_3$  ( $r = 0.51$ ) and anticorrelated with MgO,  $\text{Fe}_2\text{O}_3$  and, consequently, FeIII/FeT ( $r = -0.49$ ,  $-0.46$ , and  $-0.88$ , respectively). MgO is anticorrelated with  $\text{Al}_2\text{O}_3$  ( $r = -0.77$ ). The total Fe content expressed by  $\text{Fe}_2\text{O}_3\text{T}$  is positively correlated with both  $\text{Cr}_2\text{O}_3$  and MnO contents ( $r = 0.76$  and  $0.60$ , respectively) and anticorrelated with porosity ( $r = -0.49$ ).

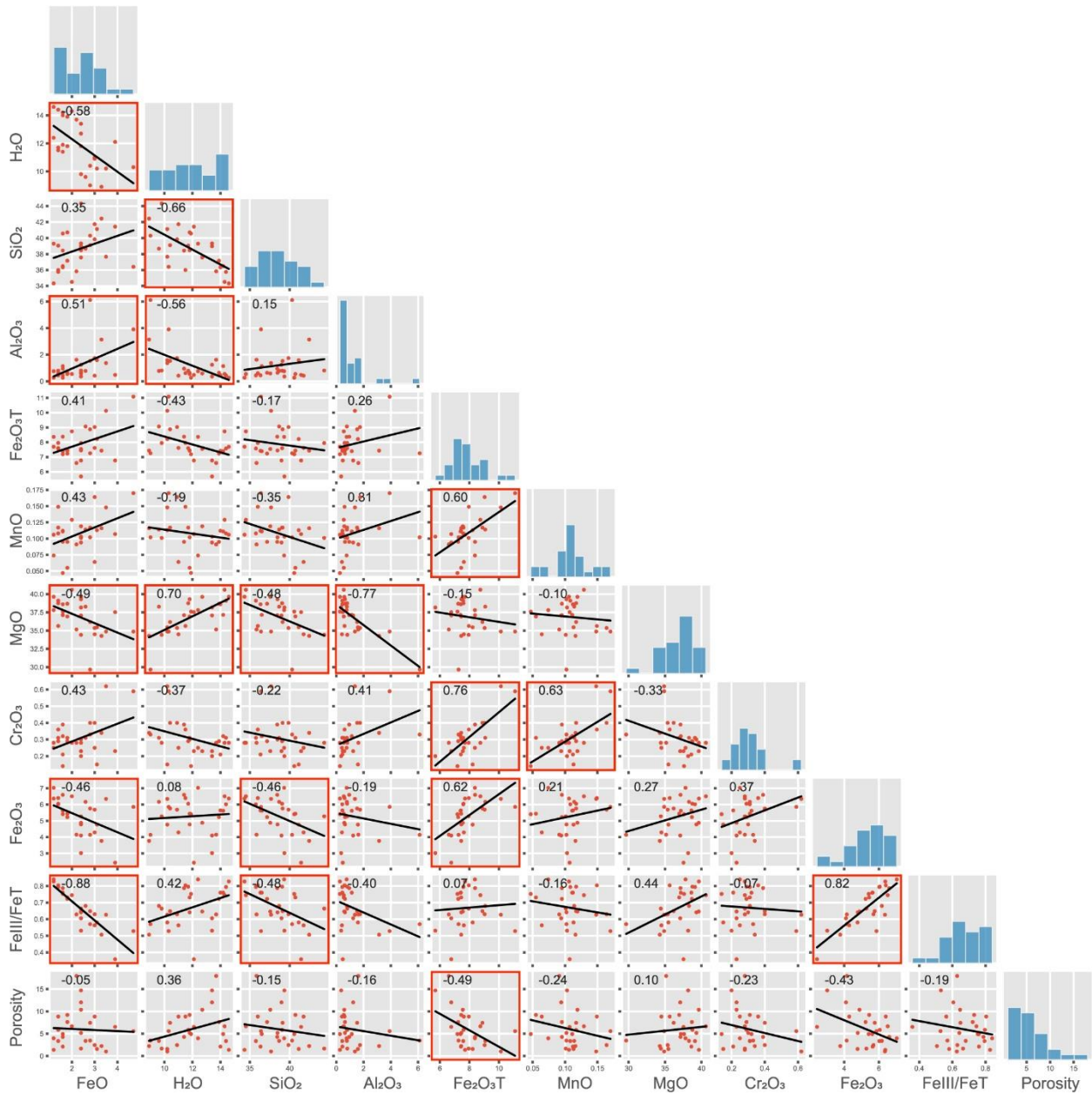


Fig. 4 - 2. Correlation matrix spanning measured properties minus oxides that resulted too close to the detection limit of the technique employed. Biplots that show Pearson coefficient greater than 0.45 and smaller than -0.45 have been marked with red squares. Only the bottom half of the correlation matrix has been plotted to facilitate its interpretation.

#### 4.3.3 Principal component analysis

We have explored the presence of correlations between porosity, Fe content, Fe redox state of serpentinized peridotites and other relevant correlations that were previously highlighted by

investigating the covariance of these properties via principal component analysis (PCA). The spread in values of the data analyzed by PCA shows that porosity (normalized according to its standard deviation, Tamuz et al., 2005) covers a wider range than the rest of the variables considered (Fig. 4 - 3).

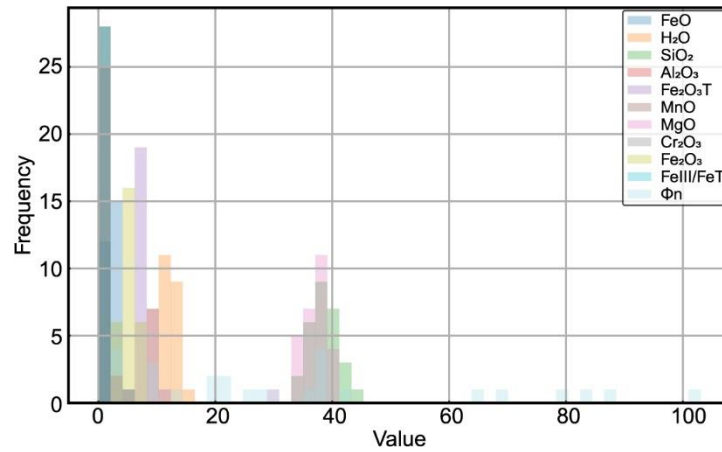


Fig. 4 - 3. Histogram showing the spread in values of the properties included in the PCA analysis. Normalized porosity is spread over a significantly wider range than the other properties.

Hence, the statistical analysis proposed here was preceded by a normalization step to prevent spurious clustering of properties according to the magnitude of their absolute values. The scree diagram (Fig. 4 - 4a) shows that only weak correlations were found, as the first principal component that explains the highest degree of variance in the PCA analysis covers less than 40% of the total. Moreover, five components are required to explain more than 95% of the dataset, indicating a poor degree of covariance between the variables considered.

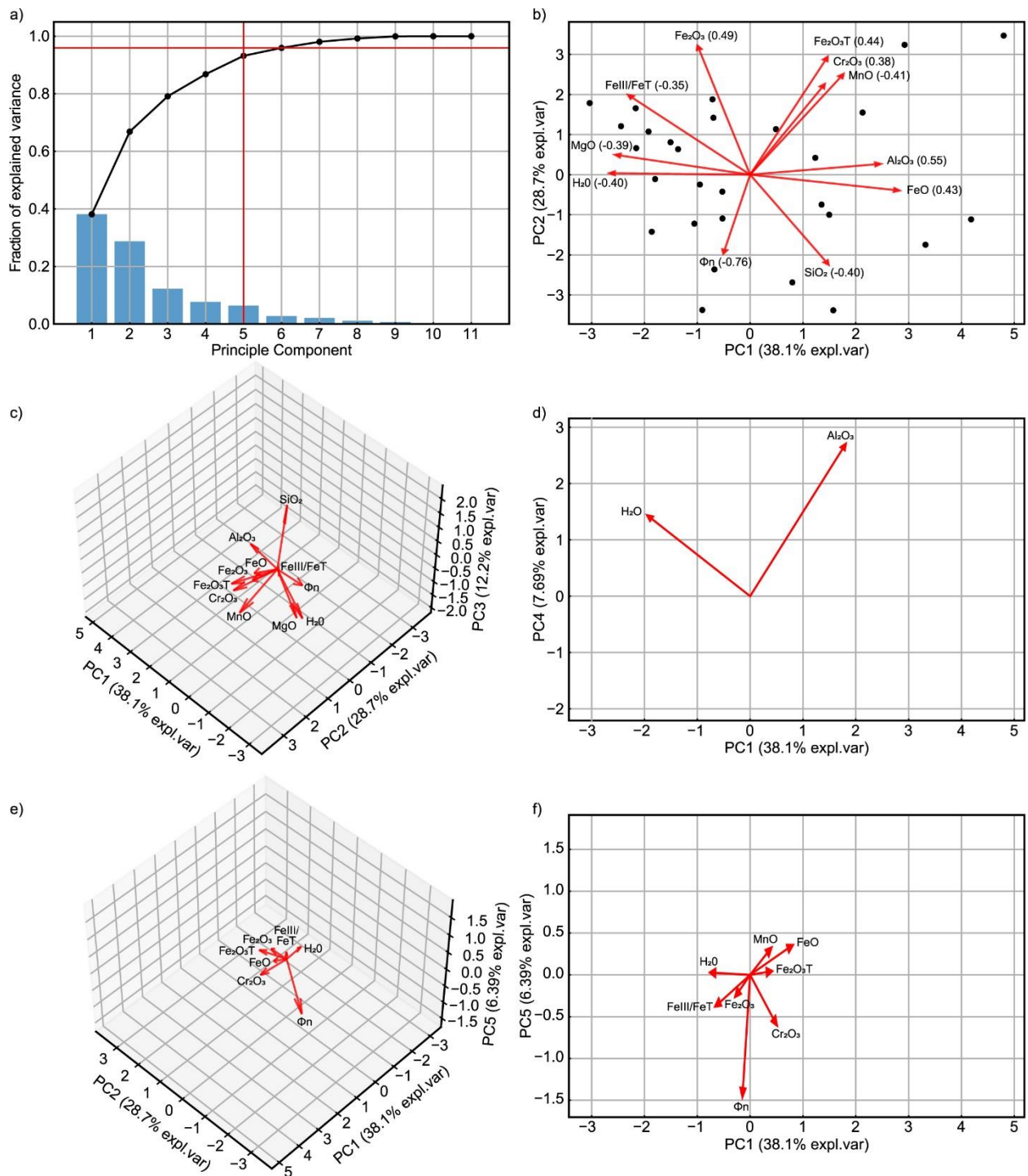


Fig. 4 - 4. Results of the PCA analysis. a) scree plot showing overall low degree of covariance. b) PC1-PC2 diagram reporting the data points scatter and the loadings of all variables included in the PCA analysis. c) 3D diagram with all loadings plotted in a PC1-PC2-PC3 space. d) The loadings for H<sub>2</sub>O and Al<sub>2</sub>O<sub>3</sub> are projected in a PC1-PC4 space which best describes those variables (Table 4 - 2). e) 3D plot in PC1-PC2-PC5 space of  $\Phi_n$ , Fe redox species, and serpentinization degree tracked via water content. f) Projection of

the PCA loading vectors shown in Fig. 4 - 4e plus MnO in PC1-PC5 space.  $\Phi_n$  is an isolated vector and does not reveal positive or negative correlations.

The loadings vectors that represent Fe<sub>2</sub>O<sub>3</sub>, Cr<sub>2</sub>O<sub>3</sub>, and MnO are subparallel (Fig. 4 - 4b) and thus indicate some degree of correlation, as was highlighted by the correlation matrix (Fig. 4 - 2). Furthermore, because the principal components that best describe Fe<sub>2</sub>O<sub>3</sub>T, Cr<sub>2</sub>O<sub>3</sub>, and MnO are the second and third principal components (Table 4 - 2), the 3D diagram in Fig. 4 - 4c can be used to clarify their relationships. Fe<sub>2</sub>O<sub>3</sub>T and Cr<sub>2</sub>O<sub>3</sub> are apparently correlated, whereas MnO appears to deviate from the former vectors (Fig. 4 - 4c). The MgO and H<sub>2</sub>O vectors (Fig. 4 - 4b) have similar slopes and score values (-0.39 and -0.40, respectively), are subparallel to the PC1 axis that is their best descriptor (Table 4 - 2), and, thus, their variance appears well explained by the PCA analysis. Furthermore, they appear anticorrelated with the FeO contents, with FeO and MgO projecting as symmetrically opposite vectors in the PCA space. Because the first principal component is the best descriptor of MgO, FeO, and H<sub>2</sub>O, their correlation appears valid. Al<sub>2</sub>O<sub>3</sub> seems anticorrelated with H<sub>2</sub>O, however the correlation is apparent and results from the projection of all PCA loadings on a two-dimensional PC1-PC2 space (Fig. 4 - 4b). Whereas H<sub>2</sub>O is best explained by the first principal component, Al<sub>2</sub>O<sub>3</sub> is instead best described by the fourth principal component (Table 4 - 2). Fig. 4 - 4d shows that H<sub>2</sub>O and Al<sub>2</sub>O<sub>3</sub> projected in a PC1-PC4 space are diverging vectors without evident correlation. Similarly, the apparent anticorrelation between SiO<sub>2</sub> against Fe<sub>2</sub>O<sub>3</sub> and FeIII/FeT contents also results from projection onto a PC1-PC2 space, and when projected in a 3D space they appear as diverging vector without evident correlations (Fig. 4 - 4c).

Table 4 - 2. List of principal components that best describe each property analyzed via PCA. Also reports the cumulative explained variance across the 11 calculated components.

<b>Principal component</b>	<b>Property</b>	<b>Loading</b>	<b>Type</b>	<b>Principal component</b>	<b>Cumulative explained variance</b>
PC1	FeO	0.426874	best	PC1	0.38
PC2	Fe <sub>2</sub> O <sub>3</sub>	0.486575	best	PC2	0.67
PC3	MnO	-0.408422	best	PC3	0.79

PC4	Al <sub>2</sub> O <sub>3</sub>	0.547941	best	PC4	0.87
PC5	Φ <sub>n</sub>	-0.758105	best	PC5	0.93
PC1	H <sub>2</sub> O	-0.402578	weak	PC6	0.96
PC4	SiO <sub>2</sub>	-0.403543	weak	PC7	0.98
PC2	Fe <sub>2</sub> O <sub>3</sub> T	0.444827	weak	PC8	0.99
PC1	MgO	-0.38686	weak	PC9	1.00
PC2	Cr <sub>2</sub> O <sub>3</sub>	0.380915	weak	PC10	1.00
PC1	Fe <sup>III</sup> /Fe <sup>T</sup>	-0.348126	weak	PC11	1.00

The normalized porosity vector ( $\Phi_n$ ) is isolated in a PC1-PC2 space (Fig. 4 - 4a) and appears to have a weakly defined anticorrelation with the vectors cluster that represents the PCA loadings for Fe<sub>2</sub>O<sub>3</sub>T, Cr<sub>2</sub>O<sub>3</sub>, and MnO, although further investigation indicates that MnO shows only an apparent correlation (Fig. 4 - 4c). Because the best descriptors of  $\Phi_n$ , Fe<sub>2</sub>O<sub>3</sub>T, and Cr<sub>2</sub>O<sub>3</sub> are the principal components two and five, they are plotted in a 3D diagram in Fig. 4 - 4e together with other expressions of the Fe budget, Fe redox state, and H<sub>2</sub>O content used as a proxy for the serpentinization degree. Porosity is represented by an isolated vector that does not show relevant positive or negative correlations. This idea is strengthened by the PC1-PC5 plot in Fig. 4 - 4f, which is the PC space that best describes the porosity variations.

#### 4.3.4 Modal composition and terrestrial array

The variations in MgO and SiO<sub>2</sub> contents can be explained by the modal composition of the rock. Indeed, peridotites that are poorer in modal pyroxene and thus enriched in modal olivine are more primitive, and thus they are enriched in MgO and depleted in SiO<sub>2</sub> (Fig. 4 - 5a). The modal composition also exerts a less defined but traceable control on the bulk Al composition of the rock, so that samples richer in clinopyroxene have higher Al<sub>2</sub>O<sub>3</sub> contents (Fig. 4 - 5b).

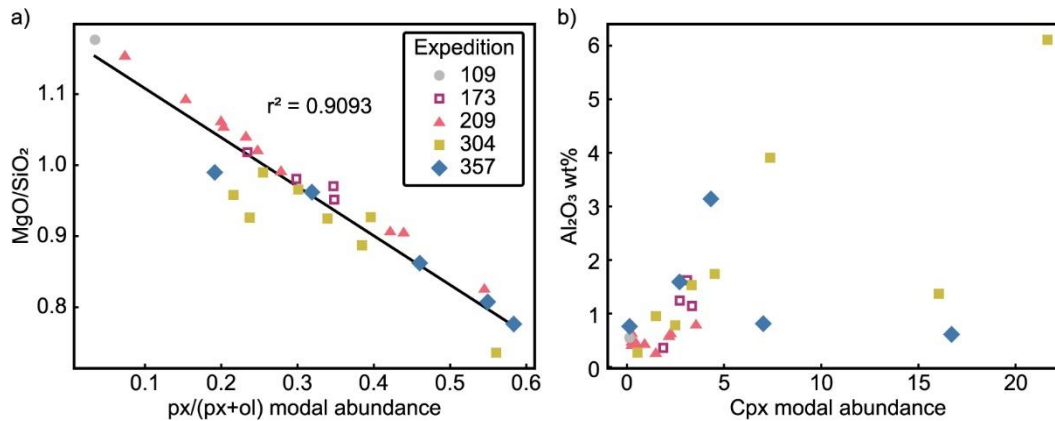


Fig. 4 - 5. Geochemical trends related to mineralogic modes. a) The MgO/SiO<sub>2</sub> ratio strongly correlates with the modal composition, increasing when greater amounts of olivine are part of the mineral assemblage of the peridotite protolith. b) The Al<sub>2</sub>O<sub>3</sub> content of the analyzed samples loosely correlates with the modal content of clinopyroxene.

Further investigation of the MgO/SiO<sub>2</sub> ratio can be performed by comparing the bulk geochemical composition of the dataset analyzed in this study and the terrestrial melting array (Fig. 4 - 6), which represents the composition attained by rocks that experienced successive magmatic depletion starting from a primitive mantle composition (Hart & Zindler, 1986; Jagoutz et al., 1979; Paulick et al., 2006). The majority of data points plots beneath the terrestrial melting array curve (Fig. 4 - 6), and few samples from Expedition 304 and 357 follow a trend towards decreasing MgO/SiO<sub>2</sub> and increasing Al<sub>2</sub>O<sub>3</sub>/SiO<sub>2</sub> values.

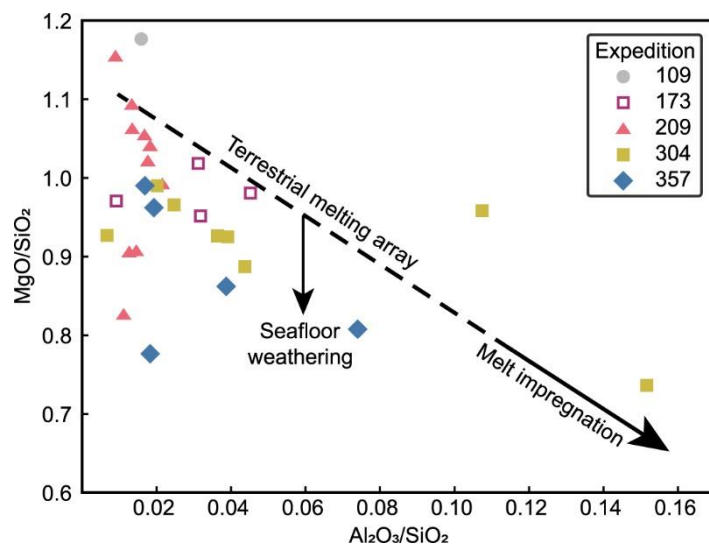


Fig. 4 - 6. Geochemical evolution of altered peridotites. Most of the presented dataset plots below the terrestrial melting array, suggesting that the majority of samples included in this study experienced varying degrees of seafloor weathering. Samples that plot parallel to the terrestrial melting array, towards decreasing MgO/SiO<sub>2</sub> and increasing Al<sub>2</sub>O<sub>3</sub>/SiO<sub>2</sub> are indicative of impregnation by gabbroic melts.

## 4.4 Discussion

### 4.4.1 Representativity of the dataset

The abyssal serpentinites analyzed in this study show several features previously highlighted elsewhere. The average FeO content determined in this study (2.3 wt%) matches that calculated from whole-rock analysis of highly to completely serpentinized peridotites reported by Evans (2008). Moreover, the average Fe<sup>III</sup>/Fe<sup>T</sup> ratio we determine, 0.67, is similar to those reported for mid-oceanic ridge oceanic core complexes elsewhere: 0.69 (Evans, 2008), 0.66 (Klein et al., 2014), and 0.61 (Mayhew & Ellison, 2020). The average Fe content recalculated as FeO total in this study, 7.09 wt%, is also similar to the average value determined from the comprehensive compilation of Mayhew and Ellison (2020), 7.22 wt%. Those authors identified several general trends which can also be seen in our sample collection. For example, the total Fe content of serpentinites has a slight inverse proportionality to the degree of serpentinization (tracked via the H<sub>2</sub>O wt% in this study), and is directly proportional to the amount of oxidized Fe (Fe<sub>2</sub>O<sub>3</sub> vs Fe<sub>2</sub>O<sub>3</sub>T), so that their

relationships are best expressed by FeIII/FeT against H<sub>2</sub>O content (Fig. 4 - 2). Moreover, the porosities measured in this study average at 5.98 % and range from 1.02 % to 17.95 %, which is in line with porosity values in serpentinized peridotites measured elsewhere (Blackman et al., 2006b; Klein et al., 2017). The control of the modal abundances of primary minerals on the MgO, SiO<sub>2</sub>, and Al<sub>2</sub>O<sub>3</sub> contents of the analyzed samples is also consistent with literature findings (Niu, 1997; Blackman et al., 2006a; Paulick et al., 2006). Thus, even though the dataset presented here is limited to 28 samples, it is generally representative of abyssal serpentinites. Importantly, however, all parameters, including FeIII/FeT and porosity, were determined on the same individual samples, which has the unique advantage of enabling testing of hypotheses related to correlations between these variables.

#### 4.4.2 *Serpentinization-related geochemical trends*

Several trends highlighted above (Section 4.3) can be justified on the basis of the geochemical behavior of peridotites affected by serpentinization reactions. The anticorrelation between serpentinization degree and FeO content results from the progressive oxidation of Fe as a peridotite becomes increasingly serpentinized (Paulick et al., 2006; Evans, 2008; Mayhew et al., 2018; Mayhew & Ellison 2020), which explains the direct proportionality between FeIII/FeT and H<sub>2</sub>O content. The MgO and SiO<sub>2</sub> contents are well explained by the modal olivine content of the rocks (Fig. 4 - 5), so that olivine-rich rocks will contain greater amounts of Mg. The positive correlation between MgO and water content likely derives from the fact that MgO-rich compositions, i.e., olivine-rich peridotites, can be subject to greater degrees of serpentinization and thus result in rocks richer in H<sub>2</sub>O. The correlation between Fe<sub>2</sub>O<sub>3</sub>T and Cr<sub>2</sub>O<sub>3</sub> contents is likely related to the varying presence of ferritchromite, whereas the correlation between FeO and Al<sub>2</sub>O<sub>3</sub> is likely the product of gabbroic melt impregnations that frequently affect ultramafic bodies in oceanic core

complexes (Blackman et al., 2006b). In fact, the latter aspect can be inferred by comparison with the terrestrial melting array (Fig. 4 - 6). In Fig. 4 - 6, data points that plot along the terrestrial array towards decreasing  $\text{MgO}/\text{SiO}_2$  and increasing  $\text{Al}_2\text{O}_3/\text{SiO}_2$  compositions are indicative of melt impregnation, which is shown by some data points that represent samples recovered during IODP Expeditions 304 and 357.

#### *4.4.3 Porosity and redox state of iron*

Our study does not demonstrate a clear correlation between porosity and Fe composition or Fe redox state in abyssal serpentinites. This observation contrasts with findings from studies on ophiolitic serpentinites (Saad, 1969; Toft et al., 1990), but is consistent with recent studies on abyssal serpentinites (Klein et al., 2017). Several studies have highlighted the presence of a well-defined trend between increasing alteration degree, magnetic susceptibility, and decreasing density of serpentinitized peridotites (Bina & Henry, 1990; Maffione et al., 2014; Oufi et al., 2002; Toft et al., 1990; Saad, 1969). The latter can be explained theoretically by involving generation of porosity, which drives the reduction in rock density, and formation of magnetite with increasing extents of serpentinitization, which drives the progressive increase in magnetic susceptibility (Toft et al., 1990). However, porosity results from the complex interplay of several factors including primary crystal fabric, deformation history, volume changes related to metamorphic alterations (dissolution, precipitation and mineral replacement reactions), and factors related to the sampling techniques adopted, like vertical unloading and, in the case of drill cores, cracking during drilling (Blackman et al., 2006a).

In the case of serpentinitized peridotite, studies have shown that significant amounts of Mg can be exported during low-temperature fluid-rock interactions after the earlier, higher-temperature stage(s) of serpentinitization (de Obeso & Kelemen, 2020; de Obeso et al., 2021; Pujatti et al., 2023;

Snow & Dick, 1995). Mg removal during this (seafloor) weathering process has been chiefly due to late stage dissolution of brucite (Jöns et al., 2017; Klein et al., 2020; Sonzogni et al., 2017). The Fe redox content of serpentinites can also be subjected to substantial reworking due to weathering and/or metasomatic alteration. This is particularly the case during low-temperature (seafloor) weathering, by oxidizing fluids such as meteoric waters or seawater – Saad (1990) studied the *Red Mountain* ultramafics, after all. Together, these results suggest caution should be taken when using the Fe(III) content as a proxy for the magnetic properties of serpentinites.

The main mineralogic control on the magnetic response of serpentinites is related to the abundance of magnetite, but low-temperature oxidation can lead to transformation of magnetite to other Fe oxides, namely maghemite (Maffione et al., 2014; Oufi et al., 2002; Saad, 1969; Su et al., 2015), hematite and/or goethite (Klein et al., 2017; Mayhew & Ellison, 2020), and further Fe oxides can result from the dissolution of Fe-rich brucite and oxidation of the Fe component (Klein et al., 2020). The transformation of magnetite to maghemite is particularly significant because, whereas it involves quantitative oxidation of Fe(II) to Fe(III), its magnetic susceptibility response is on the same order as that of magnetite (Hunt et al., 1995). Therefore, trends in magnetic response of serpentinites can also be reproduced when substantial geochemical transformation other than serpentinization affects peridotites.

Overall, both porosity and Fe(III) contents of serpentinites can be affected by seafloor weathering processes, thus are not always representative of the conditions imparted by serpentinization. The latter argument is particularly relevant to oceanic serpentinites and is exemplified by the significantly different Fe redox states measured in dredged samples versus drilled samples (Evans, 2008; Mayhew & Ellison, 2020). The abyssal serpentinites presented here have experienced varying degrees of seafloor weathering, as indicated by their plotting significantly below the

terrestrial melting array (Fig. 4 - 6), suggesting loss of MgO and potential enrichment in SiO<sub>2</sub> due to replacement of serpentine by talc. Geochemical variations are also likely to affect the properties of ophiolitic serpentinites, because prograde metamorphism can lead to reduction of Fe to Fe(II) (Debret et al., 2015; Mayhew & Ellison, 2020), and the intense deformation history linked with subduction and emplacement of ophiolitic bodies is likely to overprint the porosity generated in seafloor serpentinization settings by obliterating former pore networks and generating dehydration- and strain-related anisotropic porosity (Arkwright et al., 2008; Ganzhorn et al., 2019; Kawano et al., 2011; Plümper et al., 2017).

Another possible reason for the lack of discernible correlations between Fe redox state and porosity in serpentinites could be related to the limited range of alteration shown by the samples investigated here. In fact, the minimum water content reported here is 8.9 wt%, which roughly corresponds to a serpentinization degree of 60%, and the maximum water content is 14.6 wt% that corresponds to a serpentinization degree greater than 99%. Hence, our datasets cover peridotite that experienced roughly 60% to 100% serpentinization, lacking coverage of smaller degrees of alteration. This sampling trend is apparently consistent across studies – the extensive Mayhew et al. (2020) compilation contains far more samples that are >60% serpentinized than samples that are <60% serpentinized.

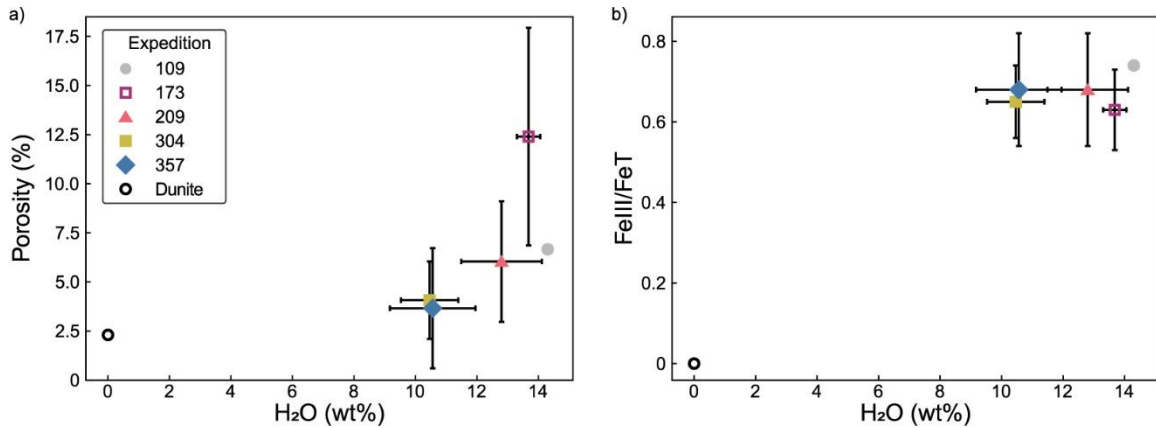


Fig. 4 - 7. Porosity and Fe redox distribution against serpentinization degree monitored via water content. The black bars are standard deviations. Data for unaltered dunite (porosity = 2.3%; FeIII/FeT = 0) after Luhmann et al. (2017). a) Mean porosity content plotted against water content grouped by drilling expedition. b) Mean FeIII/FeT plotted against water content grouped by expedition.

When grouped by expedition, the average porosity of the analyzed serpentinites from an individual expedition shows a more significant correlation with the averaged measured H<sub>2</sub>O wt% (Fig. 4 - 7a) than the analysis of the whole porosity and H<sub>2</sub>O wt% dataset (Fig. 4 - 2). Yet, expedition-averaged FeIII/FeT is apparently uncorrelated with expedition-averaged H<sub>2</sub>O wt% (Fig. 4 - 7b). Thus, while the distribution of the data is consistent with the concept of increases in porosity and Fe(III) contents with increasing degrees of serpentinization, the mean porosity appears to follow an exponential trend where the majority of the pore volume is generated at high degrees of serpentinization (Fig. 4 - 7a). On the other hand, the FeIII/FeT content plateaus at ~0.67, even when porosity is only slightly elevated above pristine peridotite porosity. This latter observation would be consistent with a control on Fe redox state that is apparently independent of the specific alteration mineralogy. In other words, magnetite alone cannot account for all Fe(III) in the samples, because magnetite, with FeIII/FeT = 0.67, does not contain H<sub>2</sub>O, the average FeIII/FeT = ~0.67 must therefore be achieved by the relative, and dynamic, partitioning of Fe(II) and Fe(III) between not only magnetite, but also brucite and serpentine as serpentinization proceeds through these advanced alteration stages.

Ultimately, it is possible that a dataset spanning the full range of alteration degrees experienced by serpentinized peridotites could reveal direct correlations between porosity content and Fe redox state that are not visible in our analyses. However, the observation that such a large portion of analyzed samples are highly serpentinized (Mayhew et al., 2020) suggests that unique field or experimental sampling efforts would be required to observe such trends.

#### 4.5 Conclusions

In this study, we present geochemical and porosity measurements of abyssal serpentinites recovered via oceanic drilling. The overall geochemical makeup of the samples presented here reproduces results from previous studies and appears representative of the geochemical concentrations measured from abyssal serpentinites. Following the hypothesis that increasing degrees of serpentinization are associated with the generation of pores and oxidation of Fe in secondary minerals, as suggested by correlations between magnetic properties and density of serpentinites predicted by early literature studies, we have investigated the presence of potential trends between the Fe redox budget and porosity measurements in abyssal serpentinites. A statistical analysis revealed no significant correlations. Porosity plots as an isolated vector in principal components spaces, with no evident positive or negative correlations with other analyzed properties. We suggest that both porosity and the Fe redox budget are strongly affected by the geologic history of serpentinized peridotites, i.e., these properties can vary significantly both during serpentinization and after serpentinization reactions cease to be active. Low-temperature seafloor weathering processes can strongly impact porosity due to the late-stage dissolution of brucite, and Fe can undergo oxidation reactions, e.g., replacement of magnetite by maghemite, which, importantly, can happen without substantial variations in magnetic susceptibility of the bulk rock. Moreover, ophiolitic serpentinites experience extensively variable conditions over

geologic timescales that can considerably affect the Fe and porosity content of serpentinites, for example via reduction of Fe to its divalent form and restructuring of the pore-network due to dehydration reactions and deformation processes. An assessment of our datasets including properties of unaltered peridotite showed the potential presence of discernible trends, thus we suggest that future work should aim at producing chemical and porosity datasets that cover serpentinization degrees from 0% to 60%.

**Acknowledgments.** This study used samples and data provided by the International Ocean Discovery Program (IODP). We acknowledge the support of the Natural Sciences and Engineering Research Council of Canada (NSERC) for providing funding for this research under Discovery Grant RGPIN-2018-03800. We would like to thank Fabio Ciceri, Lincoln Hanton, Alan Hildebrand, Amin Ghanizadeh and Adnan Younis for the insightful scientific discussions and help with collecting high-quality volumetric and porosity measurements. We want to extend our gratitude to Adedapo Awolayo for his aid in writing the codes used for data processing.

## 5 Conclusions

This thesis explored the role and significance of porosity during the alteration of mafic and ultramafic lithologies in the oceanic lithosphere. Porosity generation and evolution during fluid-rock interactions involving both hot hydrothermal fluids and low-temperature seawater have been investigated via petrographic, geochemical, and statistical methods. Mineral replacement and alteration processes are intimately linked with porosity generation, which enables the infiltration of fluids to reactive mineral surfaces and produces characteristic textural expressions that preserve evidence of the kinetically controlled geochemical processes that generated them. The samples studied in this thesis were selected from drill cores recovered from the oceanic seafloor, because they offer the advantage of being geologically young and have not undergone the physical and chemical reworking experienced by oceanic lithosphere exposed on land in ophiolitic bodies.

In Chapter 2, rock cores recovered from the seafloor of the TAG mound were analyzed petrographically, revealing the presence of a characteristic nodular texture involving anhydrite, pyrite, quartz, and pores that evolves with increasing depth within the TAG mound. Interpretation of the mineral replacement process that underlie the formation of the nodular texture enables us to constrain the internal growth dynamics of the TAG mound. The model proposed to explain the formation of the nodular texture involves circulation of hydrothermal fluids along the grain boundaries of pyrite, leading to dissolution of anhydrite. The resulting dissolved sulfur subsequently contributes to the growth of pyrite. Furthermore, the voids created at the grain boundaries of pyrite are filled by quartz that grows in open space, forming a characteristic alignment of coarse euhedral crystals. Importantly, the model is consistent with the distribution of

the isotopic signatures of sulfur in sulfides at TAG according to the predictions of the anhydrite buffer model.

In Chapter 3, tomographic techniques were employed to visualize the presence and distribution of pores from the nanoscale to the microscale in serpentinized peridotites recovered from several sites in proximity of the Mid-Atlantic Ridge. Only the highest resolution dataset displays the presence of nanometer-sized pores homogeneously distributed in the serpentine matrix, and we suggest that this class of pore sizes formed due to serpentinization. All samples revealed the presence of dissolution pores located at the grain boundaries of olivine, which, on the basis of kinetic and textural reasoning, was interpreted to result from low-temperature seafloor weathering processes. While the newly generated pores occupied a small fraction of the rocks' volumes, we estimate significant exports of Mg to seawater with consequent increase of its alkalinity as a result of this process, due to the widespread presence of ultramafic rocks at slow-spreading ridges and the pervasive nature of seafloor weathering. These chemical fluxes thereby affect the chemical composition and alkalinity of seawater, potentially affecting the solubility of carbonate minerals and consequently the coupled carbonate-silicate cycle, and thus may contribute to the maintenance of clement conditions on Earth over geologic time scales.

Chapter 4 presents a statistical analysis of geochemical and porosity data collected from serpentinized peridotites recovered from 10 different sites that drilled through basement rocks beneath the Atlantic Ocean seafloor. Based on observed increases in porosity and magnetic susceptibility signal with increasing degrees of serpentinization, we hypothesized that the porosity and bulk  $\text{Fe}^{3+}$  should increase proportionally as serpentinization reactions proceed. Importantly, however, no direct correlations were found. Rather, our results suggest that alteration due to seafloor weathering processes affects both the porosity content and geochemical composition of

the serpentinites, introducing variability that can obscure underlying trends. Clustering of the data according to expedition and including the porosity and FeIII/FeT ratio of unaltered peridotite show more clearly defined trends, however the lack of samples of weakly serpentinized peridotite prevents definitive interpretations.

The varied nature of the systems studied in the research chapters of this thesis remarks the fact that pores are a ubiquitous property of rocks and exert fundamental controls on all geological processes that involve fluid-rock interactions.

## Bibliography

- [dataset] Pujatti, S. (2023). Geochemical and porosity datasets: Fe oxidation and porosity generation in abyssal serpentinites. Open Science Framework. doi:10.17605/OSF.IO/8C7EF
- Alt, J. C. (1994). A sulfur isotopic profile through the Troodos ophiolite, Cyprus: primary composition and the effects of seawater hydrothermal alteration. *Geochimica et Cosmochimica Acta*, 58(7), 1825-1840. doi:10.1016/0016-7037(94)90539-8
- Andréani, M., Baronnet, A., Boullier, A. M., & Gratier, J. P. (2004). A microstructural study of a “crack-seal” type serpentine vein using SEM and TEM techniques. *European Journal of Mineralogy*, 16(4), 585–595. doi:10.1127/0935-1221/2004/0016-0585
- Andréani, M., Mével, C., Boullier, A. M., & Escartin, J. (2007). Dynamic control on serpentine crystallization in veins: Constraints on hydration processes in oceanic peridotites. *Geochemistry, Geophysics, Geosystems*, 8(2). doi:10.1029/2006gc001373
- Aoyama, S., Nishizawa, M., Takai, K., & Ueno, Y. (2014). Microbial sulfate reduction within the Iheya North seafloor hydrothermal system constrained by quadruple sulfur isotopes. *Earth and Planetary Science Letters*, 398, 113–126. doi:10.1016/j.epsl.2014.04.039
- Arizaleta, M. L., Nightingale, M., & Tutolo, B. M. (2020). A rate law for sepiolite growth at ambient temperatures and its implications for early lacustrine diagenesis. *Geochimica et Cosmochimica Acta*, 288, 301–315. doi:10.1016/j.gca.2020.08.014
- Arkwright, J. C., Rutter, E. H., Brodie, K. H., & Llana-Fúnez, S. (2008). Role of porosity and dehydration reaction on the deformation of hot-pressed serpentinite aggregates. *Journal of the Geological Society*, 165(3), 639–649. doi:10.1144/0016-76492007-119
- Ashworth, J. R., Birdi, J. J., & Emmett, T. F. (1992). Diffusion in coronas around clinopyroxene: modelling with local equilibrium and steady state, and a non-steady-state

modification to account for zoned actinolite-hornblende. *Contributions to Mineralogy and Petrology*, 109(3), 307–325. <https://doi.org/10.1007/bf00283321>

Awad, A., Koster van Groos, A. F., & Guggenheim, S. (2000). Forsteritic olivine: effect of crystallographic direction on dissolution kinetics. *Geochimica et Cosmochimica Acta*, 64(10), 1765–1772. doi:10.1016/s0016-7037(99)00442-1

Bach, W., & Fruh-Green, G. L. (2010). Alteration of the Oceanic Lithosphere and Implications for Seafloor Processes. *Elements*, 6(3), 173–178. doi:10.2113/gselements.6.3.173

Bach, W., Garrido, C. J., Paulick, H., Harvey, J., & Rosner, M. (2004). Seawater-peridotite interactions: First insights from ODP Leg 209, MAR 15°N. *Geochemistry, Geophysics, Geosystems*, 5(9). doi:10.1029/2004gc000744

Bach, W., Jöns, N., & Klein, F. (2013). Metasomatism within the ocean crust. In *Metasomatism and the chemical transformation of rock*, 253–288. doi:10.1007/978-3-642-28394-9\_8

Bach, W., Rosner, M., Jöns, N., Rausch, S., Robinson, L. F., Paulick, H., & Erzinger, J. (2011). Carbonate veins trace seawater circulation during exhumation and uplift of mantle rock: Results from ODP Leg 209. *Earth and Planetary Science Letters*, 311(3-4), 242–252. doi:10.1016/j.epsl.2011.09.021

Bales, R. C., & Morgan, J. J. (1985). Dissolution kinetics of chrysotile at pH 7 to 10. *Geochimica et Cosmochimica Acta*, 49(11), 2281-2288. doi: 10.1016/0016-7037(85)90228-5

Barrer, R. M. (1951). *Diffusion in and through solids*. University Press, Cambridge.

Barreyre, T., Escartín, J., Garcia, R., Cannat, M., Mittelstaedt, E., & Prados, R. (2012). Structure, temporal evolution, and heat flux estimates from the Lucky Strike deep-sea

hydrothermal field derived from seafloor image mosaics. *Geochemistry, Geophysics, Geosystems*, 13(4). doi:10.1029/2011GC003990

Beinlich, A., Austrheim, H., Mavromatis, V., Grguric, B., Putnis, C. V., & Putnis, A. (2018). Peridotite weathering is the missing ingredient of Earth's continental crust composition. *Nature Communications*, 9(1). doi:10.1038/s41467-018-03039-9

Berner, E. K., & Berner, R. A. (1987). *Global water cycle: geochemistry and environment*. Prentice-Hall, Inc., Englewood Cliffs New Jersey. 1987. 397. doi:10.1017/s0376892900009206

Berninger, U.-N., Jordan, G., Schott, J., & Oelkers, E. H. (2014). The experimental determination of hydromagnesite precipitation rates at 22.5–75°C. *Mineralogical Magazine*, 78(6), 1405–1416. doi:10.1180/minmag.2014.078.6.07

Bethke, C. M.; Farrell, B.; Yeakel, S. *The Geochemist's Workbench® Release 12.0 - Reaction Modeling Guide*; 2018.

Bina, M. M., & Henry, B. (1990). Magnetic properties, opaque mineralogy and magnetic anisotropies of serpentinized peridotites from ODP Hole 670A near the Mid-Atlantic Ridge. *Physics of the Earth and Planetary Interiors*, 65(1–2), 88–103. doi:10.1016/0031-9201(90)90078-c

Bischoff, J. L., & Seyfried, W. E. (1978). Hydrothermal chemistry of seawater from 25 degrees to 350 degrees C. *American Journal of Science*, 278(6), 838–860. doi:10.2475/ajs.278.6.838

Blackman, D. K., Ildefonse, B., John, B. E., Ohara, Y., Miller, D. J., & Macleod, C. J. (2006a). Site U1309. *Proceedings of the Integrated Ocean Drilling Program*. doi:10.2204/iodp.proc.304305.103.2006

Blackman, D. K., Ildefonse, B., John, B. E., Ohara, Y., Miller, D. J., & Macleod, C. J. (2006b). Expedition 304/305 Scientists (2006). Expedition 304/305 summary. In Proceedings of the Integrated Ocean Drilling Program, 304, 305. doi:10.2204/iodp.proc.304305.101.2006

Blount, C. W., & Dickson, F. W. (1969). The solubility of anhydrite (CaSO<sub>4</sub>) in NaCl-H<sub>2</sub>O from 100 to 450 C and 1 to 1000 bars. *Geochimica et Cosmochimica Acta*, 33(2), 227-245. doi:10.1016/0016-7037(69)90140-9

Bodnar, R. J. (1993). Revised equation and table for determining the freezing point depression of H<sub>2</sub>O-NaCl solutions. *Geochimica et Cosmochimica Acta*, 57(3), 683-684. doi:10.1016/0016-7037(93)90378-A

Boudier, F., Baronnet, A., & Mainprice, D. (2010). Serpentine Mineral Replacements of Natural Olivine and their Seismic Implications: Oceanic Lizardite versus Subduction-Related Antigorite. *Journal of Petrology*, 51(1-2), 495–512. doi:10.1093/petrology/egp049

Bowen, N. L., & Tuttle, O. F. (1949). The system MgO—SiO<sub>2</sub>—H<sub>2</sub>O. *GSA Bulletin*, 60(3), 439–460. doi: [https://doi.org/10.1130/0016-7606\(1949\)60\[439:TSM\]2.0.CO;2](https://doi.org/10.1130/0016-7606(1949)60[439:TSM]2.0.CO;2)

Brady, P. V., & Gíslason, S. R. (1997). Seafloor weathering controls on atmospheric CO<sub>2</sub> and global climate. *Geochimica et Cosmochimica Acta*, 61(5), 965-973. doi:10.1016/s0016-7037(96)00385-7

Bruland, K. W. (1983). Trace elements in seawater. *Chemical Oceanography*, 8, 157–220.

Campbell, A.C., Palmer, M.R., Klinkhammer, G.P., Bowers, T.S., Edmond, J.M., Lawrence, J.R., Casey, J.F., Thompson, G., Humphris, S., Rona, P. and Karson, J.A. (1988). Chemistry of hot springs on the Mid-Atlantic Ridge. *Nature*, 335(6190), 514-519. doi:10.1038/335514a0

Canales, J. P., Sohn, R. A., & deMartin, B. J. (2007). Crustal structure of the TAG segment (Mid-Atlantic Ridge, 26 10' N): Implications for the nature of hydrothermal circulation and detachment faulting at slow spreading ridges. *Geochemistry, Geophysics, Geosystems*, 8, Q08004. doi:10.1029/2007GC001629

Cannat, M., Fontaine, F., & Escartín, J. (2010). Serpentinization and associated hydrogen and methane fluxes at slow spreading ridges. *Diversity of Hydrothermal Systems on Slow Spreading Ocean Ridges*, 241–264. doi:10.1029/2008gm000760

Cannat, M., Karson, J.A., Miller, D.J., et al. (1995). *Proceedings of the Ocean Drilling Program, Initial Reports, 153: College Station, TX (Ocean Drilling Program)*. doi:10.2973/odp.proc.ir.153.1995

Charlou, J. L., Donval, J. P., Fouquet, Y., Jean-Baptiste, P., & Holm, N. (2002). Geochemistry of high H<sub>2</sub> and CH<sub>4</sub> vent fluids issuing from ultramafic rocks at the Rainbow hydrothermal field (36 14' N, MAR). *Chemical Geology*, 191(4), 345-359. doi:10.1016/s0009-2541(02)00134-1

Charlou, J. L., Donval, J. P., Jean-Baptiste, P., Dapoigny, A., & Rona, P. A. (1996). Gases and helium isotopes in high temperature solutions sampled before and after ODP Leg 158 drilling at TAG hydrothermal field (26 N, MAR). *Geophysical Research Letters*, 23(23), 3491-3494. doi:10.1029/96gl02141

Che, Z., Nightingale, M., & Tutolo, B. M. (2021). Probing the application of kinetic theory to Mg-phyllsilicate growth with Si isotope doping. *Geochimica et Cosmochimica Acta*, 310, 205–220. doi:10.1016/j.gca.2021.05.025

Chiba, H., Uchiyama, N., & Teagle, D. A. (1998). Stable isotope study of anhydrite and sulfide minerals at the TAG hydrothermal mound, Mid-Atlantic Ridge, 26°N. *Proceedings of*

the Ocean Drilling Program: Scientific Results, 158, 85-90.  
doi:10.2973/odp.proc.sr.158.207.1998

Clarke, G. L., & Powell, R. (1991). Decompressional coronas and symplectites in granulites of the Musgrave Complex, central Australia. *Journal of Metamorphic Geology*, 9(4), 441–450. <https://doi.org/10.1111/j.1525-1314.1991.tb00538.x>

Consolmagno S.J., G. J., & Britt, D. T. (1998). The density and porosity of meteorites from the Vatican collection. *Meteoritics & Planetary Science*, 33(6), 1231–1241. doi:10.1111/j.1945-5100.1998.tb01308.x

Constantinou, G. (1972). *The geology and genesis of the sulphide ores of Cyprus*. (Doctoral dissertation, Imperial College London (University of London)).

Coogan, L. A., & Gillis, K. M. (2013). Evidence that low-temperature oceanic hydrothermal systems play an important role in the silicate-carbonate weathering cycle and long-term climate regulation. *Geochemistry, Geophysics, Geosystems*, 14(6), 1771–1786. doi:10.1002/ggge.20113

Coogan, L. A., & Gillis, K. M. (2018). Low-Temperature Alteration of the Seafloor: Impacts on Ocean Chemistry. *Annual Review of Earth and Planetary Sciences*, 46(1), 21–45. doi:10.1146/annurev-earth-082517-010027

Cooperdock, E. H. G., & Stockli, D. F. (2018). Dating exhumed peridotite with spinel (U–Th)/He chronometry. *Earth and Planetary Science Letters*, 489, 219–227. doi:10.1016/j.epsl.2018.02.041

Cross, M. M., Manning, D. A. C., Bottrell, S. H., & Worden, R. H. (2004). Thermochemical sulphate reduction (TSR): experimental determination of reaction kinetics

and implications of the observed reaction rates for petroleum reservoirs. *Organic Geochemistry*, 35(4), 393–404. doi:10.1016/j.orggeochem.2004.01.005

de Obeso, J. C., & Kelemen, P. B. (2020). Major element mobility during serpentinization, oxidation and weathering of mantle peridotite at low temperatures. *Philosophical Transactions of the Royal Society A: Mathematical, Physical and Engineering Sciences*, 378(2165), 20180433. doi:10.1098/rsta.2018.0433

de Obeso, J. C., Santiago Ramos, D. P., Higgins, J. A., & Kelemen, P. B. (2021). A Mg Isotopic Perspective on the Mobility of Magnesium During Serpentinization and Carbonation of the Oman Ophiolite. *Journal of Geophysical Research: Solid Earth*, 126(2). doi:10.1029/2020jb020237

Debret, B., Bolfan-Casanova, N., Padrón-Navarta, J. A., Martin-Hernandez, F., Andreani, M., Garrido, C. J., López Sánchez-Vizcaíno, V., Gómez-Pugnaire, M. T., Muñoz, M., & Trcera, N. (2015). Redox state of iron during high-pressure serpentinite dehydration. *Contributions to Mineralogy and Petrology*, 169(4). doi:10.1007/s00410-015-1130-y

Demartin, B. J., Sohn, R. A., Pablo Canales, J., & Humphris, S. E. (2007). Kinematics and geometry of active detachment faulting beneath the Trans-Atlantic Geotraverse (TAG) hydrothermal field on the Mid-Atlantic Ridge. *Geology*, 35(8), 711-714. doi:10.1130/G23718A.1

Detrick, R., Honnorez, J., Bryan, W.B., Juteau, T., et al. (1988). *Proceedings of the Ocean Drilling Program, Initial Reports, 106/109*: College Station, TX (Ocean Drilling Program). doi:10.2973/odp.proc.ir.106109.1988

Douville, E., Charlou, J. L., Oelkers, E. H., Bienvenu P., Jove Colon C. F., Donval J. P., Fouquet Y., Prieur D., Appriou P. (2002) The rainbow vent fluids (36°14'N, MAR): the

influence of ultramafic rocks and phase separation on trace metal content in Mid-Atlantic Ridge hydrothermal fluids. *Chemical Geology*, 184, 37–48. doi:10.1016/s0009-2541(01)00351-5

Driesner, T. (2007). The system H<sub>2</sub>O–NaCl. Part II: Correlations for molar volume, enthalpy, and isobaric heat capacity from 0 to 1000 C, 1 to 5000 bar, and 0 to 1 X<sub>NaCl</sub>. *Geochimica et Cosmochimica Acta*, 71(20), 4902-4919. doi:10.1016/j.gca.2007.05.026

Driesner, T., & Heinrich, C. A. (2007). The system H<sub>2</sub>O–NaCl. Part I: Correlation formulae for phase relations in temperature–pressure–composition space from 0 to 1000 C, 0 to 5000 bar, and 0 to 1 X<sub>NaCl</sub>. *Geochimica et Cosmochimica Acta*, 71(20), 4880-4901. doi:10.1016/j.gca.2006.01.033

Elderfield, H., & Schultz, A. (1996). Mid-Ocean Ridge Hydrothermal Fluxes and the Chemical Composition of the Ocean. *Annual Review of Earth and Planetary Sciences*, 24(1), 191–224. doi:/10.1146/annurev.earth.24.1.191

England, P. C., and Thompson, A. B. (1984). Pressure--Temperature--Time Paths of Regional Metamorphism I. Heat Transfer during the Evolution of Regions of Thickened Continental Crust. *Journal of Petrology*, 25(4), 894–928. doi:10.1093/petrology/25.4.894

Eskola, P. E. (1920). The mineral facies of rocks. *Norsk Geologisk Tidsskrift*, 6, 143–191.

Evans, B. W. (2008). Control of the Products of Serpentinization by the Fe<sup>2+</sup>+Mg-1 Exchange Potential of Olivine and Orthopyroxene. *Journal of Petrology*, 49(10), 1873–1887. doi:10.1093/petrology/egn050

Faragó, T., Gasilov, S., Emslie, I., Zuber, M., Helfen, L., Vogelgesang, M., & Baumbach, T. (2022). Tofu: a fast, versatile and user-friendly image processing toolkit for computed

tomography. *Journal of Synchrotron Radiation*, 29(3), 916–927.  
doi:10.1107/s160057752200282x

Früh-Green, G.L., Orcutt, B.N., Green, S.L., Cotterill, C., & the Expedition 357 Scientists (2017). Atlantis Massif serpentization and life. In: *Proceedings of the International Ocean Discovery Program, 357*: College Station, TX (International Ocean Discovery Program).  
doi:10.14379/iodp.proc.357.2017

Fuhr, M., Geilert, S., Schmidt, M., Liebetrau, V., Vogt, C., Ledwig, B., & Wallmann, K. (2022). Kinetics of olivine weathering in seawater: an experimental study. *Frontiers in Climate*, 39. doi:10.3389/fclim.2022.831587

Ganzhorn, A. C., Pilorgé, H., & Reynard, B. (2019). Porosity of metamorphic rocks and fluid migration within subduction interfaces. *Earth and Planetary Science Letters*, 522, 107–117. doi:10.1016/j.epsl.2019.06.030

Gemmell, J. B., & Sharpe, R. (1998). Detailed sulfur-isotope investigation of the TAG hydrothermal mound and stockwork zone, 26°N, Mid-Atlantic Ridge. *Proceedings of the Ocean Drilling Program: Scientific Results*, 158, 71-83. doi:10.2973/odp.proc.sr.158.206.1998

Goldstein, R. H., & Reynolds, T. J. (1994). Systematics of fluid inclusions in diagenetic minerals. *SEPM short course*, 31, 199. doi:10.2110/scn.94.31

Grandstaff, D. E. (1978). Changes in surface area and morphology and the mechanism of forsterite dissolution. *Geochimica et Cosmochimica Acta*, 42(12), 1899–1901.  
doi:10.1016/0016-7037(78)90245-4

Grimes, C. B., John, B. E., Cheadle, M. J., & Wooden, J. L. (2008). Protracted construction of gabbroic crust at a slow spreading ridge: Constraints from <sup>206</sup>Pb/<sup>238</sup>U zircon ages from

Atlantis Massif and IODP Hole U1309D (30°N, MAR). *Geochemistry, Geophysics, Geosystems*, 9(8). doi:10.1029/2008gc002063

Gronvold, F., & Westrum Jr, E. F. (1976). Heat capacities of iron disulfides. Thermodynamics of marcasite from 5 to 700 K, pyrite from 300 to 780 K, and the transformation of marcasite to pyrite. doi:10.1016/0021-9614(76)90135-X

Guillot, S., & Hattori, K. (2013). Serpentinites: Essential Roles in Geodynamics, Arc Volcanism, Sustainable Development, and the Origin of Life. *Elements*, 9(2), 95–98. doi:10.2113/gselements.9.2.95

Hart, S. R., & Zindler, A. (1986). In search of a bulk-Earth composition. *Chemical Geology*, 57(3–4), 247–267. doi:10.1016/0009-2541(86)90053-7

Hébert, R., Gueddari, K., LaFlèche, M. R., Beslier, M.-O., & Gardien, V. (2001). Petrology and geochemistry of exhumed peridotites and gabbros at non-volcanic margins: ODP Leg 173 West Iberia ocean-continent transition zone. Geological Society, London, Special Publications, 187(1), 161–189. doi:10.1144/gsl.sp.2001.187.01.09

Herzig, P., Petersen, S., & Hannington, M. D. (1998). Geochemistry and sulfur-isotopic composition of the TAG hydrothermal mound, Mid-Atlantic Ridge, 26 N. *Proceedings of the Ocean Drilling Program: Scientific Results*, 158, 47-70. doi:10.2973/odp.proc.sr.158.202.1998

Hollocher, K. (2004) CIPW Norm Calculation Program. Geology Department, Union College.

Holm, N. G., Oze, C., Mousis, O., Waite, J. H., & Guilbert-Lepoutre, A. (2015). Serpentinization and the Formation of H<sub>2</sub> and CH<sub>4</sub> on Celestial Bodies (Planets, Moons, Comets). *Astrobiology*, 15(7), 587–600. doi:10.1089/ast.2014.1188

Hook, J. R. (2003). An introduction to porosity. *Petrophysics-The SPWLA Journal of Formation Evaluation and Reservoir Description*, 44(03).

Huang, K.-J., Teng, F.-Z., Plank, T., Staudigel, H., Hu, Y., & Bao, Z.-Y. (2018). Magnesium isotopic composition of altered oceanic crust and the global Mg cycle. *Geochimica et Cosmochimica Acta*, 238, 357–373. doi:10.1016/j.gca.2018.07.011

Humphris, S. E., & Tivey, M. K. (2000). A synthesis of geological and geochemical investigations of the TAG hydrothermal field: Insights into fluid-flow and mixing processes in a hydrothermal system. *Ophiolites and Oceanic Crust: New Insights from Field Studies and the Ocean Drilling Program*. doi:10.1130/0-8137-2349-3.213

Humphris, S. E., Herzig, P. M., Miller, D. J., Alt, J. C., Becker, K., Brown, D., ... & Guerin, G. (1995). The internal structure of an active sea-floor massive sulphide deposit. *Nature*, 377(6551), 713-716. doi:10.1038/377713a0

Humphris, S. E., Tivey, M. K., & Tivey, M. A. (2015). The Trans-Atlantic Geotraverse hydrothermal field: A hydrothermal system on an active detachment fault. *Deep Sea Research Part II: Topical Studies in Oceanography*, 121, 8-16. doi:10.1016/j.dsr2.2015.02.015

Hunt, C. P., Moskowitz, B. M., & Banerjee, S. K. (1995). Magnetic properties of rocks and minerals. *Handbook of physical constants* (pp. 189–204). American Geophysical Union. doi:10.1029/RF003p0189

Hunter, J. D. (2007). Matplotlib: A 2D Graphics Environment. *Computing in Science & Engineering*, 9(3), 90-95. doi:10.1109/mcse.2007.55

Irrino, G.J., Miller, D.J., and Christensen, N.I., 1996. Velocity behavior of lower crustal and upper mantle rocks from a fast-spreading ridge at Hess Deep. In Mével, C., Gillis, K.M., Allan, J.F., and Meyer, P.S. (Eds.), *Proceedings of the Ocean Drilling Program, Scientific*

Results, 147: College Station, TX (Ocean Drilling Program), 417–440. doi:10.2973/odp.proc.sr.147.027.1996

Jagoutz, E., Palme, H., Baddenhausen, H., Blum, K., Cendales, M., Dreibus, G., Spettel, B., Lorenz, V. & Wanke, H. (1979). The abundances of major, minor and trace elements in the Earth's mantle as derived from primitive ultramafic nodules. In: Lunar and Planetary Science Conference, 10th, Houston, Tex., March 19–23, 1979, Proceedings. Volume 2. New York: Pergamon Press, Inc., pp. 2031–2050.

Jamtveit, B., Malthesorensen, A., & Kostenko, O. (2008). Reaction enhanced permeability during retrogressive metamorphism. *Earth and Planetary Science Letters*, 267(3–4), 620–627. doi:10.1016/j.epsl.2007.12.016

Janecky, D. R., & Seyfried Jr, W. E. (1984). Formation of massive sulfide deposits on oceanic ridge crests: Incremental reaction models for mixing between hydrothermal solutions and seawater. *Geochimica et Cosmochimica Acta*, 48(12), 2723–2738. doi:10.1016/0016-7037(84)90319-3

Jonas, L., John, T., King, H. E., Geisler, T., & Putnis, A. (2014). The role of grain boundaries and transient porosity in rocks as fluid pathways for reaction front propagation. *Earth and Planetary Science Letters*, 386, 64–74. doi:10.1016/j.epsl.2013.10.050

Jöns, N., Kahl, W.-A., & Bach, W. (2017). Reaction-induced porosity and onset of low-temperature carbonation in abyssal peridotites: Insights from 3D high-resolution microtomography. *Lithos*, 268–271, 274–284. doi:10.1016/j.lithos.2016.11.014

Kawano, S., Katayama, I., & Okazaki, K. (2011). Permeability anisotropy of serpentinite and fluid pathways in a subduction zone. *Geology*, 39(10), 939–942. doi:10.1130/g32173.1

Kelemen, P. B., & Hirth, G. (2012). Reaction-driven cracking during retrograde metamorphism: Olivine hydration and carbonation. *Earth and Planetary Science Letters*, 345–348, 81–89. doi:10.1016/j.epsl.2012.06.018

Kelemen, P. B., Matter, J., Streit, E. E., Rudge, J. F., Curry, W. B., & Blusztajn, J. (2011). Rates and Mechanisms of Mineral Carbonation in Peridotite: Natural Processes and Recipes for Enhanced, in situ CO<sub>2</sub> Capture and Storage. *Annual Review of Earth and Planetary Sciences*, 39(1), 545–576. doi:10.1146/annurev-earth-092010-152509

Kelemen, P.B., Kikawa, E., Miller, D.J., et al. (2004). *Proceedings of the Ocean Drilling Program, Initial Reports, 209*: College Station, TX. doi:10.2973/odp.proc.ir.209.2004

King, H. E., Satoh, H., Tsukamoto, K., & Putnis, A. (2014). Surface-specific measurements of olivine dissolution by phase-shift interferometry. *American Mineralogist*, 99(2-3), 377–386. doi:10.2138/am.2014.4606

Klein, F., & Le Roux, V. (2020). Quantifying the volume increase and chemical exchange during serpentinization. *Geology*, 48(6), 552–556. doi:10.1130/g47289.1

Klein, F., Bach, W., Humphris, S. E., Kahl, W.-A., Jons, N., Moskowitz, B., & Berquo, T. S. (2014). Magnetite in seafloor serpentinite--Some like it hot. *Geology*, 42(2), 135–138. doi:10.1130/g35068.1

Klein, F., Bach, W., Jöns, N., McCollom, T., Moskowitz, B., & Berquó, T. (2009). Iron partitioning and hydrogen generation during serpentinization of abyssal peridotites from 15°N on the Mid-Atlantic Ridge. *Geochimica et Cosmochimica Acta*, 73(22), 6868–6893. doi:10.1016/j.gca.2009.08.021

Klein, F., Humphris, S. E., & Bach, W. (2020). Brucite formation and dissolution in oceanic serpentinite. *Geochemical Perspectives Letters*, 16, 1-5. doi:10.7185/geochemlet.2035

Klein, F., Marschall, H. R., Bowring, S. A., Humphris, S. E., & Horning, G. (2017). Mid-ocean Ridge Serpentinite in the Puerto Rico Trench: from Seafloor Spreading to Subduction. *Journal of Petrology*, 58(9), 1729–1754. doi:/10.1093/petrology/egx071

Klyukin, Y. I., Haroldson, E. L., & Steele-MacInnis, M. (2020). A comprehensive numerical model for the thermodynamic and transport properties of H<sub>2</sub>O-NaCl fluids. *Chemical Geology*, 557, 119840. doi:10.1016/j.chemgeo.2020.119840

Klyukin, Y. I., Steele-MacInnis, M., Lecumberri-Sanchez, P., & Bodnar, R. J. (2019). Fluid inclusion phase ratios, compositions and densities from ambient temperature to homogenization, based on PVTX properties of H<sub>2</sub>O-NaCl. *Earth-Science Reviews*, 102924. doi:10.1016/j.earscirev.2019.102924

Knott, R., Fouquet, Y., Honnorez, J., Petersen, S., & Bohn, M. (1998). Petrology of hydrothermal mineralization: a vertical section through the TAG mound. *Proceedings of the Ocean Drilling Program: Scientific Results*, 158, 5-26. doi:10.2973/odp.proc.sr.158.201.1998

Kondratiuk, P., Tredak, H., Ladd, A. J. C., & Szymczak, P. (2015). Synchronization of dissolution and precipitation fronts during infiltration-driven replacement in porous rocks. *Geophysical Research Letters*, 42(7), 2244–2252. doi:10.1002/2015gl063146

Kong, X. Z., Tutolo, B. M., & Saar, M. O. (2013). DBCreate: a SUPCRT92-based program for producing EQ3/6, TOUGHREACT, and GWB thermodynamic databases at user-defined T and P. *Computers & Geosciences*, 51, 415-417. doi:10.1016/j.cageo.2012.08.004

Krissansen-Totton, J., & Catling, D. C. (2017). Constraining climate sensitivity and continental versus seafloor weathering using an inverse geological carbon cycle model. *Nature communications*, 8(1), 1-15. doi:10.1038/ncomms15423

Lacinska, A. M., Styles, M. T., Bateman, K., Hall, M., & Brown, P. D. (2017). An experimental study of the carbonation of serpentinite and partially serpentinitised peridotites. *Frontiers in Earth Science*, 5, 37. doi:10.3389/feart.2017.00037

Lafay, R., Montes-Hernandez, G., Janots, E., Chiriac, R., Findling, N., & Toche, F. (2012). Mineral replacement rate of olivine by chrysotile and brucite under high alkaline conditions. *Journal of Crystal Growth*, 347(1), 62–72. doi:10.1016/j.jcrysgro.2012.02.040

LaFlamme, C., Hollis, S. P., Jamieson, J. W., & Fiorentini, M. L. (2018). Three-Dimensional Spatially Constrained Sulfur Isotopes Highlight Processes Controlling Sulfur Cycling in the Near Surface of the Iheya North Hydrothermal System, Okinawa Trough. *Geochemistry, Geophysics, Geosystems*, 19(8), 2798–2812. doi:10.1029/2018gc007499

Lalou, C., Reyss, J. L., & Bricchet, E. (1998). Age of sub-bottom sulfide samples at the TAG active mound. *Proceedings of the Ocean Drilling Program*, 158 Scientific Results. doi:10.2973/odp.proc.sr.158.214.1998

Lalou, C., Reyss, J. L., Bricchet, E., Arnold, M., Thompson, G., Fouquet, Y., & Rona, P. A. (1993). New age data for Mid-Atlantic Ridge hydrothermal sites: TAG and Snakepit chronology revisited. *Journal of Geophysical Research*, 98(B6), 9705. doi:10.1029/92jb01898

Lein, A. Y., Ulyanova, N. V., Ulyanov, A. A., Cherkashev, G. A., & Stepanova, T. V. (2001). Mineralogy and geochemistry of sulfide ores in ocean-floor hydrothermal fields associated with serpentinite protrusions. *Russian Journal of Earth Sciences*, 3(5), 371–393. doi:10.2205/2001es000068

Lowell, R. P., Yao, Y., & Germanovich, L. N. (2003). Anhydrite precipitation and the relationship between focused and diffuse flow in seafloor hydrothermal systems. *Journal of Geophysical Research: Solid Earth*, 108(B9). doi:10.1029/2002jb002371

Luce, R. W., Bartlett, R. W., & Parks, G. A. (1972). Dissolution kinetics of magnesium silicates. *Geochimica et Cosmochimica Acta*, 36(1), 35–50. doi:10.1016/0016-7037(72)90119-6

Luhmann, A. J., Tutolo, B. M., Bagley, B. C., Mildner, D. F. R., Scheuermann, P. P., Feinberg, J. M., Ignatyev, K., & Seyfried, W. E. (2017). Chemical and physical changes during seawater flow through intact dunite cores: An experimental study at 150–200 °C. *Geochimica et Cosmochimica Acta*, 214, 86–114. <https://doi.org/10.1016/j.gca.2017.07.020>

Macdonald, A. H., & Fyfe, W. S. (1985). Rate of serpentinization in seafloor environments. *Tectonophysics*, 116(1–2), 123–135. doi:10.1016/0040-1951(85)90225-2

Maffione, M., Morris, A., Plümper, O., & van Hinsbergen, D. J. J. (2014). Magnetic properties of variably serpentinized peridotites and their implication for the evolution of oceanic core complexes. *Geochemistry, Geophysics, Geosystems*, 15(4), 923–944. doi:10.1002/2013gc004993

Marchig, V., Blum, N., & Roonwal, G. (1997). Massive sulfide chimneys from the east pacific rise at 7°24'S and 16°43'S. *Marine Georesources & Geotechnology*, 15(1), 49-66. doi:10.1080/10641199709379934\_

Marchig, V., Puchelt, H., Rosch, H., & Blum, N. (1990). Massive sulfides from ultra-fast spreading ridge, East Pacific Rise at 18-21°S: A geochemical stock report. *Marine Mining*, 9(4), 459-493.

Mayhew, L. E., & Ellison, E. T. (2020). A synthesis and meta-analysis of the Fe chemistry of serpentinites and serpentine minerals. *Philosophical Transactions of the Royal Society A: Mathematical, Physical and Engineering Sciences*, 378(2165), 20180420. doi:10.1098/rsta.2018.0420

Mayhew, L. E., Ellison, E. T., Miller, H. M., Kelemen, P. B., & Templeton, A. S. (2018). Iron transformations during low temperature alteration of variably serpentinized rocks from the Samail ophiolite, Oman. *Geochimica et Cosmochimica Acta*, 222, 704–728. doi:10.1016/j.gca.2017.11.023

McCollom, T. M. (2007). Geochemical constraints on sources of metabolic energy for chemolithoautotrophy in ultramafic-hosted deep-sea hydrothermal systems. *Astrobiology*, 7(6), 933-950. doi:10.1089/ast.2006.0119

McCollom, T. M. (2008). Observational, experimental, and theoretical constraints on carbon cycling in mid-ocean ridge hydrothermal systems. *Magma to Microbe: Modeling hydrothermal processes at ocean spreading centers*, 178, 193-213. doi:10.1029/178gm10

McCollom, T. M. (2016a). Abiotic methane formation during experimental serpentinization of olivine. *Proceedings of the National Academy of Sciences*, 113(49), 13965–13970. doi:10.1073/pnas.1611843113

McCollom, T. M., & Bach, W. (2009). Thermodynamic constraints on hydrogen generation during serpentinization of ultramafic rocks. *Geochimica et Cosmochimica Acta*, 73(3), 856–875. doi:10.1016/j.gca.2008.10.032

McCollom, T. M., Klein, F., & Ramba, M. (2022). Hydrogen generation from serpentinization of iron-rich olivine on Mars, icy moons, and other planetary bodies. *Icarus*, 372, 114754. doi:10.1016/j.icarus.2021.114754

McCollom, T. M., Klein, F., Moskowitz, B., Berquó, T. S., Bach, W., & Templeton, A. S. (2020). Hydrogen generation and iron partitioning during experimental serpentinization of an olivine–pyroxene mixture. *Geochimica et Cosmochimica Acta*, 282, 55–75. doi:10.1016/j.gca.2020.05.016

McCollom, T. M., Klein, F., Robbins, M., Moskowitz, B., Berquó, T. S., Jöns, N., Bach, W., & Templeton, A. (2016b). Temperature trends for reaction rates, hydrogen generation, and partitioning of iron during experimental serpentinization of olivine. *Geochimica et Cosmochimica Acta*, 181, 175–200. doi:10.1016/j.gca.2016.03.002

McDermott, J. M., Sylva, S. P., Ono, S., German, C. R., & Seewald, J. S. (2020). Abiotic redox reactions in hydrothermal mixing zones: Decreased energy availability for the subsurface biosphere. *Proceedings of the National Academy of Sciences*, 117(34), 20453–20461. doi:10.1073/pnas.2003108117

Mills, R. A., & Elderfield, H. (1995). Rare earth element geochemistry of hydrothermal deposits from the active TAG Mound, 26°N Mid-Atlantic Ridge. *Geochimica et Cosmochimica Acta*, 59(17), 3511–3524. doi:10.1016/0016-7037(95)00224-n

Misch, P., & Onyeagocha, A. C. (1976). Symplectite breakdown of Ca-rich almandines in upper amphibolite-facies Skagit Gneiss, North Cascades, Washington. *Contributions to Mineralogy and Petrology*, 54(3), 189–224. <https://doi.org/10.1007/bf00371006>

Moody, J. B. (1976). Serpentinization: a review. *Lithos*, 9(2), 125–138. doi:10.1016/0024-4937(76)90030-x

Mulders, J. J. P. A., & Oelkers, E. H. (2021). An experimental study of sepiolite dissolution and growth rates as function of the aqueous solution saturation state at 60 °C. *Geochimica et Cosmochimica Acta*, 315, 276–294. doi:10.1016/j.gca.2021.09.004

Müntener, O. (2010). Serpentine and serpentinization: A link between planet formation and life. *Geology*, 38(10), 959–960. doi:10.1130/focus102010.1

Niu, Y. (1997). Mantle Melting and Melt Extraction Processes beneath Ocean Ridges: Evidence from Abyssal Peridotites. *Journal of Petrology*, 38(8), 1047–1074. doi:10.1093/etroj/38.8.1047

Oelkers, E. H., Declercq, J., Saldi, G. D., Gislason, S. R., & Schott, J. (2018). Olivine dissolution rates: A critical review. *Chemical Geology*, 500, 1–19. doi:10.1016/j.chemgeo.2018.10.008

Ohmoto, H., & Lasaga, A. C. (1982). Kinetics of reactions between aqueous sulfates and sulfides in hydrothermal systems. *Geochimica et Cosmochimica Acta*, 46(10), 1727-1745. doi:10.1016/0016-7037(82)90113-2

Ohmoto, H., Mizukami, M., Drummond, S. E., Eldridge, C. S., Pisutha-Armond, V., & Lenagh, T. C. (1983). Chemical Processes of Kuroko Formation. *The Kuroko and Related Volcanogenic Massive Sulfide Deposits*. doi:10.5382/mono.05.32

Okland, I., Huang, S., Dahle, H., Thorseth, I. H., & Pedersen, R. B. (2012). Low temperature alteration of serpentinized ultramafic rock and implications for microbial life. *Chemical Geology*, 318–319, 75–87. doi:10.1016/j.chemgeo.2012.05.015

Ono, S., Shanks, W. C., Rouxel, O. J., & Rumble, D. (2007). S-33 constraints on the seawater sulfate contribution in modern seafloor hydrothermal vent sulfides. *Geochimica et Cosmochimica Acta*, 71(5), 1170–1182. doi:10.1016/j.gca.2006.11.017

Osselin, F., Pichavant, M., Champallier, R., Ulrich, M., & Raimbourg, H. (2022). Reactive transport experiments of coupled carbonation and serpentinization in a natural serpentinite. Implication for hydrogen production and carbon geological storage. *Geochimica et Cosmochimica Acta*, 318, 165–189. doi:10.1016/j.gca.2021.11.039

Oufi, O., Cannat M., and Horen H. (2002). Magnetic properties of variably serpentinized abyssal peridotites. *Journal of Geophysical Research*, 107(B5), 2095. doi:10.1029/2001jb000549

Paganin, D., Mayo, S. C., Gureyev, T. E., Miller, P. R., & Wilkins, S. W. (2002). Simultaneous phase and amplitude extraction from a single defocused image of a homogeneous object. *Journal of Microscopy*, 206(1), 33–40. doi:10.1046/j.1365-2818.2002.01010.x

Paulick, H., Bach, W., Godard, M., De Hoog, J. C. M., Suhr, G., & Harvey, J. (2006). Geochemistry of abyssal peridotites (Mid-Atlantic Ridge, 15°20'N, ODP Leg 209): Implications for fluid/rock interaction in slow spreading environments. *Chemical Geology*, 234(3–4), 179–210. doi:10.1016/j.chemgeo.2006.04.011

Peach, C. J., Spiers, C. J., & Trimby, P. W. (2001). Effect of confining pressure on dilatation, recrystallization, and flow of rock salt at 150°C. *Journal of Geophysical Research: Solid Earth*, 106(B7), 13315–13328. doi:10.1029/2000jb900300

Peters, M., Strauss, H., Farquhar, J., Ockert, C., Eickmann, B., & Jost, C. L. (2010). Sulfur cycling at the Mid-Atlantic Ridge: A multiple sulfur isotope approach. *Chemical Geology*, 269(3-4), 180–196. doi:10.1016/j.chemgeo.2009.09.016

Petersen, S., Herzig, P., & Hannington, M. D. (1998). Fluid inclusion studies as a guide to the temperature regime within the TAG hydrothermal mound, 26 N, Mid-Atlantic Ridge. *Proceedings of the Ocean Drilling Program: Scientific Results*, 158, 163-178. doi:10.2973/odp.proc.sr.158.210.1998

Peuble, S., Andréani, M., Godard, M., Gouze, P., Barou, F., Van de Moortele, B., ... Reynard, B. (2015). Carbonate mineralization in percolated olivine aggregates: Linking effects

of crystallographic orientation and fluid flow. *American Mineralogist*, 100(2-3), 474–482.  
doi:10.2138/am-2015-4913

Plümper, O., John, T., Podladchikov, Y. Y., Vrijmoed, J. C., & Scambelluri, M. (2016). Fluid escape from subduction zones controlled by channel-forming reactive porosity. *Nature Geoscience*, 10(2), 150–156. <https://doi.org/10.1038/ngeo2865>

Plümper, O., Røyne, A., Magrasó, A., & Jamtveit, B. (2012). The interface-scale mechanism of reaction-induced fracturing during serpentinization. *Geology*, 40(12), 1103–1106. doi:10.1130/g33390.1

Pontbriand, C. W., & Sohn, R. A. (2014). Microearthquake evidence for reaction-driven cracking within the Trans-Atlantic Geotraverse active hydrothermal deposit. *Journal of Geophysical Research: Solid Earth*, 119(2), 822-839. doi:10.1002/2013JB010110

Power, I. M., Kenward, P. A., Dipple, G. M., & Raudsepp, M. (2017). Room Temperature Magnesite Precipitation. *Crystal Growth & Design*, 17(11), 5652–5659. doi:10.1021/acs.cgd.7b00311

Preiner, M., Xavier, J., Sousa, F., Zimorski, V., Neubeck, A., Lang, S., Greenwell, H., Kleinermanns, K., Tüysüz, H., McCollom, T., Holm, N., & Martin, W. (2018). Serpentinization: Connecting Geochemistry, Ancient Metabolism and Industrial Hydrogenation. *Life*, 8(4), 41. doi:10.3390/life8040041

Pujatti, S., Plümper, O., & Tutolo, B. M. (2023). Weathering-driven porosity generation in altered oceanic peridotites. *Earth and Planetary Science Letters*, 604, 118006. <https://doi.org/10.1016/j.epsl.2023.118006>

Putnis, A. (2009). Mineral Replacement Reactions. *Reviews in Mineralogy and Geochemistry*, 70(1), 87–124. doi:10.2138/rmg.2009.70.3

Putnis, A., & John, T. (2010). Replacement processes in the Earth's crust. *Elements*, 6(3), 159-164. doi:10.2113/gselements.6.3.159

Putnis, A., & Mauthe, G. (2001). The effect of pore size on cementation in porous rocks. *Geofluids*, 1(1), 37–41. doi:10.1046/j.1468-8123.2001.11001.x

Putnis, A., and Austrheim, H. (2010). Fluid-induced processes: metasomatism and metamorphism. *Geofluids*. doi:10.1111/j.1468-8123.2010.00285.x

Putnis, A., Spencer, C. J., & Raimondo, T. (2019). Timescales of geological processes: Preface. *Geoscience Frontiers*, 10(1), 1–3. doi:10.1016/j.gsf.2018.10.002

Rees, C. E., Jenkins, W. J., & Monster, J. (1978). The sulphur isotopic composition of ocean water sulphate. *Geochimica et Cosmochimica Acta*, 42(4), 377–381. doi:10.1016/0016-7037(78)90268-5

Rona, P. A., McGregor, B. A., Betzer, P. R., Bolger, G. W., & Krause, D. C. (1975). Anomalous water temperatures over Mid-Atlantic Ridge crest at 26 North latitude. *Deep Sea Research and Oceanographic Abstracts*, 22(9), 611-618. Elsevier. doi:10.1016/0011-7471(75)90048-0

Rouxel, O., Fouquet, Y., & Ludden, J. N. (2004). Copper Isotope Systematics of the Lucky Strike, Rainbow, and Logatchev Sea-Floor Hydrothermal Fields on the Mid-Atlantic Ridge. *Economic Geology*, 99(3), 585–600. doi:10.2113/gsecongeo.99.3.585

Rubie, D. C. (1986). The catalysis of mineral reactions by water and restrictions on the presence of aqueous fluid during metamorphism. *Mineralogical Magazine*, 50(357), 399–415. doi:10.1180/minmag.1986.050.357.05

Russell, M. J. (2007). The Alkaline Solution to the Emergence of Life: Energy, Entropy and Early Evolution. *Acta Biotheoretica*, 55(2), 133–179. doi:10.1007/s10441-007-9018-5

Russell, M. J., Hall, A. J., & Martin, W. (2010). Serpentinization as a source of energy at the origin of life. *Geobiology*, 8(5), 355–371. doi:10.1111/j.1472-4669.2010.00249.x

Saad, A. H. (1969). Magnetic properties of ultramafic rocks from Red Mountain, California. *Geophysics*, 34(6), 974–987. doi:10.1190/1.1440067

Scheuermann, P. P., Tutolo, B. M., & Seyfried Jr, W. E. (2019). Anhydrite solubility in low-density hydrothermal fluids: Experimental measurements and thermodynamic calculations. *Chemical Geology*, 524, 184-195. doi:10.1016/j.chemgeo.2019.06.018

Schrenk, M. O., Brazelton, W. J., & Lang, S. Q. (2013). 18. Serpentinization, Carbon, and Deep Life. *Carbon in Earth*, 575–606. doi:10.1515/9781501508318-020

Schulte, M., Blake, D., Hoehler, T., & McCollom, T. (2006). Serpentinization and Its Implications for Life on the Early Earth and Mars. *Astrobiology*, 6(2), 364–376. doi:10.1089/ast.2006.6.364

Schwarzenbach, E. M., & Steele-MacInnis, M. (2020). Fluids in submarine mid-ocean ridge hydrothermal systems. *Elements*, 16, 389-394. doi: 10.2138/gselements.16.6.389

Scott, M. R., Scott, R. B., Rona, P. A., Butler, L. W., & Nalwalk, A. J. (1974a). Rapidly accumulating manganese deposit from the median valley of the Mid-Atlantic Ridge. *Geophysical Research Letters*, 1(8), 355-358. doi:10.1029/GL001i008p00355

Scott, R. B., Rona, P. A., McGregor, B. A., & Scott, M. R. (1974b). The TAG hydrothermal field. *Nature*, 251(5473), 301-302. doi:10.1038/251301a0

Seyfried W. E., Pester N. J., Tutolo B. M., Ding K., Jr W. E. S., Pester N. J., Tutolo B. M. and Ding K. (2015). The Lost City hydrothermal system: Constraints imposed by vent fluid chemistry and reaction path models on seafloor heat and mass transfer processes. *Geochim. Cosmochim. Acta* 163, 59–79. doi:10.1016/j.gca.2015.04.040

Shanks III, W. C., Bischoff, J. L., & Rosenbauer, R. J. (1981). Seawater sulfate reduction and sulfur isotope fractionation in basaltic systems: interaction of seawater with fayalite and magnetite at 200–350 °C. *Geochimica et Cosmochimica Acta*, 45(11), 1977-1995. doi:10.1016/0016-7037(81)90054-5

Shanks III, W. C., Boehlke, J. K., Seal, R. R. (1995). Stable isotopes in mid-ocean ridge hydrothermal systems: Interactions between fluids, minerals, and organisms. In: Humphris, S. E., Zierenberg, R.A., Mullineaux, L.S., Thomsen, R.E. (Eds.), *Seafloor Hydrothermal Systems: Physical, Chemical, Biological, and Geological Interactions*, Geophysical Monograph, 91, 194-221. doi:10.1029/gm091p0194

Shanks, W. C. (2001). 8. Stable Isotopes in Seafloor Hydrothermal Systems: Vent fluids, hydrothermal deposits, hydrothermal alteration, and microbial processes. *Stable Isotope Geochemistry*, 469–526. doi:10.1515/9781501508745-011

Simmons, S. F., Brown, K. L., Tutolo, B. M. (2016) Hydrothermal Transport of Ag, Au, Cu, Pb, Te, Zn, and Other Metals and Metalloids in New Zealand Geothermal Systems: Spatial Patterns, Fluid-Mineral Equilibria, and Implications for Epithermal Mineralization. *Economic Geology*, 111 (3), 589–618. doi:10.2113/econgeo.111.3.589

Snow, J. E., & Dick, H. J. B. (1995). Pervasive magnesium loss by marine weathering of peridotite. *Geochimica et Cosmochimica Acta*, 59(20), 4219–4235. doi:10.1016/0016-7037(95)00239-v

Sonzogni, Y., Treiman, A. H., & Schwenzer, S. P. (2017). Serpentinite with and without brucite: A reaction pathway analysis of a natural serpentinite in the Josephine ophiolite, California. *Journal of Mineralogical and Petrological Sciences*, 112(2), 59–76. doi:10.2465/jmps.160509

Su, K., Liu, Q., Jiang, Z., & Duan, Z. (2015). Mechanism of magnetic property changes of serpentinites from ODP Holes 897D and 1070A. *Science China Earth Sciences*, 58(5), 815–829. doi:10.1007/s11430-014-5019-9

Tamuz, O., Mazeh, T., & Zucker, S. (2005). Correcting systematic effects in a large set of photometric light curves. *Monthly Notices of the Royal Astronomical Society*, 356(4), 1466–1470. doi:10.1111/j.1365-2966.2004.08585.x

Taskesen, E. (2020). Pca: A Python Package for Principal Component Analysis. <https://erdogant.github.io/pca>. doi: 10.5281/zenodo.7390934

Teagle, D. A., Alt, J. C., Chiba, H., & Halliday, A. N. (1998). Dissecting an active hydrothermal deposit: the strontium and oxygen isotopic anatomy of the TAG hydrothermal mound-anhydrite. *Proceedings of the Ocean Drilling Program: Scientific Results*, 158, 129-142. doi:10.2973/odp.proc.sr.158.223.1998

Thompson, A. B. (1983). Fluid-absent metamorphism. *Journal of the Geological Society*, 140(4), 533–547. <https://doi.org/10.1144/gsjgs.140.4.0533>

Tivey, M. A., Schouten, H., & Kleinrock, M. C. (2003). A near-bottom magnetic survey of the Mid-Atlantic Ridge axis at 26° N: Implications for the tectonic evolution of the TAG segment. *Journal of Geophysical Research: Solid Earth*, 108(B5). doi:10.1029/2002JB001967

Tivey, M. K. (1998). Documenting textures and mineral abundances in minicores from the TAG active hydrothermal mound using X-ray computed tomography. *Proceedings of the Ocean Drilling Program: Scientific Results*, 158, 201-212. doi:10.2973/odp.proc.sr.158.226.1998

Tivey, M. K. (2007). Generation of seafloor hydrothermal vent fluids and associated mineral deposits. *Oceanography*, 20(1), 50-65. doi:10.5670/oceanog.2007.80

Tivey, M. K., Humphris, S. E., Thompson, G., Hannington, M. D., & Rona, P. A. (1995). Deducing patterns of fluid flow and mixing within the TAG active hydrothermal mound using mineralogical and geochemical data. *Journal of Geophysical Research: Solid Earth*, 100(B7). doi:10.1029/95JB00610

Toft, P. B., Arkani-Hamed, J., & Haggerty, S. E. (1990). The effects of serpentinization on density and magnetic susceptibility: a petrophysical model. *Physics of the Earth and Planetary Interiors*, 65(1–2), 137–157. doi:10.1016/0031-9201(90)90082-9

Tosca, N. J. (2015). Geochemical pathways to Mg-clay formation. In *Magnesian Clays: Characterization, origin and applications: AIPEA Special Publication 2*, 283-329.

Tréguer, P. J., Sutton, J. N., Brzezinski, M., Charette, M. A., Devries, T., Dutkiewicz, S., Ehlert, C., Hawkings, J., Leynaert, A., Liu, S. M., Llopis Monferrer, N., López-Acosta, M., Maldonado, M., Rahman, S., Ran, L., & Rouxel, O. (2021). Reviews and syntheses: The biogeochemical cycle of silicon in the modern ocean. *Biogeosciences*, 18(4), 1269–1289. doi:10.5194/bg-18-1269-2021

Turner, F. J. (1948). Mineralogical and structural evolution of the metamorphic rocks. *Geological Society of America*, 30, 1–332. <https://doi.org/10.1130/mem30-p1>

Tutolo, B. M., Luhmann, A. J., Tosca, N. J., & Seyfried, W. E. (2018). Serpentinization as a reactive transport process: The brucite silicification reaction. *Earth and Planetary Science Letters*, 484, 385–395. doi:10.1016/j.epsl.2017.12.029

Tutolo, B. M., Mildner, D. F. R., Gagnon, C. V. L., Saar, M. O., & Seyfried, W. E. (2016). Nanoscale constraints on porosity generation and fluid flow during serpentinization. *Geology*, 44(2), 103–106. doi:10.1130/g37349.1

Velbel, M. A. (2009). Dissolution of olivine during natural weathering. *Geochimica et Cosmochimica Acta*, 73(20), 6098–6113. doi:10.1016/j.gca.2009.07.024

Vogel, H.-J., Weller, U., & Schlüter, S. (2010). Quantification of soil structure based on Minkowski functions. *Computers & Geosciences*, 36(10), 1236–1245. doi:10.1016/j.cageo.2010.03.007

Warren, J. M. (2016). Global variations in abyssal peridotite compositions. *Lithos*, 248-251, 193–219. doi:10.1016/j.lithos.2015.12.023

Waskom, M. L. (2021). Seaborn: statistical data visualization. *Journal of Open Source Software*, 6(60), 3021. doi:/10.21105/joss.03021

Whitmarsh, R. B., & Wallace, P. J. (2001). The rift-to-drift development of the west Iberia nonvolcanic continental margin: a summary and review of the contribution of Ocean Drilling Program Leg 173. *Proceedings of the Ocean Drilling Program, 173 Scientific Results*. doi:10.2973/odp.proc.sr.173.017.2001

Wicks, F. J., & Whittaker, E. J. W. (1977). Serpentine textures and serpentization. *The Canadian Mineralogist*, 15(4), 459-488.

Wilson, A. D. (1960). The micro-determination of ferrous iron in silicate minerals by a volumetric and a colorimetric method. *The Analyst*, 85(1016), 823. doi:10.1039/an9608500823

Woodruff, L. G., & Shanks, W. C. (1988). Sulfur isotope study of chimney minerals and vent fluids from 21 N, East Pacific Rise: hydrothermal sulfur sources and disequilibrium sulfate reduction. *Journal of Geophysical Research: Solid Earth*, 93(B5), 4562-4572. doi:10.1029/JB093iB05p04562

Wysokinski, T. W., Chapman, D., Adams, G., Renier, M., Suortti, P., & Thomlinson, W. (2015). Beamlines of the biomedical imaging and therapy facility at the Canadian light source – part 3. *Nuclear Instruments and Methods in Physics Research Section A: Accelerators, Spectrometers, Detectors and Associated Equipment*, 775, 1–4. doi:10.1016/j.nima.2014.11.088

Xiong, W., & Giammar, D. (2014). Forsterite Carbonation in Zones with Transport Limited by Diffusion. *Environmental Science & Technology Letters*, 1(8), 333–338. doi:10.1021/ez500182s

Yada, K. (1967). Study of chrysotile asbestos by a high resolution electron microscope. *Acta Crystallographica*, 23(5), 704–707. doi:10.1107/s0365110x67003524

Yao, X., Xia, F., Deditius, A. P., Brugger, J., Etschmann, B. E., Pearce, M. A., & Pring, A. (2020). The mechanism and kinetics of the transformation from marcasite to pyrite: in situ and ex situ experiments and geological implications. *Contributions to Mineralogy and Petrology*, 175(3), 1-25. doi:10.1007/s00410-020-1665-4

Yardley, B. W. D. (2009). The role of water in the evolution of the continental crust. *Journal of the Geological Society*, 166(4), 585–600. doi:10.1144/0016-76492008-101

Yoder, H. S. (1955). Role of water in metamorphism. doi:10.1130/SPE62-p505

You, C. F., & Bickle, M. J. (1998). Evolution of an active sea-floor massive sulphide deposit. *Nature*, 394(6694), 668-671. doi:10.1038/29279

Yu, Y., & Tikoff, B. (2020). Magnetic Cr-Rich Spinel in Serpentinized Ultramafic Complexes. *Journal of Geophysical Research: Solid Earth*, 125(11). doi:10.1029/2020jb020443

Zhao, J., Brugger, J., Grguric, B. A., Ngothai, Y., & Pring, A. (2017). Fluid-Enhanced Coarsening of Mineral Microstructures in Hydrothermally Synthesized Bornite–Digenite Solid Solution. *ACS Earth and Space Chemistry*, 1(8), 465–474. doi:10.1021/acsearthspacechem.7b00034

## Appendices

### Appendix A Supplementary Material for Chapter 2

The EMP spectrometers were set to detect S, Fe, Cu, and Zn. Natural sulfides were used as standards: pyrite for Fe and S; chalcopyrite for Cu; and sphalerite for Zn. The ZAF (atomic number, absorption, fluorescence) correction was handled with the CITZAF package. For samples 7-N-2\_71-76 and 15-N-1, Zn was excluded from the analysis to lower the acquisition time, because previous analyses lacked a discernible Zn signal. Optical microscopy showed a mineral assemblage of pyrite, anhydrite, microcrystalline quartz and minor chalcopyrite. The raw data resulting from mapping were processed using the ImageJ software package (Schindelin et al., 2012). The areas showing Cu content were assigned to chalcopyrite and were subtracted from the Fe elemental maps to find the areas associated with pyrite. The areas associated with pyrite were in turn subtracted from the S maps to determine the areas with anhydrite. Finally, the silica contents were assigned to the background values that showed no peaks for the elements considered during mapping (Table 2 - 2).

### References

Schindelin, J., Arganda-Carreras, I., Frise, E., Kaynig, V., Longair, M., Pietzsch, T., ... & Tinevez, J. Y. (2012). Fiji: an open-source platform for biological-image analysis. *Nature Methods*, 9(7), 676-682. doi:10.1038/nmeth.2019

## Appendix B Supplementary Material for Chapter 3

### Summary of ODP/IODP results

#### *Leg 209 Sample 209-1274-A-3R1 61-71 cm*

Ocean Drilling Program (ODP) Leg 209 was carried out in 2003 and resulted in drilling 19 holes at 8 sites from 14°43' to 15°44'N along the Mid-Atlantic Ridge, on well exposed outcrops of peridotite found on both sides of the rift valley (Kelemen et al., 2004). Leg 209 aimed at investigating the processes that control the generation of oceanic lithosphere at magma-starved ridge sections. The maximum penetration achieved was 209 mbsf and recovered drill cores were chiefly composed of peridotite with subordinate gabbroic rocks and impregnations. Hydrothermal alteration of rocks recovered during Leg 209 is extensive, with serpentinization pervasively affecting ultramafic rocks and chlorite-amphibole-talc assemblages replacing gabbroic rock cores and veins. Locally, rodingization affects gabbroic veins, and late stage, low-temperature carbonation and oxidative alteration were also recognized (Bach et al., 2011).

Site 1274 is the northernmost drill location along the rift valley and is found ~31 km north of the western intersection between MAR and the 15°20' Fracture Zone. One hole was drilled at this site, achieving a penetration depth of 156 mbsf. The rocks recovered consisted mainly of peridotites together with few meter-scale gabbroic intrusions (Kelemen et al., 2007). Carbonation at Site 1274 is recognized in the uppermost ~90 m of hole penetration and is present in the form of oxidative carbonates and iron oxyhydroxides-clay alteration veins and haloes. Carbonates appear either as calcite precipitated at high temperature (90 °C-170 °C) or as low-temperature aragonite veins and red to brownish oxidation haloes surrounding the veins and protruding within the unaltered protolith (Bach et al., 2011). The disappearance of carbonates from the mineral assemblage is delimited by the presence of fault gouge at ~90 mbsf. Aragonite veins constitute more than 90%

of the carbonates recovered from Site 1274 and their precipitation temperature has been constrained via oxygen isotopic analyses to range from ocean bottom seawater temperatures (~2 °C) to ~14 °C at 85 mbsf (Bach et al., 2011). Moreover, U-Th disequilibrium ages revealed that the aragonite precipitate is young (~8.5 kyr) and has uniform ages (Bach et al., 2011). Therefore, the aragonite veins have been interpreted to form from relatively unmodified seawater in the hanging wall located above the fault zone exemplified by the fault gouge interval sampled at a depth of ~90 mbsf. A late-stage of low-temperature water-rock interactions, possibly currently ongoing, is suggested also by the presence of Fe<sup>3+</sup>-rich nontronite in serpentine muds from Site 1274, which implies alteration under oxidative conditions (Kelemen et al., 2004). Core Section 209-1274-A-3R1 is made predominantly of protogranular harzburgite with subordinate dunite bands that have both been heavily altered to serpentine minerals, however locally areas with up to 15% unaltered primary minerals can be recognized. Sample 209-1274-A-3R1 61-71 was recovered from a representative portion of the overall core section at ~17.51 mbsf and is delimited at its top and bottom by the presence of orange iron oxyhydroxide and carbonate veins (Kelemen et al., 2004).

*Leg 209 Sample 209-1272-A-21R1 55-57 cm*

Site 1272 was also drilled during ODP Leg 209 and is located on the western flank of the Mid-Atlantic rift valley, close to the top of the inside corner high, south of the 15°20' Fracture Zone. Hole 1272A achieved a penetration depth of 131.5 m, recovering a rock sequence made of diabase/microgabbros in the upper ~56 mbsf, and a lower section down to the bottom of the hole made of protogranular harzburgite (Kelemen et al., 2004). The predominant style of hydrothermal alteration recognized at Hole 1272A is serpentinization, which is close to completion across the first 100 mbsf. Low-temperature oxidative alteration is identified at Hole 1272A and, similar to

Hole 1274A, it is expressed as red-brown clays and iron oxyhydroxides associated with aragonite veins. Moreover, at Site 1272 iowaite mineralization is identified in most samples of serpentinized harzburgite. Iowaite ( $\text{Mg}_6\text{Fe}^{3+}_2(\text{OH})_{16}\text{Cl}_2 \cdot 4\text{H}_2\text{O}$ ) is thought to form due to the ingress of seawater at depth and its interaction with the brucite content in peridotite as a late stage alteration that occurs at the seafloor (Bach et al., 2004). Iowaite has a similar crystal structure to brucite and results from the replacement of brucite by oxidizing its  $\text{Fe}^{2+}$  content to  $\text{Fe}^{3+}$  and charge balancing with the addition of  $\text{Cl}^-$  between the brucite layers. Several faults have been identified at Hole 1272A and their location is signaled by the presence of fault gouge and local increased veining. At the depths sampled during Leg 209 fault gouge is expected to be saturated with groundwater and highly conductive to fluid flow compared to the surrounding wallrock (Kelemen et al., 2004). Sample 209-1272-A-21R1 55-57 analyzed in this study was recovered from a depth of ~99.5 mbsf and is made of protogranular harzburgite that is heavily altered to serpentine (99% alteration). Several fault zones have been identified in the vicinity of sample 209-1272-A-21R1 55-57. Fault gouge was recognized in Core 19R (86 mbsf) and a 25 cm thick dunite vein interpreted to have formed within a fault was found in Section 23R-1 (108 mbsf). Furthermore, two other fault zones were tentatively identified in the form of a ~1 m thick fault gouge-dominated interval in core Section 21R-2 (100.6 mbsf) and a single piece of soapstone found in Section 21R-1 at cm 68 (depth ~99.58 mbsf) that seems to correlate with a major inclined fault zone determined from formation microscanner logging images recorded at the same depth as the soapstone clast and could explain the low recovery at that interval (Kelemen et al., 2004).

*Expedition 357 Sample 357-72-B-8R2 47-49 cm*

IODP Expedition 357 drilled an east-west transect across the southern wall of the Atlantis Massif to investigate potential links between serpentinization processes and their influence on microbial

populations in the shallow subseafloor. Seventeen holes were drilled to shallow depth (max penetration of 16.44 mbsf) obtaining high recovery (up to 74.76%). Two IODP expeditions have drilled into the Atlantic Massif, producing significantly different types of rock recoveries: Expedition 357 and 304/305. During Expedition 304/305 more than 90% of recovered cores were made of gabbroic rocks. Rock cores recovered during Expedition 357 show instead more variability, ranging from sedimentary carbonate and chalk at the seafloor to ultramafic rocks and mafic intrusions of gabbroic composition that frequently “impregnate” ultramafic lithologies and are found as discrete veins (Früh-Green et al., 2016). Several styles of hydrothermal alteration were observed, with serpentinization being the most pronounced, followed by talc-tremolite-chlorite replacements that were commonly identified at the contact between ultramafic lithologies and gabbro intrusions. Moreover, rodingization and late stage carbonate veins and replacements were recognized locally. The sample investigated in this study was recovered from Hole B at Site 72, which is located close to the summit of the corrugated detachment surface that is found on the top of the Atlantis Massif, approximately 750 m north-northwest of the Lost City hydrothermal field. Hole B at Site 72 penetrated to 12.43 mbsf, drilling through a surficial cover made of carbonate sands, and basaltic breccias rubble followed below ~6.2 mbsf by a complex fault zone (Früh-Green et al., 2017). The fault zone is pervasively affected by metasomatic alterations that range in style from serpentinization, talc-amphibole-chlorite metasomatism, oxidation, and rodingization. The alteration extent and geochemical enrichment in lithium, cerium and strontium of lithologies from Hole 72 B and sites from the central area of Atlantis Massif suggest that the fault zone acted as a preferential fluid pathway for seawater recharge and flow of hydrothermal fluids (Früh-Green et al., 2017). Sample 357-72-B-8R2 47-49 was recovered from ~12 mbsf from an interval of serpentinized harzburgite that shows the presence of metasomatic talc-chlorite veins

and patches. Within the same core section as sample 357-72-B-8R2 47-49, shipboard XRD analyses identified the presence of carbonate in veins, which amounted up to ~6 wt%. Furthermore, photomicrographs collected during Expedition 357 from sample 357-72-B-8R2 76-77 show the presence of olivine neoblasts pseudomorphically replaced by carbonate minerals (Früh-Green et al, 2016).

*Expedition 304/305 Sample 304-1309B-11R 110-114 cm*

International Ocean Discovery Program (IODP) Site 1309 is situated on the central dome of the Atlantic Massif, an oceanic core complex (OCC) located ~15 km west of the median-axis valley of the MAR. The domal and corrugated seafloor at the 0.5-2 Ma old massif is interpreted to be a low angle detachment fault surface (Blackman et al., 2006b). Eight holes were drilled during IODP Expeditions 304 and 305 in the footwall of the detachment fault system, and the main rock type observed was of gabbroic composition. Rock cores from Site 1309 record a complex alteration history with multiple stages of metamorphic reworking under variable conditions that range from granulite to zeolite facies. The latest and lowest T metamorphic alteration is recorded by white veins infilled by carbonate and sulfide  $\pm$  chlorite or carbonate associated with saponite. This stage is inferred to occur at low temperature, possibly ambient condition at ~ 100-120 °C as recorded at the bottom of Hole 1309D (Blackman et al., 2006b).

The sample analyzed in this study was recovered from Hole 1309B, which was drilled to 101.8 meters below the seafloor (mbsf). Hole 1309B is composed of two intrusive series separated by a relatively narrow interval of serpentinized harzburgite (maximum thickness = 3.5 m, 1.4 m of recovered material, Blackman et al., 2006a). The peridotite interval is heavily serpentinized (alteration degree from 60% to ~100%) and cut by veins at all scales. Serpentine veins are commonly associated with fine-grained carbonate, which was also observed replacing ribbon-

textured serpentine during IODP Expedition 304/305 (Blackman et al., 2006b). Moreover, calcite and/or aragonite veins were locally recognized. Analysis of cross-cutting relationship including results from Hole 1309D revealed that the carbonate veins postdate metamorphic alteration under greenschist facies, and the veins were commonly parallel to the contacts between gabbroic and ultramafic rocks (Blackman et al., 2006a). Primary olivine crystals show a lattice preferential orientation (LPO) that records the mantle flow direction. Sample 304-1309B-11R 110-114 was recovered from ~58 mbsf and is part of an ultramafic unit made of protogranular harzburgite that records the contact with the upper gabbroic units. A mm-wide white zone of talc-tremolite-carbonate alteration is present at the contact between mafic and ultramafic rocks and intrudes into the ultramafic unit along fractures. Two subparallel, talc-bearing dikelets intrude sample 304-1309B-11R 110-114.

## **Extended Methods**

### *Training material for machine learning*

The material used to train the artificial intelligence algorithm used to segment pore structures in our tomographic data sets was prepared by selecting at least 6 and up to 15 slices from the processed data sets, grouped in sequences of 3 adjacent slides. The porous areas shown in the selected images were then carefully segmented manually inside Dragonfly. The segmented training slices were fed to the artificial intelligence algorithm, which was trained on the manually reconstructed slices for approximately 8 hours. This timespan was sufficient to train the algorithm to accurately recognize pores and discard any remaining pixel as background, and could thus be applied to the entirety of the unsegmented data sets to obtain accurate thresholding of the pore network. A similar processing and reconstruction procedure was used for the FIB-SEM data sets, although a new set of slices had to be segmented manually to produce the training material for a

new algorithm. The FIB-SEM data sets were acquired at different experimental conditions than the  $\mu$ -CT data set, resulting in images with different resolution and shading effects, which necessarily required different treatment.

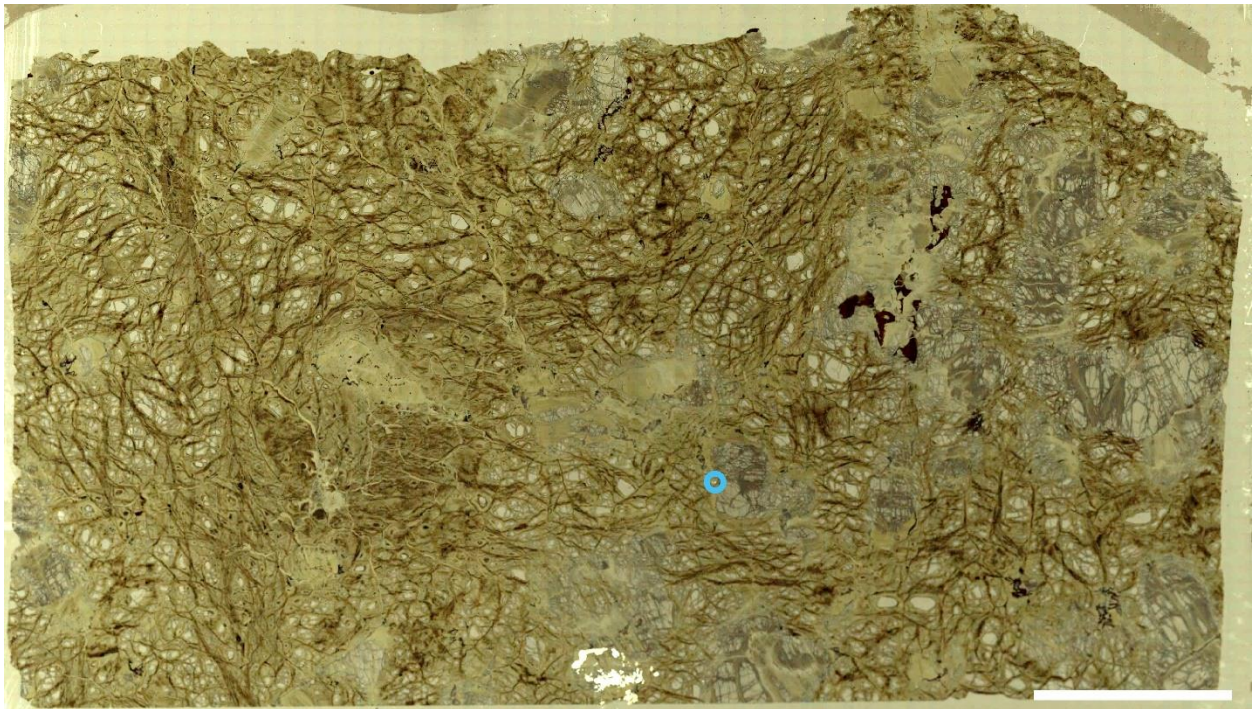
### *Euler characteristic*

The Euler characteristic  $\chi$  is a topological parameter that can be used to describe the connectivity of a structure. In 3D, it is the number of isolated objects  $N$  (i.e. pores) minus the number of redundant connections or loops  $L$  (i.e. pore throats) plus the number of cavities  $O$  (Vogel et al., 2010):

$$\chi = N - L + O \quad \text{Eq. S1}$$

In simplified terms, negative values of  $\chi$  indicate a higher number of connections, thus a higher degree of connectivity.

### **Supplementary figure**



Parallel nicols photomicrograph of sample ODP 209-1274-A-3R1 61-71. The light-blue circle shows the location where FIB-1-209 and FIB-2-209 were acquired. White scale bar = 1 cm.

## References

Bach, W., Garrido, C. J., Paulick, H., Harvey, J., & Rosner, M. (2004). Seawater-peridotite interactions: First insights from ODP Leg 209, MAR 15°N. *Geochemistry, Geophysics, Geosystems*, 5(9). doi:10.1029/2004gc000744

Bach, W., Rosner, M., Jöns, N., Rausch, S., Robinson, L. F., Paulick, H., & Erzinger, J. (2011). Carbonate veins trace seawater circulation during exhumation and uplift of mantle rock: Results from ODP Leg 209. *Earth and Planetary Science Letters*, 311(3-4), 242–252. doi:10.1016/j.epsl.2011.09.021

Blackman, D. K., Ildefonse, B., John, B. E., Ohara, Y., Miller, D. J., & Macleod, C. J. (2006a). Site U1309. *Proceedings of the Integrated Ocean Drilling Program*. doi:10.2204/iodp.proc.304305.103.2006

Blackman, D. K., Ildefonse, B., John, B. E., Ohara, Y., Miller, D. J., & Macleod, C. J. (2006b). Expedition 304/305 Scientists (2006). Expedition 304/305 summary. *Proceedings of the Integrated Ocean Drilling Program (Vol. 304, p. 305)*. doi:10.2204/iodp.proc.304305.101.2006

Früh-Green, G. L., Orcutt, B. N., Green, S. L., Cotterill, C., and the Expedition 357 Scientists (2017). Central sites. In: *Atlantis Massif Serpentinization and Life*. *Proceedings of the International Ocean Discovery Program*, 357. doi:10.14379/iodp.proc.357.104.2017

Früh-Green, G.L., Orcutt, B.N., Green, S.L., Cotterill, C., and the Expedition 357 Scientists (2016). *Atlantis Massif Serpentinization and Life*. *Proceedings of the International Ocean*

Discovery Program, 357: College Station, TX (International Ocean Discovery Program).  
doi:10.14379/iodp.proc.357.2017

Kelemen, P. B., Kikawa, E., & Miller, D. J. (2007). Leg 209 Summary: Processes in a 20-km-Thick Conductive Boundary Layer beneath the Mid-Atlantic Ridge, 14°–16°N. Proceedings of the Ocean Drilling Program, 209 Scientific Results. doi:10.2973/odp.proc.sr.209.001.2007

Kelemen, P.B., Kikawa, E., Miller, D.J., et al. (2004). Proceedings of the Ocean Drilling Program, Initial Reports., 209: College Station, TX (Ocean Drilling Program). doi:10.2973/odp.proc.ir.209.2004

Vogel, H.-J., Weller, U., & Schlüter, S. (2010). Quantification of soil structure based on Minkowski functions. Computers & Geosciences, 36(10), 1236–1245.  
doi:10.1016/j.cageo.2010.03.007

## Appendix C Supplementary Material for Chapter 4



Full correlation matrix spanning all variables measured in this study. Only the bottom half of the correlation matrix has been plotted to ease the interpretation of the data set.

## Appendix D Copyright Permissions

Benjamin M. Tutolo



**Ben** 11:46 PM

Permission granted

Matthew Steele-MacInnis

Definitely, you have my full permission and blessing. Please let me know if you need anything else.

Cheers,  
Matt

---

Matthew Steele-MacInnis  
Associate Professor

Oliver Plümper

Dear Simone.

I agree that you upload your thesis. No problem with me.

Best

Oliver

Yury Klyukin



**Yury Klyukin** 12:40 AM

Hi, sure, no problem.

I, Dr. Yury Klyukin, grant Simone Pujatti a permission to distribute any work in which we collaborated, freely and in any way future Dr. Pujatti sees appropriate